The Hashemite Kingdom of Jordan
Scientific Research Support Fund
The Hashemite University

JJEES

Jordan Journal of Earth and Environmental Sciences

Indexed by Scopus
ELSEVIER

Volume (15) Number (2)

Cover photo © Dr. Bety S. Al-Saqarat

JJEES is an International Peer-Reviewed Research Journal

ISSN 1995-6681 jjees.hu.edu.jo June 2024

Jordan Journal of Earth and Environmental Sciences (JJEES)

JJEES is an International Peer-Reviewed Research Journal, Issued by Deanship of Scientific Research, The Hashemite University, in corporation with, the Jordanian Scientific Research Support Fund, the Ministry of Higher Education and Scientific Research.

Editorial Board:

Submission address:

Manuscripts should be submitted electronically to the following e-mail:

jjees@hu.edu.jo

For more information and previous issues:

www.jjees.hu.edu.jo

Hashemite Kingdom of Jordan

Scientific Research Support Fund

Hashemite University

Jordan Journal of Earth and Environmental Sciences

JJEES

An International Peer-Reviewed Scientific Journal

Financed by the Scientific Research Support Fund

Volume 15 Number (2)

http:// jjees.hu.edu.jo/

ISSN 1995-6681

Wadi Rum is a vast, expansive area, on both sides of which are mountains of bright red sand rocks decorated with gradual bands of color that give it a touch of magic and beauty, which prompted the first Nabataeans to choose it to carve the charming city of Petra into its rocks to be their historical capital (Umm Ishrin in Wadi Rum desert).
Photograph by Dr. Bety S. Al-Saqarat, May 10, 2024

JJEES
Jordan Journal of Earth and Environmental Sciences

JJEES

JJEES (2024) 15 (2): 77-81
ISSN 1995-6681

Jordan Journal of Earth and Environmental Sciences

Investigation of Heavy Metals in Indoor Dust from Irbid, Jordan

Idrees F. Al-Momani*, Sawsan M. Ali

Chemistry Department, Yarmouk University, Irbid, Jordan

Received February 19, 2023; Accepted February 26, 2024

Abstract

The purpose of this study is to investigate the presence of a variety of heavy metals in the household dust of residents in Irbid, Jordan. Seventy samples of household dust were taken from various parts of the city, digested, and analyzed using flame atomic absorption spectroscopy (FAAS) for the presence of Pb, Cd, Cu, Zn, Co, Ni, Cr, Fe, and Mn. The geometric mean concentrations were 83.4, 2.1, 531.7, 94.8, 36.2, 16.1, 126.4, 141.3, and 9278 mg/kg for Pb, Cd, Zn, Cu, Cr, Co, Ni, Mn, and Fe, respectively. Calculations were done to determine enrichment factors about the abundance of heavy metals in the earth's crust. According to the findings, Cd and Ni are extremely enriched in the dust samples taken from indoor environments, whereas Pb, Cu, and Zn are only moderately so. The incorporation of dust from both indoor and outdoor sources into the environment of the house is thought to be the cause of the enrichment of certain elements. Calculations, based on a factor analysis, revealed that the outdoor dust from a variety of sources, which is typically brought inside by foot traffic, has a significant impact on the quality of the indoor environment.

Keywords: *Heavy metals, Indoor environment, House dust, Atomic absorption.*

1. Introduction

A growing number of researchers have recently become interested in the potential dangers posed by polluted air found inside buildings. The levels of contaminants, found in house dust, particularly heavy metals, have received a significant amount of attention in recent years (Shi and Wang, 2021; Naimabadi et al., 2021; Doyi et al., 2019). Dust in the home is a byproduct of modern living and occurs as a result of the interaction of liquids, solids, and gaseous substances that are produced by a variety of different sources. Aerosol particles, solvents, fungal spores, and soil particles, brought in on people's shoes, are the usual constituents of house dust. The precise composition is determined by multiple factors, including the activity of endogenous and exogenous sources (Gul et al., 2023; Shi and Wang, 2021).

It is possible for airborne particles and dust from nearby highways that contain heavy metals to make their way into the interior of the house through windows or balconies. It has been found that homeowners who regularly vacuum their homes, mop their floors, and dust their furniture have lower levels of metal in their homes (Gul et al., 2023; Tong and Lam, 2000). In addition, the distribution of heavy metals in house dust is affected by the activities that take place inside, the characteristics of the house, the distance that separates the building from the sources of vehicular emissions, and the type of heating that is used (Al-Momani et al., 2015). The mode of heating utilized during the colder months has a significant impact on the concentrations of various heavy metals. The highest concentrations have been found in residential properties that heat their spaces with wood or olive waste. The majority of the lead, zinc, cadmium, and copper are associated with the carbonate phases, whereas the majority of the aluminum, vanadium, manganese, and chromium are associated with the remainder (Al-Momani et al., 2015).

An increase in the levels of heavy metals can have devastating effects on human health, particularly in childhood. Children are at a greater risk than adults because they are more likely to engage in activities that involve hand-to-mouth activity (Tan et al., 2016). Because of this, it is anticipated that higher concentrations will be absorbed by the bodies of children as compared to adults. For example, a great deal of research has been done to determine how Pb intake affects children's total body burden. It was discovered that there is a correlation between the amount of lead that is present in blood and the amount of lead that is present in household dust (Isley et al., 2022).

Several studies on heavy metal levels in Jordanian soil, air, street dust, and water have been published (Tarawneh et al., 2021; Al-Massaedh and Al-Momani 2020; Mashal et al., 2017). However, indoor heavy metal levels have received less attention (Al-Momani et al., 2015; Al-Momani, 2007). The goal of this study is to estimate the levels of Pb, Cd, Cu, Zn, Co, Ni, Cr, Fe, and Mn in indoor dust, collected from 70 homes in Irbid, Jordan.

2. Materials and Methods

2.1. Sampling site

Irbid is Jordan's second-largest city. It is located on flat land, 80 kilometers north of Jordan's capital, Amman. From the north, east, and south, it is surrounded by fertile agricultural lands. In general, Summer in Irbid is exceptionally long, hot, and dry while winter is comparatively brief, cool, and wet. From November to mid-April, the weather is rainy, and the rest of the year is very dry.

* Corresponding author e-mail: imomani@yu.edu.jo

2.2. Sample collection

Samples of house dust were collected from a total of seventy different homes in Irbid City, randomly selected during the winter months. The average age of the homes was twenty years. The vacuum cleaners were utilized in the gathering of the indoor dust samples were carried in plastic bags during transport and storage prior to further preparation and examination of the samples.

2.3. Reagents and Glassware

All of the reagents had an analytical grade purity. HF had an assay of 40% (Union LAR. Supplies), and the HNO3 had a high purity assay of 69-71% (BDH Limited, England). Every solution was made with deionized water, which has an electrical conductivity of 18.2 M. After being cleaned with soap, all of the glassware and plastic bottles were then washed completely with tap water. After that, every bottle was soaked in a solution containing 10% HNO3 (v/v) for 24 hours in order to remove any heavy metal contamination. Before being used, the bottles were washed with deionized water and dried.

2.4. Sample preparation

After being dried, the samples were sieved using a polystyrene screen with a 250 µm opening size. Approximately 0.5 g sample was weighed out and placed in a 250 ml Teflon beaker. After adding approximately 15 ml of HNO3 and 4 ml of HF, the mixture was allowed to sit at room temperature for 24 hours. The digestion procedure is described in detail elsewhere (Al-Momani et al., 2015; Al-Momani 2007). Deionized water was then used to dilute the digest to a volume of 50 mL and then stored in pre-cleaned plastic bottles.

2.5. Chemical Analysis

Concentrations of Pb, Cd, Cu, Zn, Co, Ni, Cr, Fe, and Mn were determined using flame atomic absorption spectrophotometry (Varian Spectra AA, AUSTRALIA). The working standard solutions were prepared using standard stock solutions (BDH Chemicals Ltd. Poole, England). The external calibration curves were used to make quantitative determinations for each element.

2.6. Quality Assurance/Quality Control

Throughout the entirety of the experiment, quality control was kept in check through the frequent analysis of reagent blanks, standard samples, and standard reference materials. Because the concentrations shown by blank solutions were not significant, their values were disregarded. The calculated sample-to-blank concentration ratio for each of the measured elements was greater than 10% for all elements, providing further evidence that these results were accurate.

The reliability of the results of the analysis was confirmed by conducting additional tests on standard reference materials (SRM). There were a total of three SRMs that were utilized, and they were as follows: SRM-1646a, SRM-1633b, and SRM-2702. SRM samples were subjected to the same process of digestion and analysis as regular samples. Overall, the results matched the certified concentrations very closely within a range of 5–10% for all of the elements that were measured.

3. Results and Discussions

3.1. Heavy metals in household dust

A statistical overview of the measured elements is presented in Table 1. The fact that the arithmetic means for the measured elements are higher than the geometric means demonstrates that the concentrations of elements, found in the collected dust samples, are positively skewed. Therefore, to provide a more accurate depiction of the data, the Ryan-Joiner test of normality was carried out. The findings showed that the data are not normally distributed (p-values are less than 0.05). Therefore, geometric means, presented in Table 1, more accurately represent levels rather than arithmetic means.

The geometric mean concentration of Zn was approximately 531 mg/kg, making it the second most abundant metal after Fe. On the contrary, the geometric mean concentration of Cd was 62.1 mg/kg, making it the least abundant metal. The following is a ranking of the heavy metal concentrations found in the dust, collected from the homes that were investigated: Fe > Zn > Mn > Ni > Cu > Pb > Cr > Co > Cd.y

Table 1. Statistical summary of heavy metal concentrations (mg/kg dry weight) in house dust of Irbid residences.

Element	Avg.	SD	G-Mean	Min	Max
Cu	103.8	42.6	94.8	32.7	191.6
Ni	227.7	345.4	126.4	38.7	1499.8
Zn	539.7	84.7	531.7	228.6	729.8
Mn	150.0	49.8	141.3	56.7	316.4
Co	18.9	9.6	16.1	0.9	48.0
Pb	102.1	56.6	83.4	3.2	273.3
Cd	2.6	1.4	2.1	0.1	6.5
Cr	40.3	17.5	36.2	3.7	83.0
Fe	10459	3931	9278	133	20879

3.2. Comparison with literature data

In all environmental studies, one of the most important steps that must be taken into account in order to determine the level of contamination by various metals is to compare the data with the literature. Although houses from different countries differ in their designs, structural materials, ventilation, and building codes, the inside activities and the contribution of the indoor environment are still common. In addition, comparing the data with those from relevant regions would help detect the outliers that could indicate analytical errors. Therefore, the results of this study are compared with those reported by other researchers in various cities and are presented in Table 2.

Careful inspection of the data reveals that the levels of major anthropogenic elements (Cu, Pb, Cr, and Cd) are lower than those reported in Table 2. The lead levels are five times lower than those reported for Ottawa, and they are two to three times lower than those for Sydney and Amman, respectively (Rasmussen et al., 2001; Doyi et al., 2019; Al-Momani 2007). It is possible that the age of the house is to blame for the high levels of lead, found in some of the homes that were investigated. Older homes have more damaged interior surfaces and warped windows and doors, which

can trap heavy metal particulate (Kim and Fergusson, 1993; Cheng et al., 2018; Shi and Wang, 2021).

The second group of elements is comprised of Zn, Co, and Mn. These elements have levels that are approximately in the middle of the range as shown in Table 2. The geometric mean concentration of Zn was found to be 532 mg/kg, which is higher than what was reported for Sydney, but lower than what was reported for Amman and Ottawa. The proximity of the houses to the main road, which has heavy traffic, may have contributed to the presence of Zn in the dust. The increased Zn content could have been caused by wear and tear of vulcanized vehicle tires as well as corrosion of galvanized roofs (Al-Momani 2007; Cheng et al., 2018).

This study found significantly higher levels of Ni and Fe than any of those reported in Table 2. The concentration of Ni can range from 38.7 to 1499.8 mg/kg while the concentration of Fe ranges from 133.2 to 20879.2 mg/kg. Anthropogenic sources, such as emissions from vehicles and street dust, are the origins of the elements of Ni and Fe found in dust. This includes sources originating from automobile components, such as tire abrasion, brushing, bearing metals, and brake dust (Al-Momani et al., 2015; Doyi et al., 2019; Isley et al., 2022).

Table 2. Comparison of the trace metals concentrations in indoor vacuum dust with global concentration distribution of trace metals in indoor dust (mg/Kg).

	Pb	Cd	Zn	Cu	Cr	Co	Ni	Mn	Reference
Irbid, Jordan	83.4	2.1	531.8	94.8	36.2	16.1	126.4	141.3	This Study
Ottawa, Canada	406	6.46	717	206	86.7	8.92	63	267	Rasmussen et al., 2001
Amman, Jordan	169	2.92	1985	133	66.5	20.5	47	283.6	Al-Momani 2007
Istanbul, Turkey	28	0.8	832	156	55	5	263	136	Kurt-Karakus, 2012
Canada	210	6	833	279	117		102		Rasmussen et al., 2013
Japan	57.9	1.02	920	304	67.8	4.69	59.6	266	Yoshinaga et al., 2014
Al-Karak, Jordan	51.9			90.4	72.5		70	243.2	Al-Madanat et al., 2017
Chengdu, China	123	2.37	657	161	82.7		52.6		Cheng et al., 2018
Sydney, Australia	299		1876	272	90		50.9	220	Doyi et al., 2019
Neyshabur, Iran	56	1.93	513	158	67	9.7	92	332	Naimabadi et al., 2021

3.3. Enrichment of measured elements

The aluminosilicate material is the primary component of elements that can be found in sediments. It is expected that this source will explain the observed concentrations if there were no anthropogenic sources. However, because of the contributions from a variety of man-made sources, the composition of house dust is altered. In studies of atmospheric aerosols (Al-Momani et al., 2005) and soil (Isley et al., 2022; Khudhur et al., 2018; Al-Omari et al, 2012; Tong and Lam 2000; Kim and Fergusson, 1993), it is common practice to employ crustal enrichment factors (EFc) in order to ascertain the degree to which the soil composition has been altered. Iron was chosen as the element to serve as a reference because it is predominately found in the crust (Al-Momani et al., 2015; Al-Omari et al, 2012; Alghamdi et al., 2022; Madadi et al., 2022). The following formula can be used to determine the value of EFc:

$$EF_c = \frac{(C_x / C_{Fe})_{sample}}{(C_x / C_{Fe})_{crust}}$$

where $(C_x/C_{Fe})_{sample}$ is the element X concentration ratio in the sample, and $(C_x/C_{Fe})_{crust}$ is the same ratio in crustal material obtained from the compilation of trace elements in the earth's crust by Rudnick and Gao (Rudnick and Gao 2003). Enrichment factors that are greater than one indicate that crustal dust is not the only source. In general, EF values that are lower than 5.0 are not considered to be significant. Minor enrichments may result from differences in local soil composition and the reference soil used in EF calculations.

Figure 1 displays the crustal enrichment factors of the various elements that were measured. According to the findings, the concentrations of many elements are higher than their natural concentrations. The selective importation of small particles and the preferential removal of the coarser fractions during cleaning are two possible mechanisms for the occurrence of this phenomenon (Tong and Lam 2000). Both of these mechanisms have been proposed as potential explanations of the enrichment of elements in house dust.

It has been observed that the values of the EF for the same element can vary greatly from one house to the next. One possible explanation for this difference is that the strength of the various sources changes to varying degrees. The level of outdoor dust from a variety of sources, which is typically brought inside by foot traffic, has a significant impact on the quality of the environment inside buildings. There are also other dust sources in the indoor environment, such as skin, hair, mites, the rubber of carpet underlays, fibers from clothing and furniture, cooking emissions, heating emissions, and cigarette smoke (Gul et al., 2023; Morawska and Salthammer 2003). As a consequence, the large variation in the EF values could be explained by the incorporation of dust from both inside and outside the house into the environment of the home.

More than 30 enrichment factors were found for Pb, Cd, Zn, Ni, and Cu in samples taken from house dust. These results must be taken as evidence of widespread contamination. The previously used leaded gasoline, former use of lead-based paint, lead solder, and lead pipe are typically thought to be the primary contributors to the accumulation of lead in house dust (Kim and Fergusson, 1993). This is

because these activities left a legacy of contamination over a long time. However, the most significant contributor to the presence of lead in the air around the world is the combustion of leaded gasoline by motor vehicles. Recent years have seen an increase in Jordan's adoption of unleaded gasoline for widespread use. As a result, one should anticipate that the fine particles emitted from motor vehicles that contain lead compounds will be dispersed throughout the environment (Al-Omari et al 2012; Yoshinaga et al., 2014).

It is well established that an increase in the levels of certain elements can be attributed to contributions from a variety of different sources. For example, the presence of carpet and the use of galvanized iron roofing are two of the significant sources that contribute to the high levels of Zn that have been found in house dust. Zinc compounds are put to use in the vulcanization step of the manufacturing process for rubber (Cheng et al., 2018; Daru et al., 2012). In addition, homes situated close to roads are likely to have elevated concentrations of the heavy metals of Zn, Pb, and Cd because of the constant abrasion caused by passing vehicles. Ni and Cr are widely used in residential areas to prevent corrosion in office furniture and metal plating (Naimabadi et al., 2021; Doyi et al., 2019, Cheng et al., 2018).

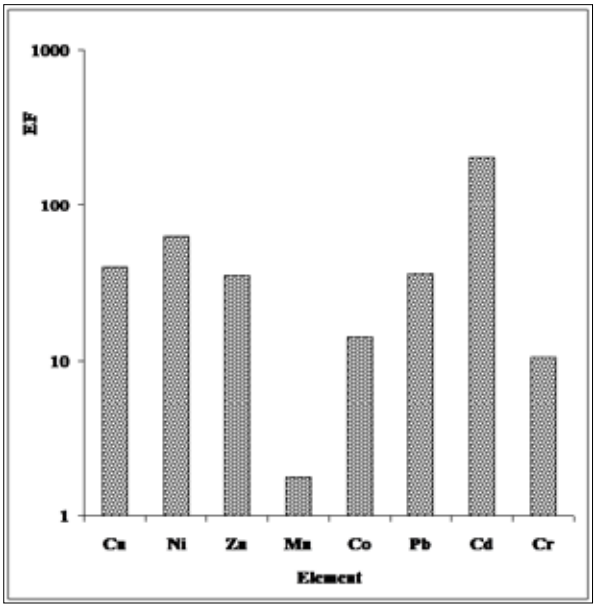

Figure 1. Crustal enrichment factors of measured elements in house dust samples.

3.4. Principal component analysis

Factor analysis was performed using the SPSS program package with varimax rotation to improve the orthogonality of resolved factors. The varimax rotated principal factor patterns for the four-factor groups (Eigenvalues > 1) explained 72.4% of the total variance (Table 2). The last column in the Table contains the communalities for the observed concentrations. The communality for an element reflects the percentage of the observed concentration that has been explained by the specific factors (sources).

The first component consists of the elements Co, Pb, and Cd. All of these elements are anthropogenic in nature. Pb, on the other hand, is commonly used as a marker element for motor vehicle emissions, so this factor has been designated as the automobile emissions factor. The second is heavily laden with Fe and Mn. These two elements are typically regarded as crustal sources. The communality for these two elements was approximately 90%, implying that approximately 10% of the observed Fe and Mn could not be explained by this system. Zn and Cu were heavily loaded on the third factor. Many smelting processes emit these two elements simultaneously. Furthermore, Cu and Zn are the primary constituents of Cu-Zn brass alloys. Thus, this factor may be interpreted as an anthropogenic factor related to the Cu and Zn industries (Isley et al., 2022).

The fourth factor had a significant loading by both Ni and Cr. These two elements are commonly found in residential areas due to their widespread use in the manufacture of office furniture and metal plating for corrosion prevention. Thus this factor is related to stainless steel (Yoshinaga et al., 2014).

4. Conclusion

According to the findings of this study, the indoor house dust found in Irbid City does not contain a high level of contamination. Heavy metals were found to be present in higher concentrations in and around highly populated areas with heavy traffic. According to the results of the enrichment factor, the levels of the following elements: Co, Ni, Zn, Co, and Cd are significantly enriched in house dust in comparison to their concentrations in nature. The combination of dust from inside and outside is the reason for the elevated levels of these elements. Calculations based on a factor analysis revealed that the outdoor dust from a variety of sources, which is typically brought inside by foot traffic, has a significant impact on the quality of the indoor environment.

Acknowledgments

We would like to express our gratitude to Yarmouk University for the financial support they have provided. The authors would like to extend their appreciation to the families that agreed to take part in the study and welcomed us into their homes.

Table 3. Rotated component matrix for house dust samples.

Variable	Factor1	Factor2	Factor3	Factor4	Communality
Cu	0.11	-0.17	**0.83**	-0.11	0.75
Ni	0.19	0.22	-0.03	**0.81**	0.74
Zn	-0.20	0.18	**0.79**	0.04	0.66
Mn	0.21	**0.89**	-0.09	-0.13	0.86
Co	**0.82**	-0.06	-0.33	-0.18	0.74
Pb	**0.79**	-0.20	0.14	0.17	0.70
Cd	**0.74**	-0.12	-0.02	-0.01	0.63
Cr	-0.35	0.32	0.16	**0.73**	0.73
Fe	0.14	**0.91**	0.07	0.17	0.86
%Variance	23.0	17.7	16.0	14.0	
Total Variance Explained, (%)					**73.0**

Conflict of Interests

The authors declare that there are no conflicts of interest regarding the publication of this paper.

References

Alghamdi, A.G., EL-Saeid, M.H., Alzahrani, A.J., Ibrahim, H.M. (2022). Heavy metal pollution and associated health risk assessment of urban dust in Riyadh, Saudi Arabia. PLoS ONE 17(1): e0261957.

Al-Madanat, O., Jiries, A., Batarseh, M., Al-Nasir, F. (2017). Indoor and Outdoor Pollution with Heavy Metals in Al-Karak City, Jordan. Journal of International Environmental Application & Science 12(2): 131-139.

Al-Massaedh, A. A., Al-Momani, I. F. (2020). Assessment of Heavy Metal Contamination in Roadside Soils along Irbid-Amman Highway, Jordan by ICP-OES. Jordan Journal of Chemistry 15(1): 1-12.

Al-Momani, I.F., Attiyat, A.S., Al-Momani, R.M. (2015). Influence of Different Heating Systems on the Bioavailable Fractions of Some Elements in House Dust. Jordan Journal of Chemistry 10(3): 194-204.

AL-Momani, I.F., Daradkeh, A.S., Haj-Hussein, A.T., Yousef, Y.A., Jaradat, Q.M., and Momani, K.A. (2005). Trace elements in daily collected aerosols in Al-Hashimya, central Jordan. Atmospheric Research 73: 87-100.

Al-Momani, I.F. (2007). Trace Elements in Street and Household Dusts in Amman, Jordan. Soil and Sediment Contamination 16(5): 485-496.

Al-Omari, A., Obeidat, S.M., Attiyat, A.S., Massadeh, A.M., Al-Momani, T.M., Al-Momani I.F. (2012). The Chemical Speciation of Trace-Metals in Street Dusts of Irbid, Jordan. Jordan Journal of Chemistry 7(4): 339-348.

Cheng, Z., Chen, L., Li, H., Lin, J., Yang, Z., Yang, Y., Xu, X., Xian, J., Shao, J., Zhu, X. (2018). Characteristics and health risk assessment of heavy metals exposure via household dust from urban area in Chengdu, China. Science of the Total Environment 619–620: 621–629.

Darus, F.M., Nasir, R.A., Sumari, S.M., Ismail, Z.S., Omar, N.A. (2012). Heavy Metals Composition of Indoor Dust in Nursery Schools Building. Procedia - Social and Behavioral Sciences 38: 169-175.

Doyi, I.N.Y., Isley, C.F., Soltani, N.S., Taylor, M.P. (2019). Human exposure and risk associated with trace element concentrations in indoor dust from Australian homes. Environment International 133: 105125.

Gul, H.K., Gullu, G., Babaei, P., Nikravan, A., Kurt-Karakus P.B., Salihoglu G. (2023). Assessment of house dust trace elements and human exposure in Ankara, Turkey. Environmental Science Pollution Research 30: 7718–7735.

Isley, C.F., Fry, K.L., Liu, X., Filippelli, G.M., Entwistle, J.A., Martin, A.P., Kah, M., Meza-Figueroa, D., Shukle, J.T., Jabeen, K., Famuyiwa, A.O., Wu, L., Sharifi-Soltani, N., Doyi, I.N.Y., Argyraki, A., Ho, K.F., Dong, C., Gunkel-Grillon, P., Aelion, M., Taylor, M.P. (2022). International Analysis of Sources and Human Health Risk Associated with Trace Metal Contaminants in Residential Indoor Dust. Environmental Science and Technology 56 (2): 1053-1068.

Khudhur, N., Khudhur, S.M., Ahmed, I. (2018). An Assessment of Heavy Metal Soil Contamination in a Steel Factory and the Surrounding Area in Erbil City. Jordan Journal of Earth and Environmental Sciences 9(1): 1-11.

Kim, N., Fergusson, J. (1993). Concentrations and sources of cadmium, copper, lead and zinc in house dust in Christchurch, New Zealand. Science of the Total Environment 138: 1-21.

Kurt-Karakus, P.B. (2012). Determination of heavy metals in indoor dust from Istanbul, Turkey: estimation of the health risk. Environment International 50: 47–55.

Madadi, R., Mohamadi, S., Rastegari, M., Karbassi, A., Rakib, M.R.J., Khandaker, M.U., Faruque, M.R.I., Idis, A.M. (2022). Health risk assessment and source apportionment of potentially toxic metal(loid)s in windowsill dust of a rapidly growing urban settlement, Iran. Scientific Reports 12:19736.

Mashal, K., Salahat, M., Al-Qinna, M., Ali, Y. (2017). Assessment of Heavy Metals in Topsoil of Al Hashmiyya City of Jordan. Jordan Journal of Earth and Environmental Sciences 8(2): 61-67.

Morawska, L., Salthammer, T. (eds.). (2003). Indoor Environment: Airborne Particles and Settled Dust. Wiley-VCH, Weinheim.

Naimabadi, A., Gholami, A., Ramezani, A. M. (2021). Determination of heavy metals and health risk assessment in indoor dust from different functional areas in Neyshabur, Iran. Indoor and Built Environment 30(10): 1781–1795.

Rasmussen, P.E., Levesque, C., Chenier, M., Gardner, H.D., Jones-Otazo, H., Petrovic, S. (2013). Canadian House Dust Study: population-based concentrations, loads and loading rates of arsenic, cadmium, chromium, copper, nickel, lead, and zinc inside urban homes. Science of the Total Environment 443: 520–529.

Rasmussen, P.E., Subramanian, K.S., Jessiman, B.J. (2001). A multi-element profile of house dust in relation to exterior dust and soils in the city of Ottawa, Canada. Science of the Total Environment 267:125–140.

Rudnick R. L., Gao S. (2003). Composition of the Continental Crust, Treatise on Geochemistry, Volume 3, pp 1-64.

Shi, T., Wang, Y. (2021). Heavy metals in indoor dust: Spatial distribution, influencing factors, and potential health risks. Science of the Total Environment, 755: 142367.

Tan, S. Y., Praveena, S. M., Abidin, E. Z., and Cheema, M. S. (2016). A Review of Heavy Metals in Indoor Dust and its Human Health-Risk Implications. Reviews Environmental Health 31 (4), 447–456.

Tarawneh, K., Eleyan, I., Alalwan, R., Sallam, S., Hammad, S. (2021). Assessment of heavy metals contamination levels in surfaces soil in Baqa'a area, Jordan. Jordan Journal of Earth and Environmental Sciences 12(3): 285-294.

Tong S.T.Y., Lam K.C. (2000). Home sweet home. A case study of household dust contamination in Hong Kong. The Science of the Total Environment 256(2–3):115–123.

Yoshinaga, J., Yamasaki, K., Yonemura, A., Ishibashi, Y., Kaido, T., Mizuno, K., Takagi, M., Tanaka, A. (2014). Lead and other elements in house dust of Japanese residences – sources of lead and health risks due to metal exposure. Environmental Pollution 189: 223–228.

JJEES

JJEES (2024) 15 (2): 82-93
ISSN 1995-6681

Jordan Journal of Earth and Environmental Sciences

Black Carbon Concentration in the District of Ar-Ramtha, Northern Jordan, and its Sources at Seven Wavelengths

Abdallah M. Mallak[1], Khadeejeh M. Hamasha[1*], Manal J. Abdallah[1]

[1]Physics Department, Yarmouk University, Jordan

Received March 1, 2023; Accepted September 13, 2023

Abstract

Variations of black carbon concentration and its sources identification were studied in Ar-Ramtha District , north of Jordan, using the aetlalometer model AE33. Measurements at six sites showed that the black carbon concentrations almost have the same behavior due to the uniform nature of the region. The average value of the black carbon concentration in the six sites was 1778 ng/m^3, 2288 ng/m^3, 1605 ng/m^3, 1785 ng/m^3, 2267 ng/m^3, and 2606 ng/m^3 respectively. Analysis of the measurements and Angstrom exponents, pre-calibrated in the instrument, revealed the ability of these variations to apportion black carbon from its sources. The largest contribution of black carbon was from fossil fuels at all sites. The absorption coefficients for each wavelength were measured at all sites. For a wavelength of 370 nm, it was discovered that the absorption coefficient had a maximum value of 58. 27Mm-1 while it it was 20.25 Mm^{-1} at 880 nm. In all sites, the average absorption coefficients reached their highest value at a wavelength of 370 nm, demonstrating the inverse relationship between wavelength and absorption coefficient.

Keywords: Black carbon, Aethalometer AE33, Ar-Ramtha District, Absorption coefficient, Angstrom exponent, Fossil fuel

1. Introduction

Black carbon (BC) is one of the elements that contribute to global warming by absorbing light from the atmosphere. It makes a significant contribution to global warming processes since it can influence local clouds and precipitation patterns (Abu Sada et al. 2015). As a result, its contribution to climate warming is on par with that of carbon dioxide (Bond et al., 2013). Because of its diminutive size that is less than 2.5 μm in diameter and ease of body penetration, BC has a detrimental effect on human health because it is the cause of numerous respiratory disorders (Janssen et al., 2012; Wang et al., 2017; Wang et al., 2021). In addition, these fine particles depend on the variability of weather parameters (Ali-Saleh et al., 2019, Al-Qinna 2018). In addition, due to its capacity to absorb nutrients crucial to plant growth, black carbon also has an impact on soil fertility (Glaser and Bruno, 2007).

Black carbon has been the subject of several recent studies in Jordan (Hamasha and Arnott 2009; Hamasha et al. 2010). Over the past 20 years, black carbon in Jordan has been increasing continuously, according to a recent research utilizing satellite data (Hamasha 2021). The main sources of black carbon in Jordan include transportation, industrial activity, and residential combustion activities such as cooking and heating. These findings highlight the need for effective legislation and regulations that will reduce Jordan's black carbon emissions while also improving the air quality and nation's overall health. The aethalometer type AE33 (Figure 1) was used in this investigation to assess the amount of black carbon and its sources (Fialho et al., 2005; Healy et al., 2017; Lack et al., 2013; Lu et al., 2015; Saleh et al., 2014) in the Ar-Ramatha region.

Figure 1. The Aethalometer AE33 in operation

2. Materials and Methods

In this study, measurements of BC were done in six different locations in Ar-Ramtha District. Ar-Ramtha District is located in the north of Jordan, near the Syrian-Jordanian border, opposite the Syrian city of Dar'a (Figure 2). It has an area of 485 km^2. The climate of Ar-Ramtha District is relatively dry. Due to its location on the verge of a desert area, it has a climate more like to that of the desert or a continental region, with hot, dry summers and rainy winters. Around 150–200 millimeters of precipitation fall annually in the eastern region, compared to 250–350

* Corresponding author e-mail: khamasha@yu.edu.jo

mm in the western and northern parts. The average daily temperature in summer is 25 degrees Celsius. Since 2011, Syrian refugees have a wide range of complex effects on Ar-Ramtha's surroundings. Land use, trash management, energy use, and water resources have been all impacted. Ar-Ramtha's expanding population has led to an increase in energy consumption. Due to increasing air pollution and greenhouse gas emissions, providing electricity to migrants via generators and other energy sources potentially harmful to the environment. The arrival of refugees in Ar-Ramtha has also led to a more demand in housing and infrastructure needs, which could endanger ecosystems and natural habitats. As a result, local ecosystem services and biodiversity may suffer.

Figure 2. A map of Jordan showing the location of the district of Ar-Ramtha in northern Jordan.

Measurements of BC were done using Aethalometer AE33. According to Virkkula et al. (2007), the equipment used in the measuring process attenuates light by depositing black carbon on the filter tape. The device supports DualSpot technology by simultaneously examining the light absorption by the deposits gathered at two parallel locations on the filter tape at varying loading rates (Drinovec et al., 2015). The Aethalometer AE33 is a device that measures the light absorption on a filter that has particles in it to estimate the amount of black carbon in the air in the present moment. The AE33 can provide accurate results in as little as one-minute using DualSpot technology and multi-wavelength optical analysis. The air sample is drawn through the instrument's input using an external pump operating at 5 liters per minute. The sample is put twice onto the filter tape once it has entered the optical chamber, each time at a different speed. The instrument analyzes the sample optically by comparing the quantity of light that passes through two places with the sample to the amount of light that goes through a loaded section of the filter tape in the reference region at wavelengths of 370, 470, 520, 590, 660, 880, and 950 nm. A detector on the other side gauges the amount of light that is transferred. Since the instrument is characterized by accumulated deposition of the sample on the filter, calculating the concentration of black carbon depends on the change in light attenuation every minute (Figure 3).

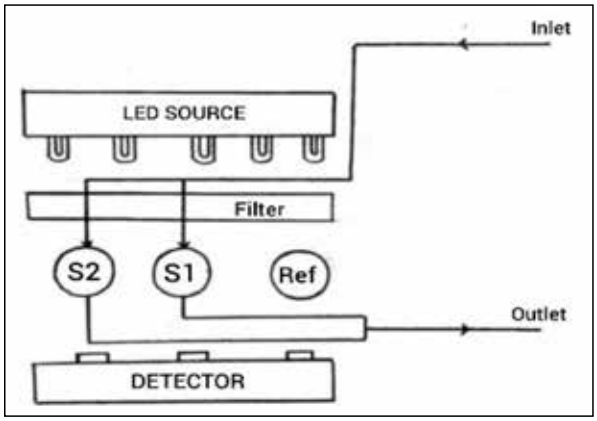

Figure 3. Schematic diagram of the optical analysis process of the sample on the filter.

The attenuation can be estimated using the signals. The detector reported using the formulas below:

$$\mathrm{ATN} = -100 \ln\left(\frac{I}{I_o}\right) \quad (1)$$

where the detector signals for the measurement location are I and the reference spot's detector signal is Io. The ratio, also known as the filter transmittance, reflects the amount of light that passes through the filter. In equation (1), the number 100 is included for convenience. The leakage factor () must be taken into consideration because the airflow is gauged after it goes through the filter. The optical chamber's lateral airflow is

$$F_{in} = F_{out} \times (1 - \zeta) \quad (2)$$

where F_{out} is the flow leaving the system after the filter, and F_{in} is the flow entering the input port. Consequently, the attenuation coefficient can be determined using

$$b_{atn} = S \times \frac{(\Delta ATN/100)}{F_{in}\Delta t} \quad (3)$$

where Δt is the time interval and S is the spot area.

The optical absorption of the filter deposits is impacted because the filter material scatters some of the incident light. According to Drinovec et al. (2015), factor C, which is dependent on the filter material, describes the amplification of optical absorption. The updated absorption factor b_{abs} is,

$$b_{abs} = \frac{b_{ATN}}{C} \quad (4)$$

The letter C (Weingartner et al. 2003) represents the multiple scattering parameter. Employing the relation, BC concentration is determined from the absorption coefficient.

$$BC = \frac{b_{abs}(\lambda)}{\sigma_{air}(\lambda)} \quad (5)$$

Where, σ is the mass absorption cross-section at wavelength λ. The values of σ at the seven wavelengths used in the AE33 observations are displayed in Table 1.

Table 1. Wavelength along with the cross-sectional area

λ (nm)	(m^2/g)
370	18.47
470	14.54
520	13.14
590	11.58
660	10.35
880	7.77
950	7.19

$$BC = \frac{BC_{measured}}{(1-k*ATN)} \quad (6)$$

where the compensating factor k is used. Seven wavelengths are tested simultaneously for optical absorption. The carbon black concentration is reported using data collected at an 880 nm wavelength. According to Sandradewi et al. (2008a, 2008b), the basis for source splitting of black carbon emissions is the wavelength dependence of the absorption coefficient. The optical absorption coefficient is the product of the absorption coefficient for burning biomass and the absorption coefficient for fossil fuels

$$b_{abs} = (b_{abs})_{ff} + (b_{abs})_{bb} \quad (7)$$

where, is the optical absorption parameter of the biomass burning, and (is the optical absorption parameter of the fossil fuels.

So,

$$BC = BC_{bb} + BC_{ff} = \frac{b_{abs}}{\sigma_{air(\lambda=880nm)}} \quad (8)$$

where, is BC of biomass burning source, and is BC of fossil fuels source. The equivalent black carbon produced by burning fossil fuels and biomass is thought to be well indicated by the absorption of near ultraviolet (UV) and infrared (IR) radiation, respectively. An important factor in identifying the origins of black carbon emissions is the optical absorption coefficient, which results from the burning of both biomass and fossil fuels. The AE33 model posits that emissions from burning fossil fuels and biomass follow spectrum dependences of λ^{-1} and λ^{-2} respectively. It is based on the difference in absorption coefficient wavelength dependence. The exponents that characterize the spectrum dependency are known as Angstrom exponents, and they are $\alpha_{ff} = 1$ for burning fossil fuels and $\alpha_{bb} = 2$ for burning biomass (Ran, L. et al. 2016).

Assessment of BC_{ff} and BC_{bb} contributions to the overall measured b_{abs} (λ) (component apportionment) is possible using the AE33 model,

$$b_{abs}(470nm) = b_{abs}(470nm)_{ff} + b_{abs}(470nm)_{bb} \quad (9)$$

$$b_{abs}(950nm) = b_{abs}(950nm)_{ff} + b_{abs}(950nm)_{bb} \quad (10)$$

In the source apportionment for AE33, the wavelength pairs 370 – 950 nm, 370-880 nm, 470-880 nm, and 470-950 nm were taken into account.

Biomass burning percentage BB (%) is:

$$BB(\%) = \frac{b_{abs}(950nm)_{bb}}{b_{abs}(950nm)} \quad (11)$$

The proportions of biomass burning and fossil fuels are then computed as follows:

$$BC_{bb} = BB \times BC \quad (12)$$

$$BC_{ff} = (1 - BB) \times BC \quad (13)$$

3. Results and Discussion

The field study was conducted in six different sites in Ar-Ramtha District to measure the black carbon concentrations using an Aethalometer AE33. Figure 4 shows the study areas in Ar-Ramtha District. The study regions were chosen based on the availability of various sources that contribute to the concentration of black carbon from burning fossil fuels and biomass. The data used in this study are from six separate days of measurements. Each measurement was conducted during all daytime.

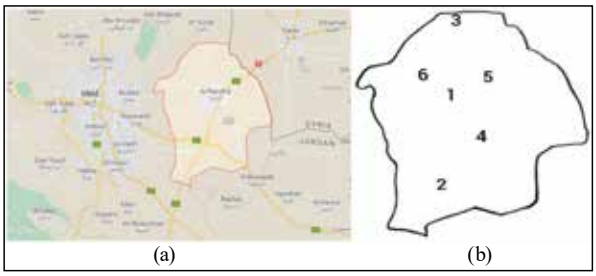

Figure 4. (a) The location of Ar-Ramtha District, north of Jordan, with respect to Irbid City and Syria boarder (b) the location of the study sites in Ar-Ramtha District

The study was conducted in the summer of 2021. The measurements were recorded by AE33 with a time resolution of one minute for a steady flow of aerosol samples (5 liters per minute). With the help of measured data from the instrument, this study examined the characteristics of the spatial and temporal patterns of black carbon to identify the origin of the BC concentration. The information utilized in this investigation is from measurements taken on six different days (Table 2). The six research sites in Ar-Ramtha District were carefully chosen in order to cover the entire region from north to south and from east to west. The southern region was chosen as the first location of Jordan University of Science and Technology (JUST), while the second site was selected in the north along the road going to Turrah . The third site was picked next to the Al-Shaqran station in the west and the fourth one was near Ar-Ramtha Government Hospital on the international route with Syria in the east. Additionally, an extremely crowded location was selected close to the Ar-Ramtha Health Center in the city center as the fifth site. The sixth location is near the Department of Licensing on the international route with Iraq in the district's southwest. Due to the limited availability and expensive cost of our aethalometer (AE33), we were unable to run the experiment simultaneously in all locations, so we did it over the course of several days. Because the locations are so close to one another and the local characteristics are the only ones that vary, it is reasonable to predict that the findings will be close. The most significant local factor is the crowdedness of the vehicles, which raises the level of atmospheric black carbon. Due to road closures at the time of the Corona pandemic, the inside routes are more congested with vehicles than the external ones.

Table 2. The study areas, date, area name, and properties.

Site #	Date	Area name	Properties
1	28/06/2021	Ar-Ramtha Comprehensive Health Center	The site is subject to the constant movement of vehicles and a populated area.
2	29/06/2021	The campus of the Jordan University of Science and Technology	The site is empty of students and has green cover
3	05/07/2021	Near the Northern Turrah Primary Health Center's	The site is subject to the constant movement of vehicles and a populated area.
4	07/07/2021	Near the Licensing Department	The site is on a public street, and it is highly subject to the constant movement of vehicles.
5	28/07/2021	Near Ar-Ramtha Government Hospital	The site is subject to the constant movement of vehicles, frequently populated, and surrounded by some cafes.
6	02/08/2021	Near the Al Shagran Gas Station	The site is on a public street, and it is highly subject to the constant movement of vehicles.

3.1. Variation of Black Carbon Concentration with Time

At each study site, the measurement represented the variance in the concentration of black carbon from burning biomass and fossil fuels (Figures 5 –10). Figure 5 shows that BC concentration in the first site varied between 772 ng/m^3 and 5177 ng/m^3. 92.94% of them were from fossil fuel sources.

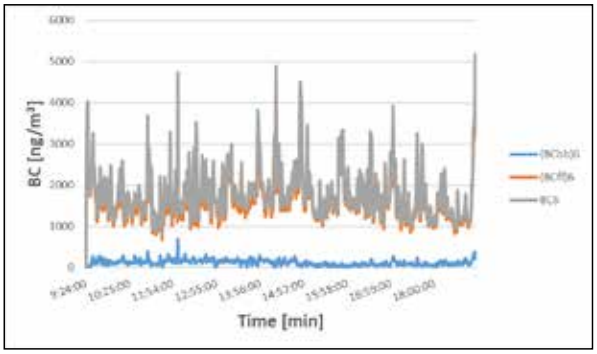

Figure 5. Variation of black carbon concentration from biomass burning and fossil fuel sources during the measurement in the first site on 28/06/2021

Figure 6 shows that BC concentration in the second site varied between 1002 ng/m^3 and 8030 ng/m^3. 89.65%of them were from fossil fuel sources.

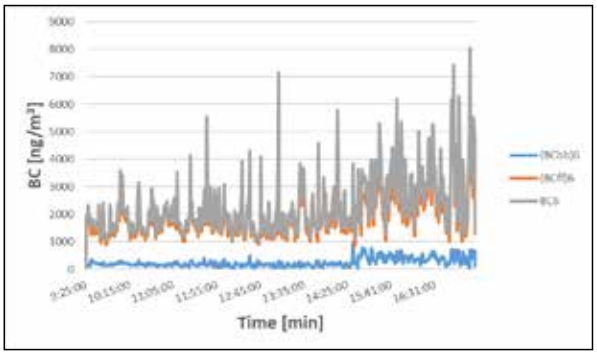

Figure 6. Variation of black carbon concentration from biomass burning and fossil fuel sources during the measurement in the second site on 29/06/2021

Figure 7 shows that BC concentration in the third site varied between 411ng/m^3 and 14299 ng/m^3.89.52% of them were from fossil fuel sources.

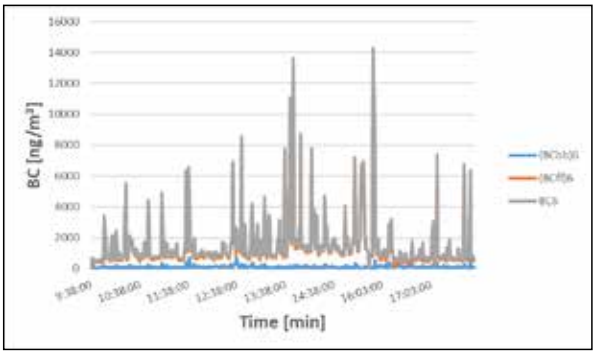

Figure 7. Variation of black carbon concentration from biomass burning and fossil fuel sources during the measurement in the third site on 05/07/2021

Figure 8 shows that BC concentration in the fourth site varied between 765 ng/m^3 and 9378 ng/m^3.95.15% of them were from fossil fuel sources.

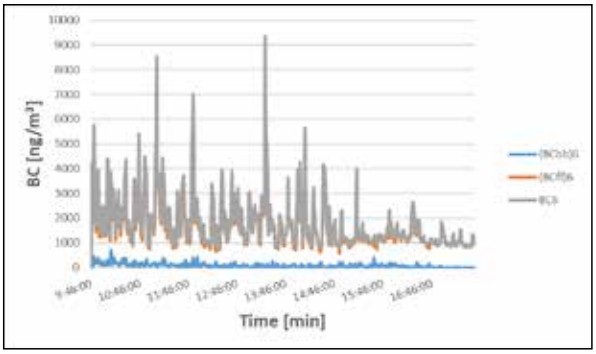

Figure 8. Variation of black carbon concentration from biomass burning and fossil fuel sources during the measurement in the fourth site on 07/07/2021

Figure 9 shows that BC concentration in the fifth site varied between 850 ng/m^3 and 8526 ng/m^3. 91.15% of them were from fossil fuel sources.

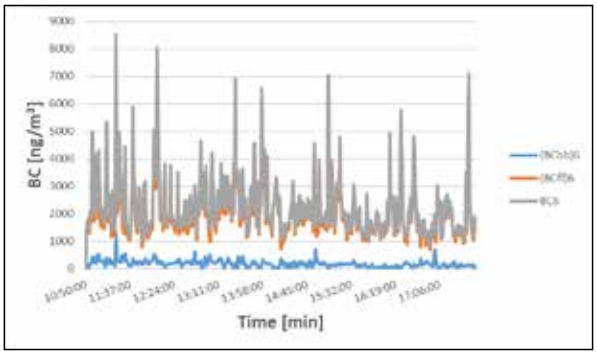

Figure 9. Variation of black carbon concentration from biomass burning and fossil fuel sources during the measurement in the fifth site on 28/07/2021

Figure 10 shows that BC concentration in the sixth site varied between 989 ng/m^3 and 16372 ng/m^3. 85.23% of them were from fossil fuel sources.

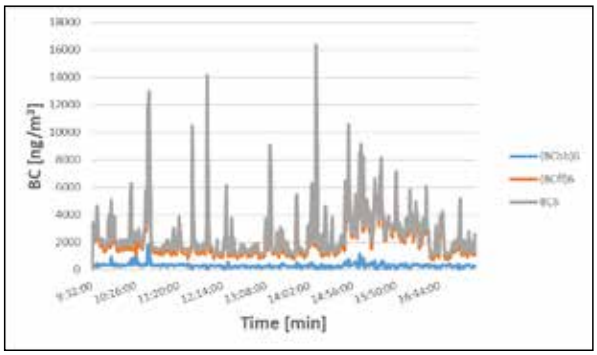

Figure 10. Variation of black carbon concentration from biomass burning and fossil fuel sources during the measurement in the sixth site on 02/08/2021

The average concentrations of BC during the measurements for all sites varied between 1605 ng/m^3 and 2606 ng/m^3. As seen in Figure 11, most the BC concentrations are from fossil fuel sources. This result is expected because the most sources of black carbon in Ar-Ramtha District were mobile transportation. The largest concentrations in BC were from site 6. It is very crowded with vehicles as it connects Ar-Ramtha area to Irbid via villages east of Irbid such as Sal and Bushra. The second largest concentration of black carbon was at site 2, the site of Jordan University of Science and Technology. Although, there were no students at the time of the measurements except for some staff who were on duty. Besides, it is very close to King Abdullah Hospital, which is very busy all the time. The result of BC concentration is very high and comparable to an urban area like Barranquilla, a Caribbean city in Colombia (Blanco-Donado et al. 2022).

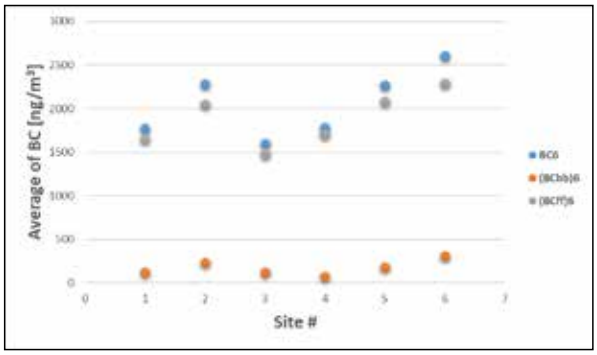

Figure 11. Average of black carbon concentration from biomass burning and fossil fuel sources during the measurement for all sites

3.2 Variation of Absorption Coefficients with Wavelengths

The absorption coefficients of the black carbon concentration from seven wavelengths were calculated based on the variation in the mass absorption cross-section of each wavelength during the measurement at each site. Figure 12 shows the time series of black carbon light absorption coefficients (b_{abs}) for the measurements at site 1 for the seven wavelengths (370nm, 470nm, 520nm, 590nm, 660nm, 880nm, and 950nm). The average b_{abs} of all wavelengths was 34.35 Mm^{-1}, 28.19 Mm^{-1}, 24.51 Mm^{-1}, 20.97 Mm^{-1}, 18.44 Mm^{-1}, 13.81 Mm^{-1}, and 13.05 Mm^{-1} respectively.

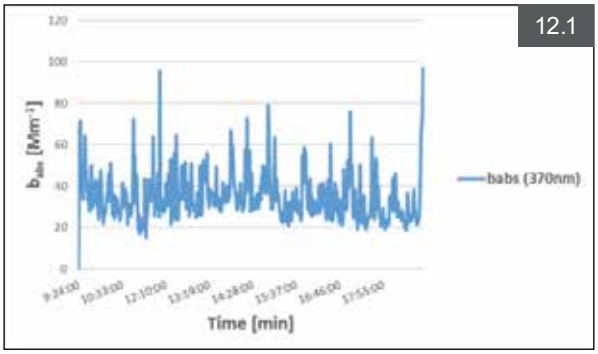

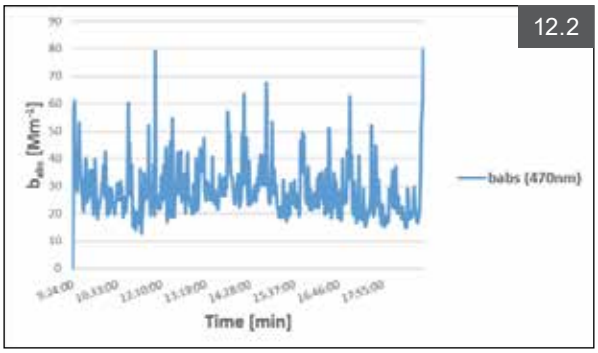

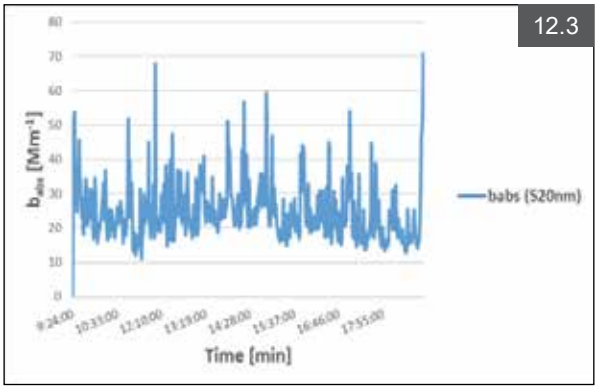

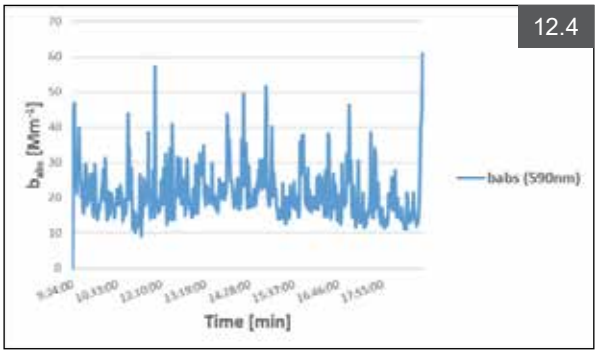

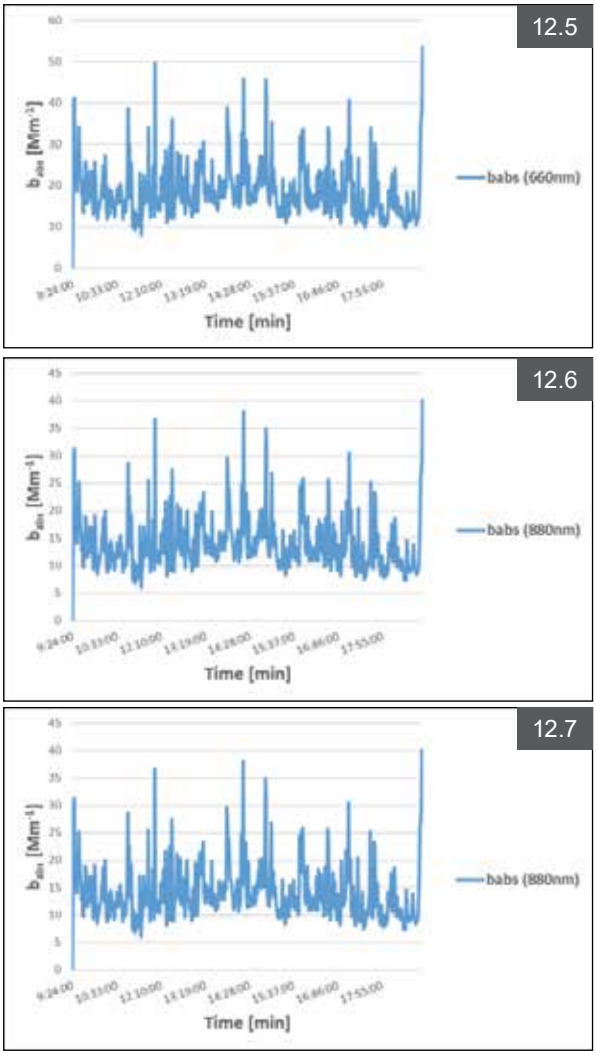

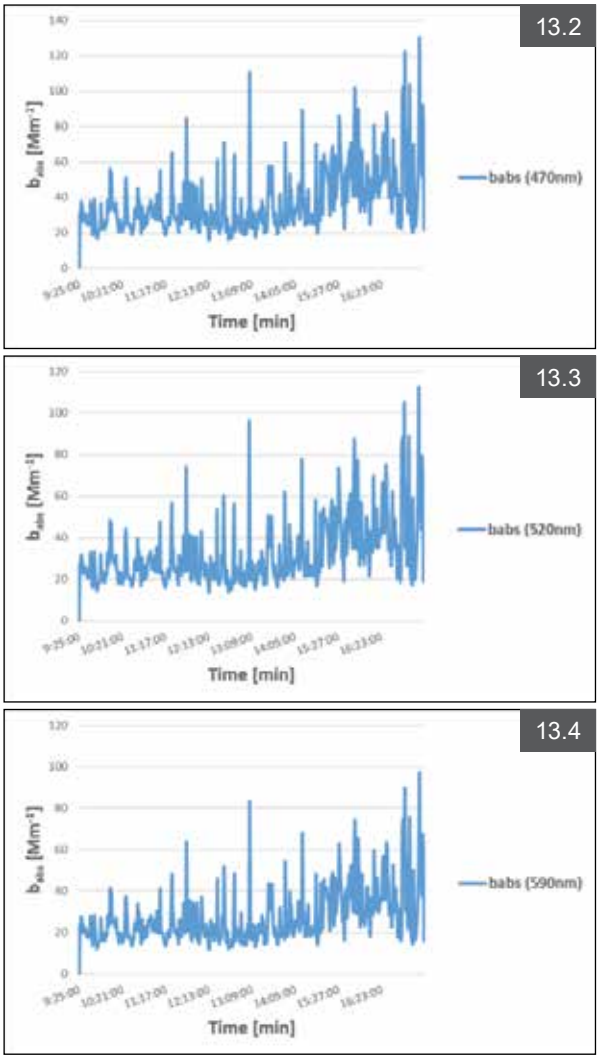

Figure 12. Variation in the absorption coefficients of black carbon during the measurement of the seven wavelengths in the first site on 28/06/2021

Figure 13 shows the time series of black carbon light absorption coefficients (b_{abs}) for the measurements at site 2 for the seven wavelengths (370nm, 470nm, 520nm, 590nm, 660nm, 880nm, and 950nm). The average b_{abs} of all wavelengths was 46.19 Mm^{-1}, 37.58 Mm^{-1}, 32.30 Mm^{-1}, 27.52 Mm^{-1}, 24.06 Mm^{-1}, 17.78 Mm^{-1}, and 16.82 Mm^{-1} respectively.

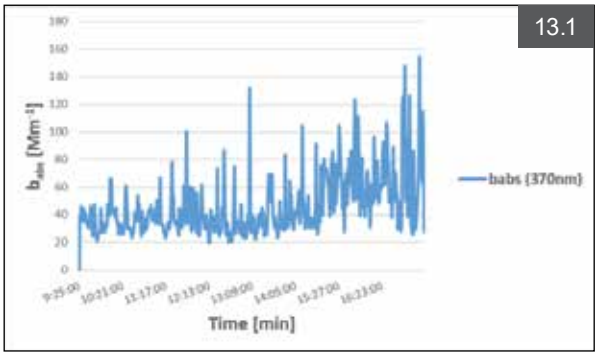

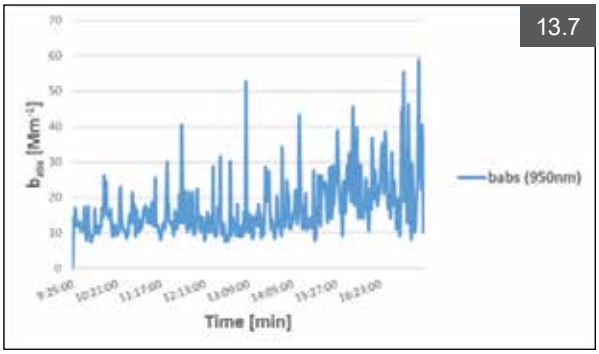

Figure 13. Variation in the absorption coefficients of black carbon during the measurement of the seven wavelengths in the second site on 29/06/2021

Figure 14 shows the time series of black carbon light absorption coefficients (b_{abs}) for the measurements at site 3 for the seven wavelengths (370nm, 470nm, 520nm, 590nm, 660nm, 880nm, and 950nm). The average b_{abs} of all wavelengths was 31.56 Mm^{-1}, 25.77 Mm^{-1}, 22.38 Mm^{-1}, 19.28 Mm^{-1}, 16.94 Mm^{-1}, 12.47 Mm^{-1}, and 11.93 Mm^{-1} respectively.

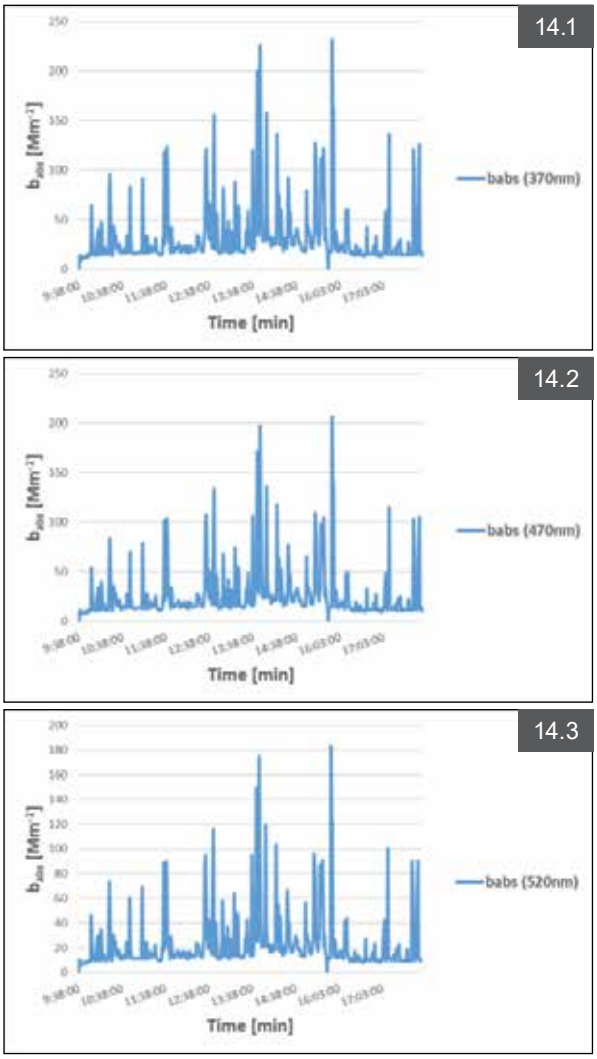

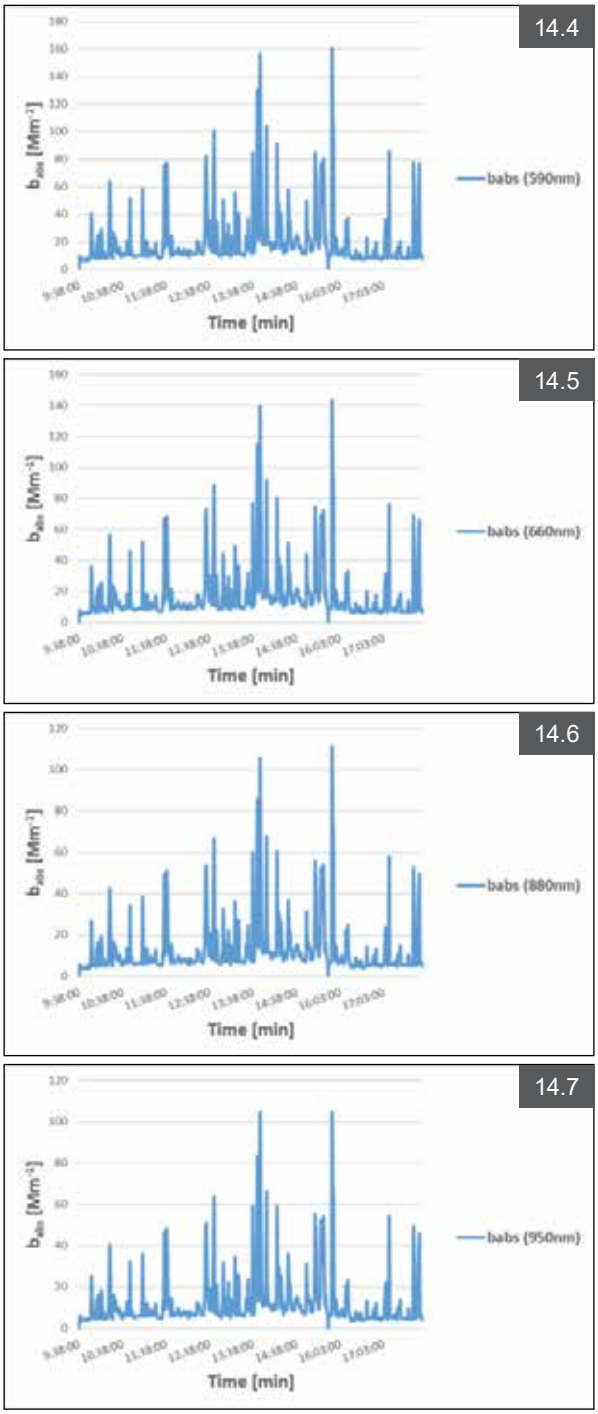

Figure 14. Variation in the absorption coefficients of black carbon during the measurement of the seven wavelengths in the third site on 05/07/2021

Figure 15 shows the time series of black carbon light absorption coefficients (b_{abs}) for the measurements at site 4 for the seven wavelengths (370nm, 470nm, 520nm, 590nm, 660nm, 880nm, and 950nm). The average b_{abs} for all wavelengths was 34.10 Mm^{-1}, 28.28 Mm^{-1}, 24.64 Mm^{-1}, 21.39 Mm^{-1}, 18.85 Mm^{-1}, 13.87 Mm^{-1}, and 13.52 Mm^{-1} respectively.

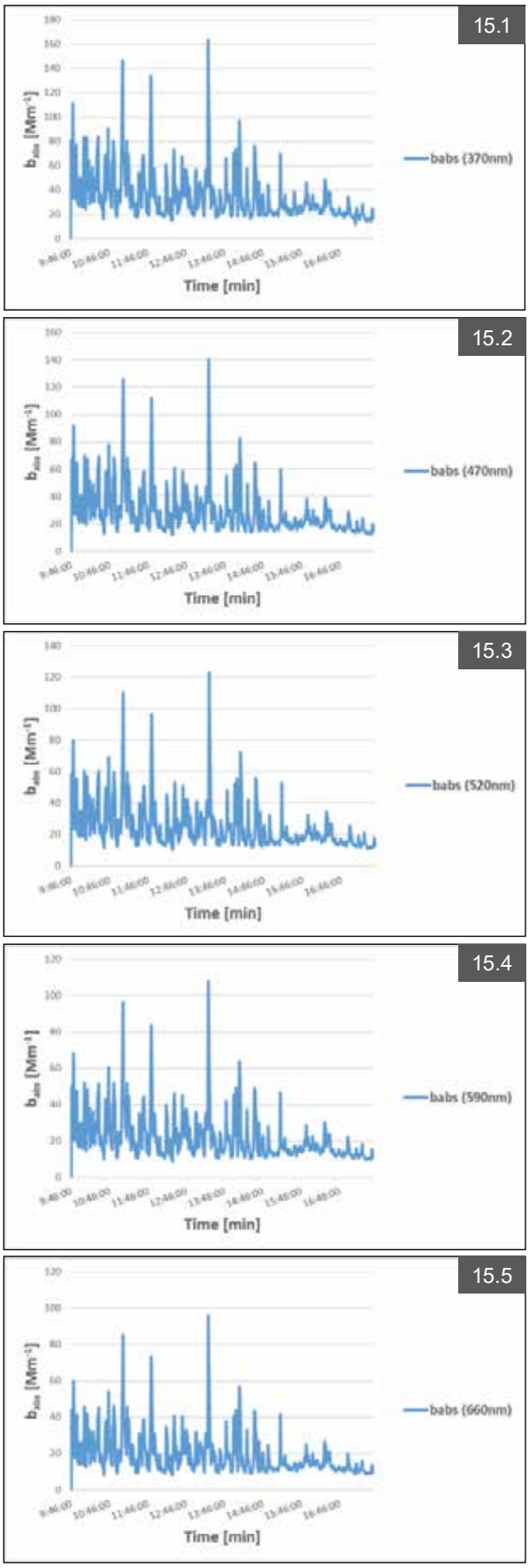

Figure 15. Variation in the absorption coefficients of black carbon during the measurement of the seven wavelengths in the fourth site on 07/07/2021

We note that the average values of the absorption coefficients of the seven wavelengths at sites 1 and 4 are identical. This similarlity indicates uniform nature of the two sites in terms of the availability of black carbon sources. Figure 16 shows the time series of black carbon light absorption coefficients (b_{abs}) for the measurements at site 5 for the seven wavelengths (370nm, 470nm, 520nm, 590nm, 660nm, 880nm, and 950nm). The average b_{abs} for all wavelengths was 44.29 Mm^{-1}, 36.24 Mm^{-1}, 31.37 Mm^{-1}, 26.93 Mm^{-1}, 23.57 Mm^{-1}, 17.61 Mm^{-1}, and 16.60 Mm^{-1} respectively.

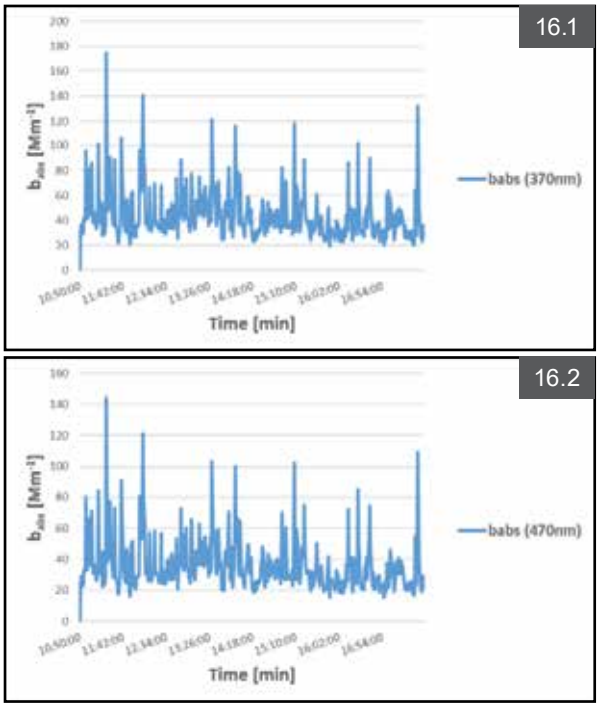

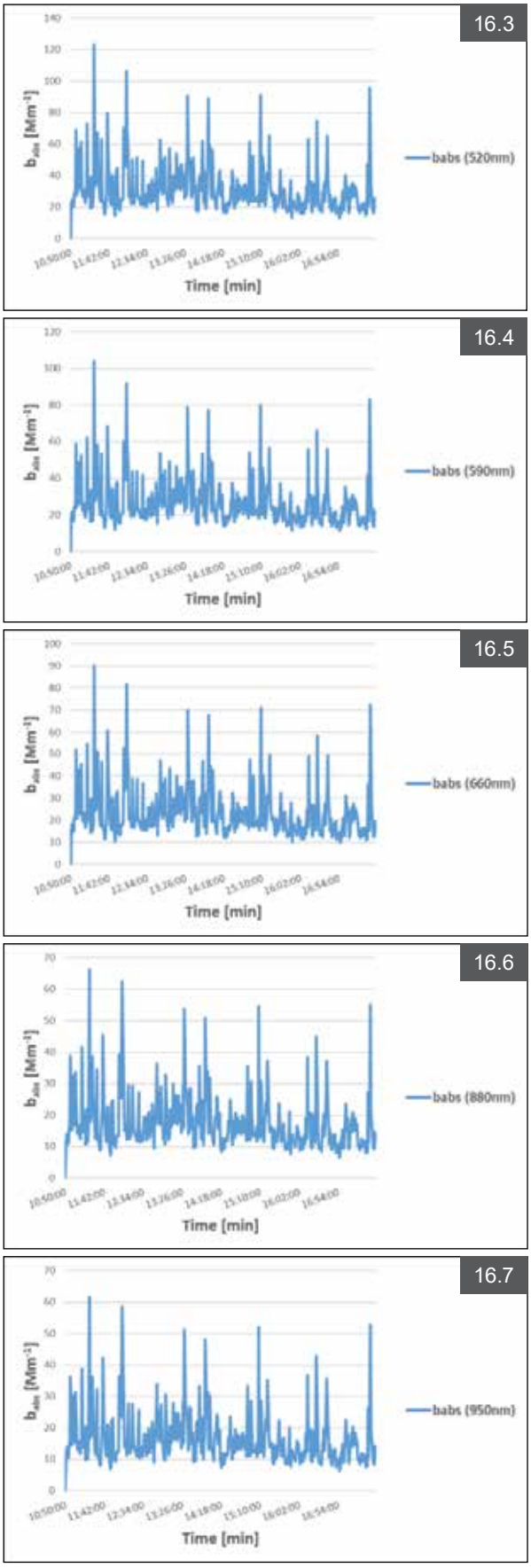

Figure 16. Variation in the absorption coefficients of black carbon during the measurement of the seven wavelengths in the fifth site on 28/07/2021

Figure 17 shows the time series of black carbon light absorption coefficients (b_{abs}) for the measurements at site 6 for the seven wavelengths (370nm, 470nm, 520nm, 590nm, 660nm, 880nm, and 950nm). The average b_{abs} for all wavelengths was 58.27 Mm^{-1}, 44.47 Mm^{-1}, 37.83 Mm^{-1}, 32.21 Mm^{-1}, 28.03 Mm^{-1}, 20.25 Mm^{-1}, and 19.66 Mm^{-1} respectively.

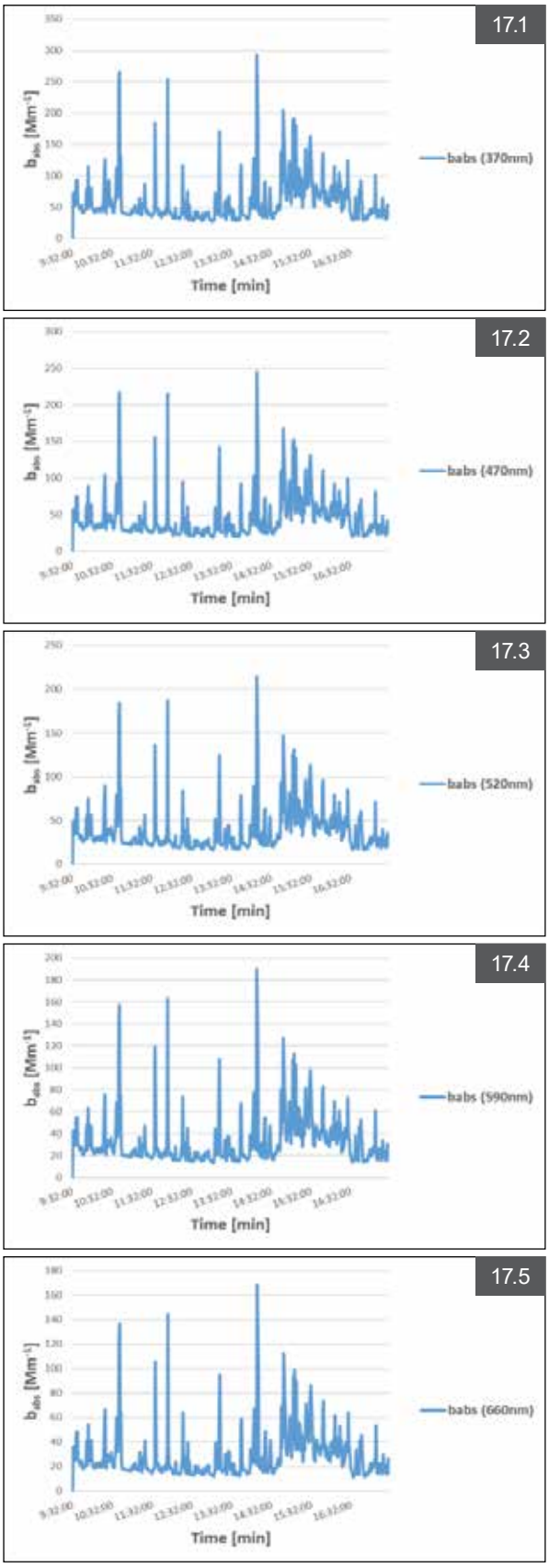

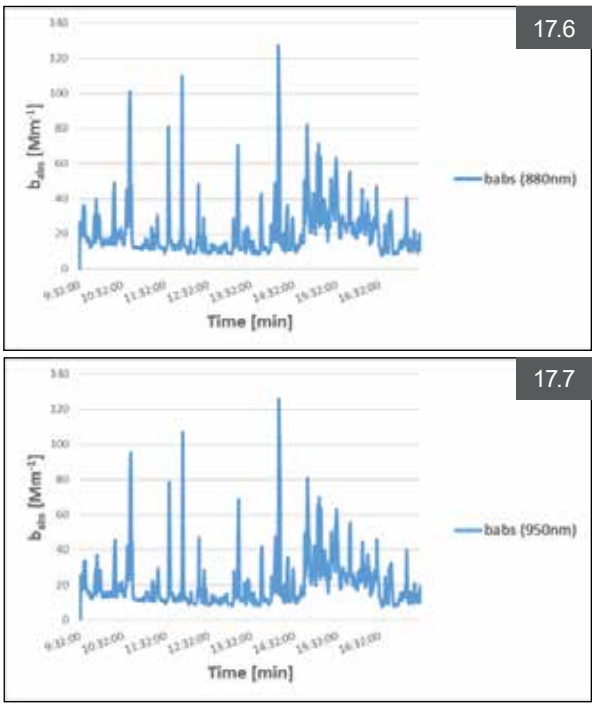

Figure 17. Variation in the absorption coefficients of black carbon during the measurement of the seven wavelengths in the sixth site on 02/08/2021

The average absorption coefficient values of the seven wavelengths were evaluated at six sites (Figure 18). It was found that the highest value was in site 6 because it is located on a public street, and it is subject to a greater degree of continuous movement of vehicles and population congestion than other sites. In addition, this site is considered the closest to the city of Irbid, which is considered one of the highest places in the concentration of black carbon in Jordan. It was found that the average values of the absorption coefficients in the six sites decreased with the increase of the wavelength because the absorption efficiency is proportional to the inverse of the wavelength. In addition, the values of the absorption coefficient at a defined wavelength are proportional to the size of the particles. This absorption process increases the air temperature and affects the climate because it removes energy from electromagnetic radiation and converts it into thermal radiation.

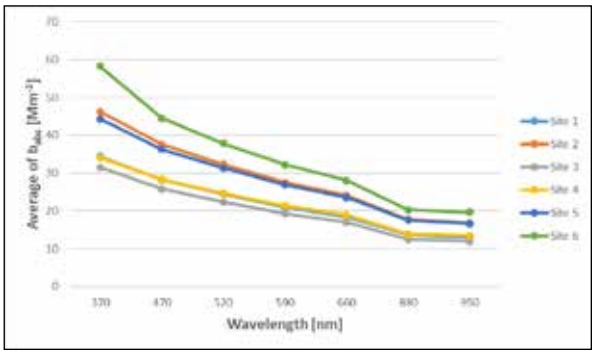

Figure 18. Average absorption coefficients of black carbon versus wavelength during measurements at different sites

Since the defining standard, used for reporting black carbon concentration, is at the wavelength of 880 nm, the average values of the absorption coefficients during the measurement campaign in Ar-Ramtha District were compared with a measurement in Irbid City, 20 km away from Ar-Ramtha. The average value of the absorption coefficient in Irbid City (Hamasha 2021) was (36.38Mm^{-1}) greater than in Ar-Ramtha District (15.96 Mm^{-1}). The reason is related to the combustion activities, population density, and overcrowded streets with buses and cars being more available in Irbid. In addition, it is related to the availability of cafes, shops, and restaurants that contribute to increasing the black carbon concentration. The measurement campaign in Ar-Ramtha was mostly in a less polluted, open, and less dense atmosphere population compared to the measurement campaign in Irbid.

Depending on the source, different BC concentrations have been discovered as having discernible effects on global warming. Even little increases in BC concentrations, according to reports, can have a big impact on the environment and people's health. The recommended yearly average limit for $PM_{2.5}$ (particulate matter with a diameter of less than 2.5 micrometers), as stated by the World Health Organization (WHO), is 10 g/m^3. Since black carbon is part of $PM_{2.5}$, lowering $PM_{2.5}$ concentrations can also aid in lowering black carbon emissions. The United Nations Framework Convention on climate change has developed rules and procedures for calculating and disclosing black carbon emissions in terms of global limits and measurements. The Climate and Clean Air Coalition has also established goals for lowering black carbon emissions in a number of industries, including brick manufacturing, transportation, and home energy. Numerous national standards and laws also govern the measurement and management of black carbon emissions.

3.3 The Role of the Angstrom Exponents (α) in Determining the Source of Black Carbon

The absorption exponent gives insight into the source of black carbon formation (Andreae and Gelencser 2006, Bergstrom et al. 2007). The role of the Angstrom exponents was evaluated in determining the contribution to the concentration of black carbon from its different sources during the measurement at all sites. It was found that the value absorption exponent of the measurements for all sites fluctuates around the value 1, which indicates the role of fossil fuels as the main contributor to the black carbon concentration (Table 3).

Table 3. Daily average absorption Angstrom exponent

Site #	Average Angstrom exponent
1	1.097
2	1.141
3	1.138
4	1.051
5	1.119
6	1.196

As can be seen in Table 3, the change of Angstrom exponent during the measurements in all sites fluctuates around 1 and is an indication of the major contribution of fossil fuels to the black carbon concentration.

4. Conclusion

The concentration of black carbon, which has a significant role in the global warming process, changes in the atmosphere depending on the geographical location and availability of its sources and is also affected by weather factors. The aethalometer AE33 provides real-time determination of the black carbon sources and percentages. The average value of all 6 sites in Ar-Ramtha district was found to be 2055 ng/m^3or 2.06μg/m^3 which is comparable to measurements done in urban areas. Analysis of measurements and angstroms pre-calibrated in the instrument revealed the ability to split black carbon from its sources. It was found that the source of fossil fuels is the dominant source of black carbon in the Ar-Ramtha region. It was also found that the absorption coefficient is inversely proportional to the wavelength.

Acknowledgment

The authors would like to thank Scientific Research and Graduate Studies Deanship at Yarmouk University, Jordan for supporting this work with Grant No. 18/2019.

Conflict of Interests

The authors declare that there are no conflicts of interest regarding the publication of this paper.

References

Abu Sada, A., Abu-Allaban M., and Al-Malabeh A., (2015), Temporal and Spatial Analysis of Climate Change at Northern Jordanian Badia, Jordan Journal of Earth and Environmental Sciences, 7 (2), ISSN 1995-6681, p. 87 – 93

Ali-Saleh, S., Shilbayeh Z., Alkattan H., Al-Refie M., Jaghbeir O., and Hussein T., (2019), Temporal Variations of Submicron Particle Number Concentrations at an Urban Background Site in Amman-Jordan, Jordan Journal of Earth and Environmental Sciences, 10 (1): ISSN 1995-6681, p. 7-14

Al-Qinna, M., (2018), Analyses of Climate Variability in Jordan using Topographic Auxiliary Variables by the Cokriging Technique, Jordan Journal of Earth and Environmental Sciences . 9 (1), ISSN 1995-6681, p. 67 - 74

Andreae, M. O. and Gelencsér, A.,(2006), Black carbon or brown carbon? The nature of light-absorbing carbonaceous aerosols, Atmos. Chem. Phys., 6, 3131–3148, https: // doi. org/ 10.5194/ acp-6-3131-2006.

Bergstrom, R. W., Pilewskie, P., Russell, P. B., Redemann, J., Bond, T. C., Quinn, P. K., and Sierau, B., (2007), Spectral absorption properties of atmospheric aerosols, Atmos. Chem. Phys., 7, 5937–5943 https://doi.org/10.5194/acp-7-5937-2007.

Blanco-Donado E.P., Schneider I.L., Artaxo P., Lozano-Osorio J., Portz L., Oliveira M.L.S., (2022), Source identification and global implications of black carbon, Geoscience Frontiers, 13 (1) , art. no. 101149

Bond, T. C., Doherty, S. J., Fahey, D. W., Forster, P. M., Berntsen, T., DeAngelo, B. J., Flanner, M. G., Ghan, S., Kärcher, B., Koch, D., Kinne, S., Kondo, Y., Quinn, P. K., Sarofim, M. C., Schultz, M. G., Schulz, M., Venkataraman, C., Zhang, H., Zhang, S., Bellouin, N., Guttikunda, S. K., Hopke, P. K., Jacobson, M. Z., Kaiser, J. W., Klimont, Z., Lohmann, U., Schwarz, J. P., Shindell, D., Storelvmo, T., Warren, S. G., and Zender, C. S., (2013), 715 Bounding the role of black carbon in the climate system: A scientific assessment, J. Geophys. Res., 118, 5380–5552, https://doi.org/10.1002/jgrd.50171.

Drinovec, L., Gregorič, A., Zotter, P., Wolf, R., Bruns, E. A., Prévôt, A. S. H., Petit, J. E., Favez, O., Sciare, J., Arnold, I. J., (2017), The filter-loading effect by ambient aerosols in filter absorption photometers depends on the coating of the sampled particles. Atmos. Meas. Tech. 10, 1043–1059, doi: 10.5194/amt-10-1043-2017.

Drinovec, L., Močnik, G., Zotter, P., Prévôt, A., Ruckstuhl, C., Coz, E., Rupakheti, M., Sciare, J., Müller, T., and Wiedensohler, A., (2015), "The" dual-spot" Aethalometer: an improved measurement of aerosol black carbon with real-time loading compensation", Atmos. Meas. Tech., 8, 1965–1979, https://doi.org/10.5194/amt-8-1965-2015.

Fialho, P., Hansen, A. D. A., and Honrath, R. E., (2005), Absorption coefficients by aerosols in remote areas: a new approach to decouple dust and black carbon absorption coefficients using seven wavelength Aethalometer data, J. Aerosol Sci., 36, 267–282.

Glaser and Bruno, (2007), "Prehistorically modified soils of central Amazonia: a model for sustainable agriculture in the twenty-first Century", Philosophical Transactions of the Royal Society B: Biological Sciences. 362 (1478): 187–196.

Hamasha, K. M. and W. P., Arnott, (2009), "Photoacoustic measurements of black carbon light absorption coefficients in Irbid city, Jordan", Environ. Monit. Assess, Doi 10.1007 / s10661-009-1017-3

Hamasha, K. M., M. S. Almomani , M. Abu-Allaban and W. P. Arnott, (2010), Study of Black Carbon Levels in City Centers and Industrial Centers in Jordan, Jordan Journal of Physics, Vol. 3, No. 1, pp 1-8

Hamasha, K., (2021), The Increasing Trend of Black Carbon and Organic Carbon in Jordan during the Period of 2007 to 2018, Nature Environment and Pollution Technology Vol 20 , No. 3, pp. 955 – 972, doi.org/10.46488/NEPT.2021.v20i03.004

Hamasha, K., (2023), Measurement of Black Carbon Absorption Coefficients Using an Aethalometer and Their Association with Visibility, Nature Environment and Pollution Technology ,Vol 22, No. 2, pp 741 – 753, doi.org/ 10.46488 / NEPT.2023. v22i02.017

Healy, R.M., Wang, J.M., Sofowote, U., Su, Y., Debosz, J., Noble, M., Munoz, A., Jeong, C. H., Hilker, N., Evans, G. J., (2019), Black carbon in the Lower Fraser Valley, British Columbia: Impact of 2017 wildfires on local air quality and aerosol optical properties. Atmos. Environ. 2019, 217, 116976, doi:10.1016 / j.atmosenv.2019.116976.

Janssen, N. A. H., Gerlofs-Nijland, M. E., Lanki, T., Salonen, R. O., Cassee, F., Hoek, G., Fischer, P., Brunekreef, B., Krzyzanowski, M., (2012), "Health effects of black carbon", The WHO European Centre for Environment and Health, Bonn, Germany, World Health Organisation Regional Office for Europe, Copenhagen, Denmark.

Lack, D. A., Bahreini, R., Langridge, J. M., Gilman, J. B., and Middlebrook, A. M., (2013), Brown carbon absorption linked to organic mass tracers in biomass burning particles. Atmos. Chem. Phys., 13, 2415–2422, doi:10.5194/acp-13-2415-2013.

Lu, Z., Streets, D. G., Winijkul, E., Yan, F., Chen, Y., Bond, T. C., Feng, Y., Dubey, M. K., Liu, S., Pinto, J. P., and Carmichael G. R., (2015), Light Absorption Properties and Radiative Effects of Primary Organic Aerosol Emissions. Environ. Sci. Technol., 49, 4868–4877, doi:10.1021/acs.est.5b00211.

Ran, L., Z.Z. Deng, P.C. Wang, X. A. Xia, (2016), Black carbon and wavelength-dependent aerosol absorption in North China Plain based on two year aethalometermeasurement, Atmospheric Environment, Vol. 142, pp. 132-144, ISSN 1352-2310, doi.org/10.1016/j

Saleh, R., Robinson, E. S., Tkacik, D. S., Ahern, A. T., Liu, S., Aiken, A. C., Sullivan, R. C., Presto, A. A., Dubey, M. K., Yokelson, R. J., Donahue, N. M. and Robinson, A. L., (2014), Brownness of organics in aerosols from biomass burning linked to their black carbon content. Natural Geoscience, 7, 647–650,

doi:10.1038/NGEO2220.

Sandradewi, J., Prévôt, A. S. H., Szidat, S., Perron, N., Alfarra, M. R., Lanz, V. A., Weingartner, E., and Baltensperger, U., (2008a), Using aerosol light absorption measurements for the quantitative determination of wood burning and traffic emission contributions to particulate matter, Environ. Sci. Technol., 42, 3316–3323, doi:10.1021/es702253m.

Sandradewi, J., Prévôt, A. S. H., Weingartner, E., Schmidhauser, R., Gysel, M., and altensperger, U., (2008b), A study of wood burning and traffic aerosols in an Alpine valley using a multi-wavelength aethalometer, Atmos. Environ., 42, 101–112.

Virkkula, A., Mäkelä, T., Hillamo, R., Yli-Tuomi, T., Hirsikko, A., Hämeri, K., and Koponen, I. K., (2007), A simple procedure for correcting loading effects of Aethalometer data, J. Air Waste Manage.,57, 1214–1222, doi:10.3155/1047-3289.57.10.1214.

Wang, L., Bao, S., Liu, X., Wang, F., Zhang, J., Dang, P., Wang, F., Li, B., Lin, Y., (2021), Low-dose exposure to black carbon significantly increase lung injury of cadmium by promoting cellular apoptosis, Ecotoxicology and Environmental Safety , ttps://doi.org/10.1016/j. ecoenv. 2021. 112703, 2021

Wang, J., Huang, L. Wang, C. Chen, D. Yang, M. Jin, C. Bai, Y. Song, Urban particulate matter triggers lung inflammation via the ROS-MAPK-NF-kappaB signaling pathway, J. Thorac. Dis., 9 (11) (2017), pp. 4398-4412, 2017

Weingartner, E., Saathoff, H., Schnaiter, M., Streit, N., Bitnar, B., and Baltensperger, U., (2003), “Absorption of light by soot particles: determination of the absorption coefficient by means of aethalometers”, J. Aerosol Sci. 34, 1445-1463

JJEES

JJEES (2024) 15 (2): 94-106
ISSN 1995-6681

Jordan Journal of Earth and Environmental Sciences

Geochemical Evaluation of a Geothermal Region for the Trace Elements Related to the Subsurface Mineralization Using Machine Learning Methods

Farzad Moradpouri[1*], Hamid Sabeti[2]

[1] Department of Mining Engineering, Faculty of Engineering, Lorestan University, Khoramabad, Iran
[2] Department of Mining Engineering, Faculty of Engineering, Birjand University of Technology), Birjand, Iran

Received August 20, 2023; Accepted December 20, 2023

Abstract

The aim of this paper is to identify the promising geochemical anomalies in the geothermal area of Mianeh in northwestern Iran. This was carried out using 840 stream sediment samples, which were analyzed by ICP-MS for 42 elements for Multivariate Geochemical Analysis (MGA). Due to the high migration and mobility power of the Arsenic element, it was selected as the main geothermal pathfinder. Thus (As) element was determined as a labeled variable, and the other important elements and their relationships with (As) can be identified through MGA. Some of these related elements can then be proposed for future exploration. Firstly, for the implementation of MGA, a Probability Plot Modeling (PPM) on the (As) concentration values was carried out to separate background and anomaly subpopulations and extract threshold values for each subpopulation. Secondly, based on the PPM results for the (As) variable, the Discriminant Function Method (DFM), using their functions of code 0, 1, and 2, was implemented to distinguish different variables belonging to each of those subpopulations (background, mixture, and anomaly). Also, Principal Component Analysis (PCA) and Clustering Analysis (CA) were carried out which lead to almost similar results to the DFM. Finally, the elements of Au, Mo, W, Cu, Be, K, and Rb were recognized as the most important elements related to the (As) element. Finally, ArcGIS mapping shows a geothermal region from the NW to NE of the study area for plans and detailed exploration.

Keywords: *Geothermal pathfinders, Stream sediments, Mineralization, Multivariate analysis, GIS mapping.*

1. Introduction

Geothermal energy is a source of clean energy that can provide reliable base-load power generation, or it can be used as a pathfinder for mineral resources in depth in countries and regions where this resource is available (Barbier, 2002; Lund et al., 2003). The potential for the generation of geothermal energy is found in active seismic areas or with volcanic activity worldwide (Grunsky et al., 2009; Mwangi, 2013). Even some of the geothermal resources are ubiquitous in populated areas and easily accessible; many others are found in the depths of the ocean, in mountainous regions, and under glaciers or cubicles (Bloomfield, 2003; Grunsky et al., 2009; Rybach, 2010).

In the crust, the temperature gradient is typically 30 °C per kilometer, but it can be as high as 150 °C per kilometer in a hot geothermal area. The geothermal resources have been developed in several steps, starting with the exploration of the surface, followed by exploratory drilling to discover and confirm the resource availability (Rowley, 1982). In some countries with many hot springs and surface thermal evidence, it might be a sign of geothermal resources (Openshaw, 1983; Zhu et al., 1989; Ghadimi et al. 2012; Seyedrahimi-Niaraq et al., 2019).

The presence of hot springs, geysers, and fumaroles along with hydrothermal alterations are superficial signs of geothermal activity that may indicate the existence of economical geothermal resources in a region (Lund et al., 2003; Grunsky et al., 2009). According to conducted studies in Iran, many geothermal promising regions in NW of Iran indicate the existence of economic geothermal resources. Using this surface evidence, geological information and geochemical analysis and interpretation can achieve a conceptual model of geothermal resources (Yousefi et al., 2010; Najafi and Ghobadian, 2011; Ma et al., 2016).

Geochemical prospecting plays an important role in the exploration of geothermal resources. In recent years, several researchers used machine learning in geochemical explorations (He, et al., 2022). Pan et al., (2023) carried out geological mapping via a convolutional neural network based on remote sensing and geochemical survey. Zhang et al., (2021) used integration of machine learning algorithms to estimate resources in gold deposits. They also used machine learning-based prediction of trace element concentrations in prospectivity mapping (Zhang et al., 2021a; Zhang et al., 2021b).Geochemical stream sediments can reflect various geochemical characteristics related to the probable subsurface ore bodies better than samples such as soil and groundwater (Anderson, 2006; Ranasinghe et al., 2009; Chandrajit et al., 2001; Gransky et al., 2009; Zuo et al., 2009). In geochemical prospecting, it is not always possible to solve a problem by studying only one element, and it is common

* Corresponding author e-mail: moradpouri.fa@lu.ac.ir

for a set of variables to interact and associate. In this case, it is necessary to study several elements or even the study of contents associated with other variables representative of geological or environmental phenomena (Spadoni et al., 2005; Ranasinghe et al., 2009; Moradpouri et al., 2023). On the other hand, the main problem in the analysis and interpretation of geochemical data (especially stream sediments) is the variety and large size of the data matrix. This problem can be solved using multivariate data analysis that can convert large volumes of the data into simple and visual geochemical information (Peh and Halamić 2010; Gransky et al., 2009; Zuo, 2011; Li et al., 2012; Moradpouri and Ghavami-Riabi, 2020; Tobore, et al., 2023).

In this way, multivariate methods have been an important tool for many years for analyzing a large amount of data so that one can work with many variables simultaneously since it is the set of variables that models a geochemical landscape, not just one in isolation (Anderson, 2006; Chandrajit et al., 2001; Gransky et al., 2009; Al-Momani, et al., 2020; Moradpouri and Hayati, 2021). As the various variables interact to form the final observed picture, some of these interactions and associations sometimes appear clearly in multivariate studies. It is important to mention that the obtained results in the applications of multivariate variables must be compared with the geological information available in the study area for interpretation (Davis, 2002; Dillon and Goldstein, 1984; Moradpouri et al., 2017). For each result of a multivariate application, an association with a geological, metallogenetic, or geochemical process in the area should be sought. Thus, when representing such a result on a map, the behavior of a process that operated in the region can be seen, which can be of great value in understanding its evolution, especially in the case of representing mineralization, hydrothermal alteration, or others (Halfpenny and Mazzucchelli, 1999; Helvoort et al., 2005; Peh and Halamić, 2010; Grunsky et al., 2014, Moradpouri and Ghavami-Riabi, 2020; Moradpouri and Hayati, 2021).

Several researchers used the elements Hg and (As) as indicators for exploring geothermal resources (Matlick and Buseck, 1975; Openshaw, 1983; Shiikawa, 1983; Qian, 2009; Jimoh et al., 2023). The other elements of Sb, Bi, B, and some anions and cations are the key elements in the exploration of geothermal resources (Bingqiu et al., 1988; Zuo et al., 2009; Qian, 2009). Risdianto et al. (2010) presented that the intersections of faults might create permeability in depth and influence the flow of geothermal fluids from reservoirs. Mwangi (2013) used conservative constituents for tracing the origin and flow of geothermal fluids, stable isotopes along with B and Cl as the most important elements. He also used rock-forming constituents of SiO_2, Na, K, Ca, Mg, CO_2, and H_2 to predict subsurface temperatures and potential production problems such as deposition and corrosion (Mwangi, 2013).This paper aims to analyze the stream sediment data of the Mianeh geothermal region in NW of Iran for geothermal pathfinders and new insight into probable subsurface mineralization. The data included 840 stream sediment samples, which were analyzed by ICP-MS methods for 42 geochemical elements. According to the hot spring in the region and field study, the element of (As) was identified as the starting geothermal pathfinder to carry out the Multivariate Geochemical Analysis (MGA).

1.1. Arsenic (As) as Pathfinder

In the early period of geochemical exploration, arsenic (As) and antimony (Sb) were commonly used as so-called pathfinder elements for Au (Boyle, 1979). The name is given because of the common association of gold mineralisation with rocks enriched in arsenopyrite (FeAsS) and/or stibnite (Sb2S3), and because As and Sb were easier to determine analytically due to their higher abundances (Steenfelt, 1996).

Several researchers suggested the use of the identified elements expressly using the strongly correlated elements such as As and Zn to detect hidden anomalies in the complex environment (Dzigbodi-Adjimah, 1993; Kesse, 1985; Arhin et al., 2015).

Yaisamut et al., (2023), presented the interpretation of intricate spatial dispersion patterns and concentration levels of deposit pathfinder elements, specifically arsenic (As), copper (Cu), and zinc (Zn), using a comprehensive array of stream sediment geochemistry data.

2. Geological setting

The Iranian crust is divided into several main and sub-zones based on magmatic, metamorphic, sedimentary, and tectonic occurrences. Mianeh region is located in the NW of Iran (Figure 1). This region has undergone many changes, so that the effects can be monitored from the Precambrian (Mianeh metamorphic unit) to the recent (Sabalan and Sahand volcanism). When looking at the geological map of the Mianeh in Figure 1, it is observed that Tertiary sediments, volcanic rocks, and intrusive masses cover most of it. Most outcrops of the Mianeh region are almost composed of volcanic and sedimentary rocks associated with the Cenozoic by which Eocene and Oligocene volcanic rocks cover the largest area in the region. These rocks often have a combination of rhyolite, ignimbrite, rhyodacite, and trachyte, and the results of the chemical analysis indicate the alkaline nature of this volcanism (Aghanabati, 2004). During the Eocene, the Mianeh region witnessed a lot of volcanic activity, which is often in the form of lava flows with andesitic, basaltic, and andesitic trachea with various combinations of tuff layers. The lowest part of the Eocene volcanic rocks is in the form of pyroclastic deposits, gray acidic tuffs, and acidic lavas followed by andesitic lavas and sandy tuffs (Aghanabati, 2004). A large volume of Eocene volcanic rocks in the form of mega-porphyry andesite is found in the Bozgoosh mountain range. The transition from Eocene to Oligocene volcanism is in the form of ignimbrite, rhyolite, trachyte, and shear tuff rocks that are located on Eocene-related units. Miocene lithology in the regions includes conglomerate, siltstone, sandstone, basalt, andesite, tuff, marl, hornblende, siltstone marls, sandstone conglomerates, shales, and pyroclastic rocks. Miocene deposits are exposed in the southern areas around Mianeh. In addition, Quaternary deposits include old terraces, new terraces, paved limestones, and salt plains that are exposed in the areas around Mianeh (Aghanabati, 2004). The location of the city's border, samples location, Maman hot spring, streams, and river location can also be seen in Figure 1.

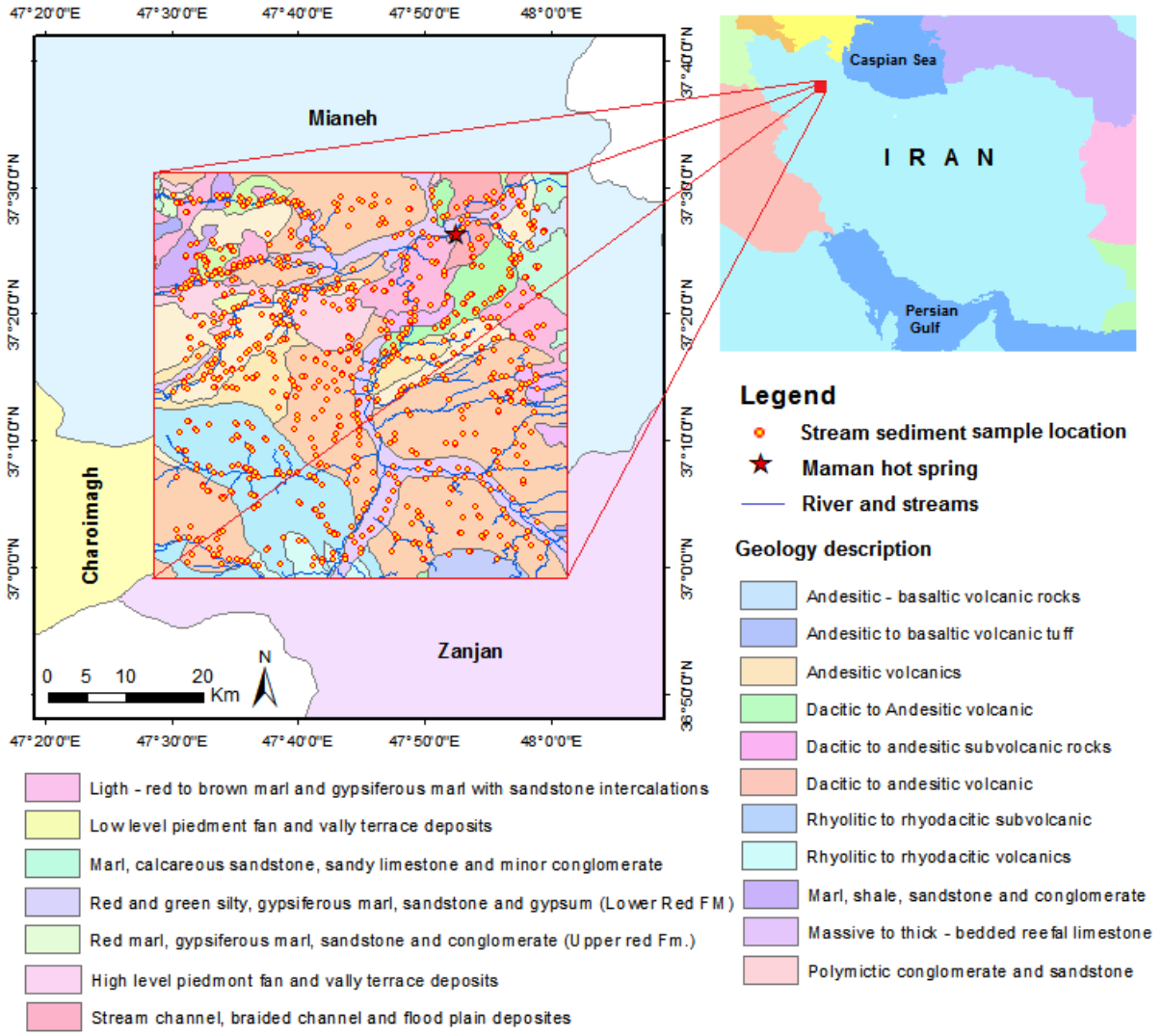

Figure 1. Geological setting and location map of the study area, stream sediment samples, hot springs, rivers, and streams

Rivers, streams, and hot springs: The main rivers in the study area are shown in Figure 2a. Qezel Owzan is one of the longest rivers in Iran. On its track, Zanjanrood and Abharrood Rivers join it, and before the city of Mianeh, the Qaranqo, Shahrchai, and Aidoqmosh Rivers, which flow from west to east join it, and it finally flows into the Caspian Sea (Figure 2a). In addition to the mentioned rivers and due to the topography, the study area includes many streams that are shown in Figure 2b.

The other important phenomena in Eastern Azarbaijan province are hot springs. Some of which are located around Mianeh city. The hot springs of Maman, Sabz, Ivorq, and Gudarq are among the most prominent ones. Sulfur, arsenic, salt, copper, and iron ions are among the most important combinations in these hot waters. Maman hot springs, at a distance of 100 meters from each other, are located in the region of Maman village in the central part of Miyaneh city and the northeast of the study area (Figure 2b). These springs also have therapeutic characteristics of the sulfur type. The water of Maman hot spring is naturally yellow which indicates the presence of sulfur, which can also be seen in the color of the rocks inside and around the hot springs. In addition, many other hot and cold springs in the surrounding regions can be used in geochemical studies to find trace elements. Furthermore, Figure 2b shows a satellite image of the study area including the location map of the stream sediment samples, Maman hot spring, river, and stream sediments which help to interpret the results of the geochemical multivariate analysis.

Figure 2. Location map: (a) rivers (b) streams and stream sediment samples

3. Material and Methods

With the above variety of information (topography, geology, rivers, hot springs), the geochemical analysis and interpretation of stream sediments for probable subsurface mineralization could be a multifaceted work, but the results considerably help us determine the promising areas for future plans and detailed exploration. Therefore, the geochemical sampling of 840 stream sediment samples employed the use of a mattock or shovel to reach appropriate samples from the available river and streams in the study area. Due to the location and nature of the streams, sampling spacing was different. All samples were analyzed for major and trace elements cocentrations by inductively coupled plasma mass spectrometry (ICP-MS) for 42 elments, following a 95°C Aqua Regia digestion. Analytical uncertainties vary from 0.03% to 0.1% for major elements and from 0.1% to 0.55% for trace elements.

3.1. Multivariate Geochemical Analysis (MGA)

A large number of techniques are available that address problems in space with multidimensional approaches to one, two, or more than two populations. Multivariate data are almost all based on the matrix of element concentration. Among the most used methods in geochemistry, principal component analysis, clustering analysis, factor analysis, and discriminant analysis can be mentioned.

Basic statistics:

First, the univariate statistical analysis of the dataset, including maximum, minimum, mean, and standard deviation was carried out for a primary consideration of abnormal variations so that some of the variables show meaningful values (Table 1). Among those elements and based on the reasons that were mentioned, the arsenic (As) element was identified as the geothermal pathfinder in the study area to carry out the Multivariate Geochemical Analysis (MGA) that clarifies which of these elements have more relationships with the As as a pathfinder and which could be a sign of subsurface mineralization. The mean value of (As) in the study area is 20.07 (ppm), and its maximum value is 174.1 (ppm) which may be a meaningful sign of subsurface geothermal activities. In addition, the analysis of histograms, Q-Q and P-P plots, was carried out for the (As) data which indicates a reasonable continuity and lognormal nature in the dataset (Figure 3). Therefore, it was considered for existing sub-populations, thresholds, and background and anomaly separation using PPM.

Table 1. Basic statistics of the stream sediments dataset in the study area (N = 840)

Variable	Min.	Max.	Mean	Std. deviation	Variable	Min.	Max.	Mean	Std. deviation
As	1.460	174.1	20.069	12.942	Mo	0.010	15.61	1.490	1.338
Au	1.000	88	2.338	4.18	Na	1376	73830	13422.8	6550.1
Ag	0.000	2	0.367	0.164	Nb	4.87	69.67	16.435	5.709
Al	23210	103300	64196.7	13703.5	Ni	2.68	74.27	28.366	11.3
Ba	129.6	2516	675.068	208.582	P	20.14	4321	993.05	758.576
Be	0.64	5.82	1.700	0.594	Pb	9.61	172.3	32.307	13.915
Bi	0.01	12.87	1.501	1.255	Rb	12.49	266.9	69.074	30.482
Ca	11240	283200	78684.4	27033.9	S	10	246100	12055.0	27337.8
Cd	0.1	6.48	0.341	0.268	Sb	0.14	342	2.451	11.79
Ce	10.94	111	51.739	12.436	Sc	4.23	25.450	11.781	3.25
Co	4.53	57.83	15.712	5.636	Sn	1.8	7.6	3.204	0.676
Cr	3.61	227.4	63.184	26.408	Sr	117.8	6124	629.82	584.64
Cs	1.0	27.55	5.889	2.535	Te	0.08	1.0	0.156	0.086
Cu	9.090	203.5	34.70	20.98	Th	3.84	83	14.892	5.887
Fe	17480	335750	53608.2	20787.5	Ti	1363	35455	5409.1	2383.8
Hg	0.05	0.6	0.089	0.026	Tl	0.4	2.35	0.918	0.235
K	3434	50800	19424.5	6558.1	U	0.94	17.23	4.437	1.554
La	7.51	75	27.344	7.637	V	41.96	1147	152.98	84.706
Li	11.33	185.8	28.842	12.291	W	0.27	54.3	1.754	2.227
Mg	96.41	32810	9951.3	4237.1	Zn	24.64	334.1	75.95	29.441
Mn	246.7	4431	903.246	283.6	Zr	75.7	911.2	315.02	121.75

Probability Plot Modeling (PPM):

An important issue in the interpretation of various geochemical data with the prospecting perspective is the determination of threshold values that separate the ranges of values defined as representing background and anomalous values. Thus, the probability plot modeling on (As) element as the most important element related to geothermal activities was carried out to de-convolute the subpopulations, which separate the background from the anomalous values. The results of (As) probability diagram modeling are shown in Figure 4. The horizontal axis is the cumulative percent and the vertical axis is the logarithm of concentration values for specific groups of data as open circles (Figure 4a). It should be added that the least-squares method was used to fit the best model to the data. The continuous curve that passes through the groups of data (open circles) is the fitting model that presents the recombination of the sub-populations represented by the sloping straight lines. It is obvious that

three sub-populations can be recognized in the data (Figure 4b). The final step is the improvement of the previous fitting model, which is shown in Figure 4c with the final threshold values. The result of the probability plot modeling, including the details for each subpopulation and the threshold values, is presented in Table 2.

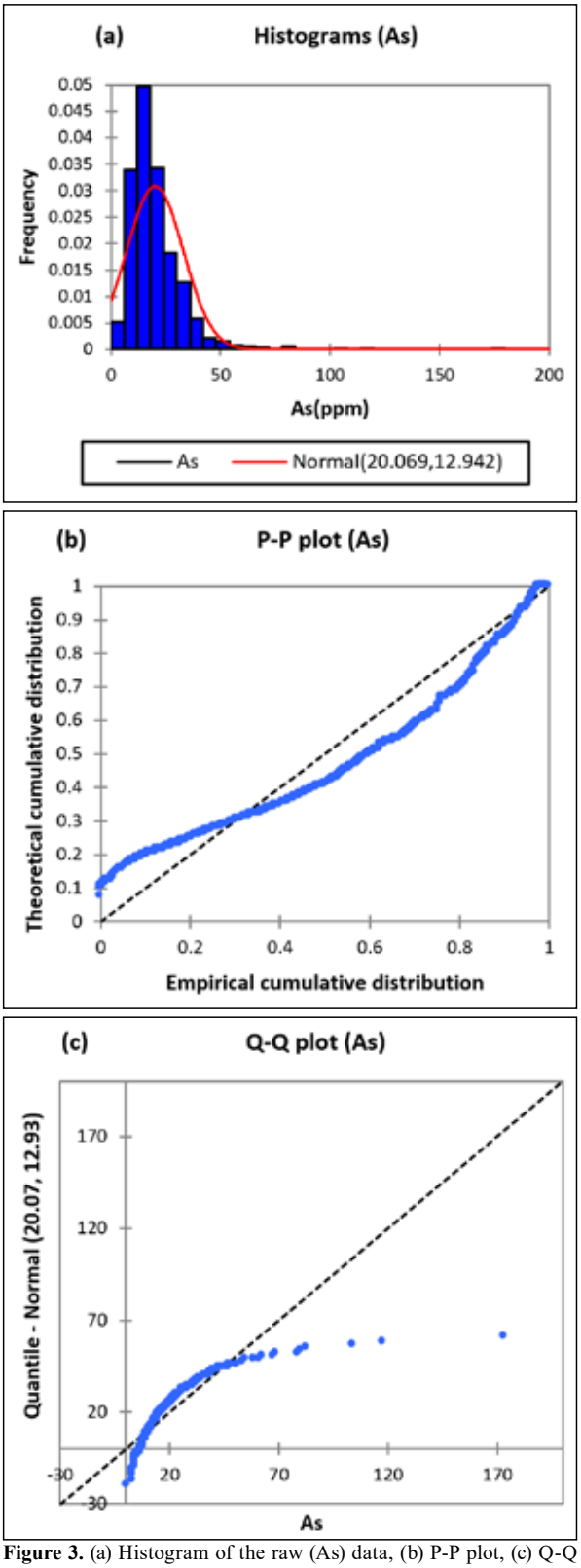

Figure 3. (a) Histogram of the raw (As) data, (b) P-P plot, (c) Q-Q plot.

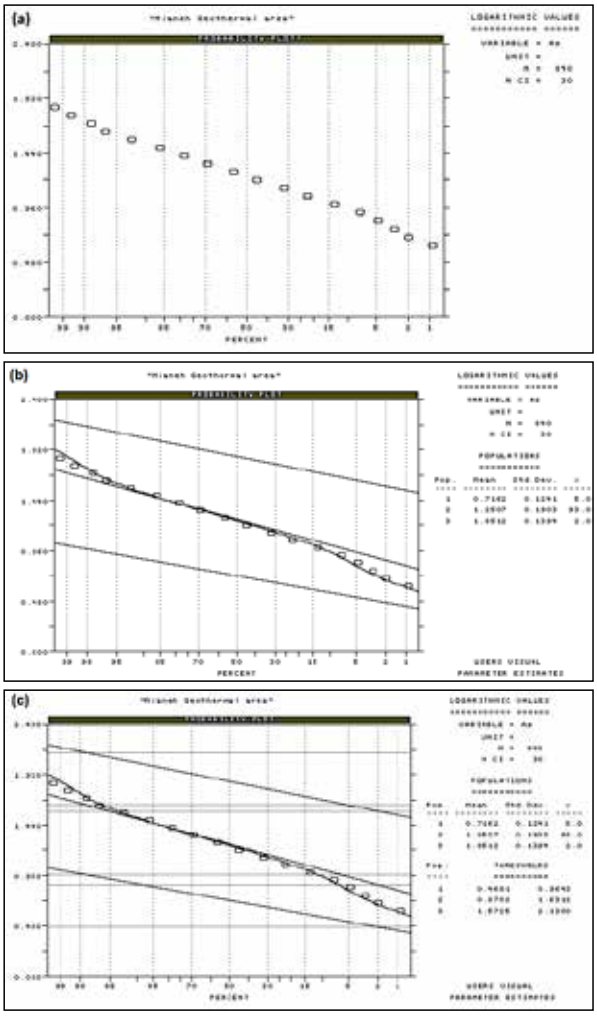

Figure 4. The results of the probability plot modeling. (a) Probability plot of the logarithmic (As) values; (b) First three subpopulation estimates. (c) Results for the revision of the first estimate by three optimization steps to minimize the deviation between data (circles) and model (the fitted curve).

Table 2. Mean, percentage, and threshold values after deconvolution for the three recognized (As) subpopulations

Variable=As	Unit=ppm	N=840	Population	Thresholds
Population	Mean	Percentage	1	2.94-9.21
1	5.20	5.0	2	7.42-42.78
2	17.81	93.0	3	37.37-134.9
3	70.99	2.0	Transform=Logarithmic	
Populations=3 Missing observation=0				

According to the results of probability diagram modeling (in Figure 4 and Table 2), samples with (As) concentration less than 9.21 ppm were identified as background subpopulation, The concentrations values between 9.21 to 42.78 ppm were identified as mixtures of background and anomaly. Finally, samples with concentrations above 42.78 ppm were defined as the anomaly subpopulation. Therefore, the location map of (As) distribution for these three subpopulations is shown in Figure 5. As can be seen, most of the representing anomalous samples are located in the north part of the study area especially along with Qaranqo River and in Maman hot spring. This was somehow expected and showed a promising sign, but it needs to be interpreted considering the

whole geological and geochemical evidence after the proper analysis in the later sections. Thus, first a multivariate discriminant analysis was carried out to determine the most related elements to the (As) content using the PPM threshold results of Table 2. In addition, the multivariate geochemical analysis of PCA and clustering analysis were carried out for comparison.

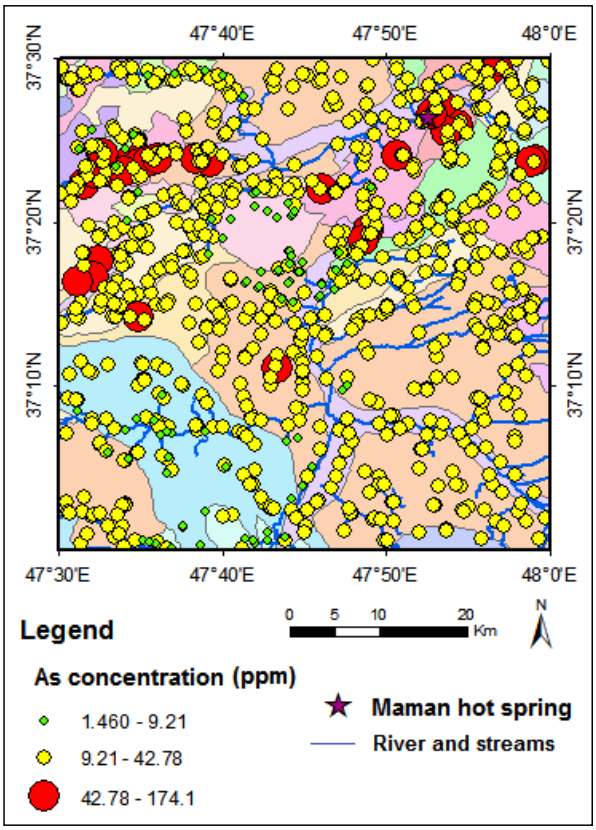

Figure 5. Arsenic (As) content distribution based on the probability plot modeling threshold values

Discriminant Function Method (DFM): DFM is one multivariate statistical data analysis that is used for the evaluation of the dependence of one sample on one of two (or more) known populations. The discriminant function is defined based on known features of those populations. In order to define the discriminant function, a linear combination of all variables is used to create a normally distributed univariate variable. This function is calculated in the direction of the highest discrimination of the populations (Peh and Halamić, 2010).

The coefficients of this linear combination is defined as follows.

$$[a]^T = \left(\left[\bar{X}_1 - \bar{X}_2\right]\right)^T [S]^{-1} \quad (1)$$

where $[a]^T$ is the coefficients matrix, $\bar{X}_1$ and $\bar{X}_2$ are estimated mean vectors of two populations, is the reversed covariance matrix of two populations.

Now, the discriminant function is calculated using the following equation.

$$DF = \left(\left[\bar{X}_1 - \bar{X}_2\right]\right)^T [S]^{-1} [X] \quad (2)$$

where $[X]$ is the vector of the newly observed sample, there is a function that defines the separation boundary of two populations called the critical function as in the following equation.

$$[D]_0 = \left(\left[\bar{X}_1 - \bar{X}_2\right]\right)^T [S]^{-1} \left(\frac{\left[\bar{X}_1 + \bar{X}_2\right]}{2}\right) \quad (3)$$

This function is a vector, which starts from the end of $[\bar{X}_1]$ and finally reaches to the separation boundary of two populations. If then $DF < D_0$ the sample is assigned to population 1 and if then $DF > D_0$ samples are assigned to population 2.

Arsenic mentioned above, (As) element was chosen as the dependent variable versus the other independent variables (elements). Thus, the linear discriminant functions of Code 0, Code 1, and Code 2, were defined based on the probability plot modeling of the (As) variable in Table 2. The analysis was implemented using the dataset of 42 variables related to the 840 stream sediment samples. Based on the threshold values, the (As) values of the background population with a concentration of less than 9.21 ppm were defined as Code 0, the values between 9.21 and 42.78 ppm were defined as Code 1 (a mixture of the background and anomaly), and finally, the values above 42.78 ppm were defined as Code 2 (anomaly). This forms the basis of the linear function that was used for the DFM, which evaluates the relationship between variables through the three defined codes and the two discriminant functions.

Based on the DFM, two functions can be defined which are shown in Table 3 with its parameters. Function 1 describes 90.3% of the variability with a correlation of 84% with the data. In addition, function 2 describes 9.7% of the variability with a 45% correlation. Contrary to the correlation coefficient, the lower the Wilks' Lambda coefficient, the better the discriminant function. The larger the Chi-square coefficient, the better the function could justify the variability.

Table 3. Calculated discriminant functions and validation parameters

Function	Eigenvalue	Variance percentage	Cumulative percentage	Correlation	Wilks' Lambda	Chi-square	df	Sig.
1	2.349	90.3	90.3	0.84	0.239	1169.663	84	0.000
2	0.251	9.7	100.0	0.45	0.799	182.887	41	0.000

In the next step, the samples were classified according to two discriminant functions. In Figure 6, each classified sample was coded and a different color was assigned for visualization purposes. This figure shows that considerable discrimination has occurred between the data related to sub-populations. Then, the variables were discriminated based on the two defined functions between the three disputed sub-populations that are shown in Figure 7, which shows one reality that describes separation boundary based on (As) variable coded values and their functions. In addition, the

other variables' locations in Figure 7, are outputs of the DFM. As can be seen in Figure 7, As, Au, Mo, W, Th, K, Rb, Be, Ce, Fe, and Nb were located in the anomalous part as tracing elements for (As) element and probable mineralization (Code 2). Cs, Co, Ce, Hg, P, Ni, Li, and Zr were located in the mixture part (Code 1), and the rest were located in the background part (Code 0).

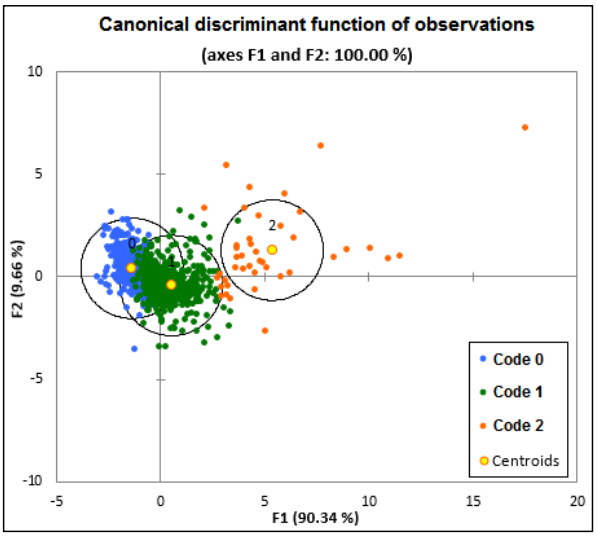

Figure 6. Classified samples based on discriminant function 1 and 2

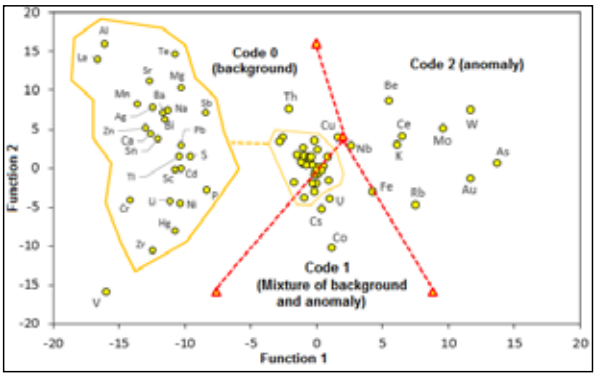

Figure 7. Standardized canonical discriminant function coefficient based on the three discriminant functions.

To evaluate the results of DFM, based on p-p modeling and according to the discriminate functions, 93.2%, 86.6%, and 81% of the samples were correctly classified as code 0, Code 1, and Code 2 respectively when three different groups memberships were used (Table 4). In addition, as can be seen in Table 3, this method could validate that 92% of code 0, 83.5% of code 1, and 71.4% of code 2 were classified properly.

Principal Component Analysis (PCA):

PCA is a way of identifying patterns in data and expressing them in a way that highlights their similarities and differences, with the advantage that once these patterns are identified, we can reduce the number of dimensions without much loss of information. We choose components and form a vector feature, and the eigenvector with the highest corresponding eigenvalue is the principal component of the dataset. Minor components can be ignored, with some loss of information, but if the eigenvalues are small, the loss is not very significant.

Table 4. Classification and validation of the DFM results.

	Code		Predicted Group Membership			Total
			0	1	2	
Original	Count	0	314	23	0	337
		1	61	399	1	461
		2	0	8	34	42
	%	0	93.2	6.8	.0	100.0
		1	13.2	86.6	.2	100.0
		2	.0	19.0	81.0	100.0
Cross-validated	Count	0	310	27	0	337
		1	71	385	5	461
		2	0	12	30	42
	%	0	92.0	8.0	.0	100.0
		1	15.4	83.5	1.1	100.0
		2	.0	28.6	71.4	100.0

In Geology, PCA can represent active geological processes, present lithological changes or events causing mineralization. The dimensionality of the problem is also reduced. In addition, it allows the identification of the variables that have very high or low contributions to the variability of the study area. An identification that allows suggesting the elimination of these variables in future stages of study. In addition, a very common objective in geochemical programs is the classification of observations that make up a given sample (rocks, stream sediments, soils, or water). This classification is often based on the measured concentration. It is very useful in cases where large amounts of observations are available and in cases where there is little prior knowledge of the meaning of the genesis of the constituents.

In the current research, PCA was processed with the raw data of 840 stream sediment samples for 42 variables to explore the elemental associations. There are several techniques for decision-making on the retention of main components, the most accepted and recommended being the one that proposes the retention of main components whose total variability percentages are considered significant, that is, they explain an important proportion of the total variations present. In the original data set. It is evident that, at this point, the participation of the technician who applies PCA is decisive; the non-use of components from a certain level (from the fourth main component, or the fifth, for example) does not, however, cause any problems on the ones used, nor does it affect their interpretation under any circumstances. It can only leave processes represented by the unused components, which have no influence, as stated above, on the interpreted components (and their associated processes). Table 5 presents the variability of each component and its respective eigenvalue for the first component among the whole component. Actually, the first two components explain 45.63% of the variability of the data, while the first seven components explain 66.9%. As can be seen, in Figure 8, after the fifth component, one can see a mild trend in variability, which means that we can ignore the components with the low contribution in introducing the variability in the data.

Table 5. Main components and their respective eigenvalue and variability

	F1	F2	F3	F4	F5	F6	F7
Eigenvalue	13.502	5.664	2.734	1.916	1.544	1.417	1.321
Variability (%)	32.147	13.486	6.510	4.562	3.676	3.374	3.146
Cumulative %	32.147	45.633	52.143	56.705	60.381	63.756	66.901

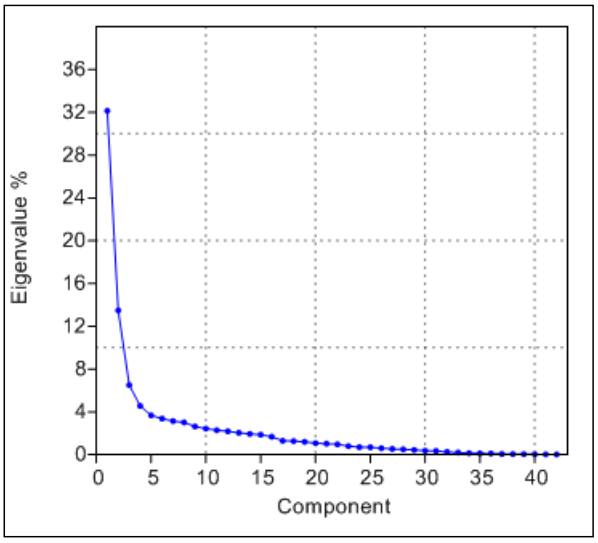

Figure 8. Contribution of variables to the main components

Figure 9a-c shows the correlation between the first three components with the coordinates of the variables. The coordinates are based on correlations and are plotted according to components F1, F2, and F3. As can be seen in Figure 9a, the first group from the loadings of F1 consists of Na, Ni, Tl, Mn, Ba, Nb, Li, Th, Zn, Sn, Cr, Co, Fe, Cs, Ti, V, Hg, Bi, and Tl, and the second group from the loadings of F_2 consists of K, Be, Rb, Au, As, Mo, Sb, P, Cu, W, Ag, Zr, Al, Ce, La, Cd, Pb, and Sc. In addition, in each group, one can interpret the relationship and correlation between elements. For example, the most related elements to (As) as the main pathfinder element in Mianeh geothermal area in F1/F2 map are Au, Sb, Mo, Cu, W, K, Rb, Be, Zr, and P. It is both because of the low angle between their straight lines and rather due to their close distance of (As), Au, Mo, and Sb from the center, we need to obsessively interpret this association and we should look at the relationship between these variables on the other pair of components map. On the other hand, the correlation between the ratio of elements shows that for example for the elements (As), Au, and Cu, there is no correlation between the As/Au ratio with As/Cu, but the short length of the line that connects both Au and Cu to (As) shows the lower variance between each pair of these elements. As an example of a high correlation between two pairs of ratios, the high correlation for the ratio of As/Au to As/Sb can be mentioned. Figure 10a-c shows the coordinates of the samples according to components F1, F2, and F3. Figures 9 and 10 determine the importance degree of each factor based on the location of the different variables and samples' location.

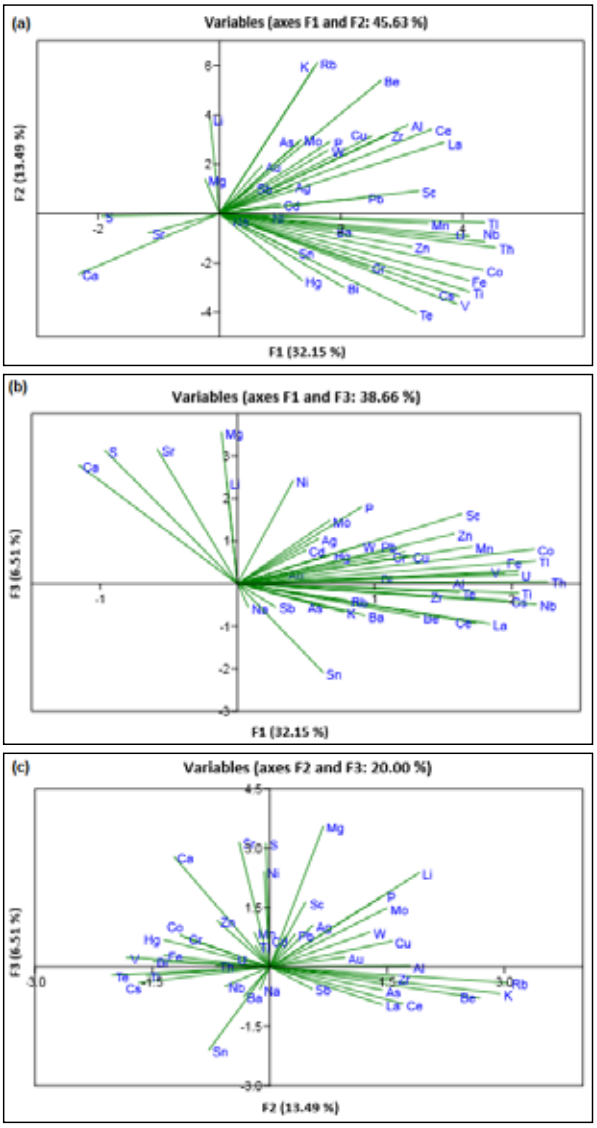

Figure 9. Coordinates of the variables when the axes represent the variable loading values in F1 (principal component 1), and F2 (principal component 2) and F3 (principal component 3). (a) in the F1 and F2 domain, (b) in the F1 and F3 domain, (c) in the F2 and F3 domain.

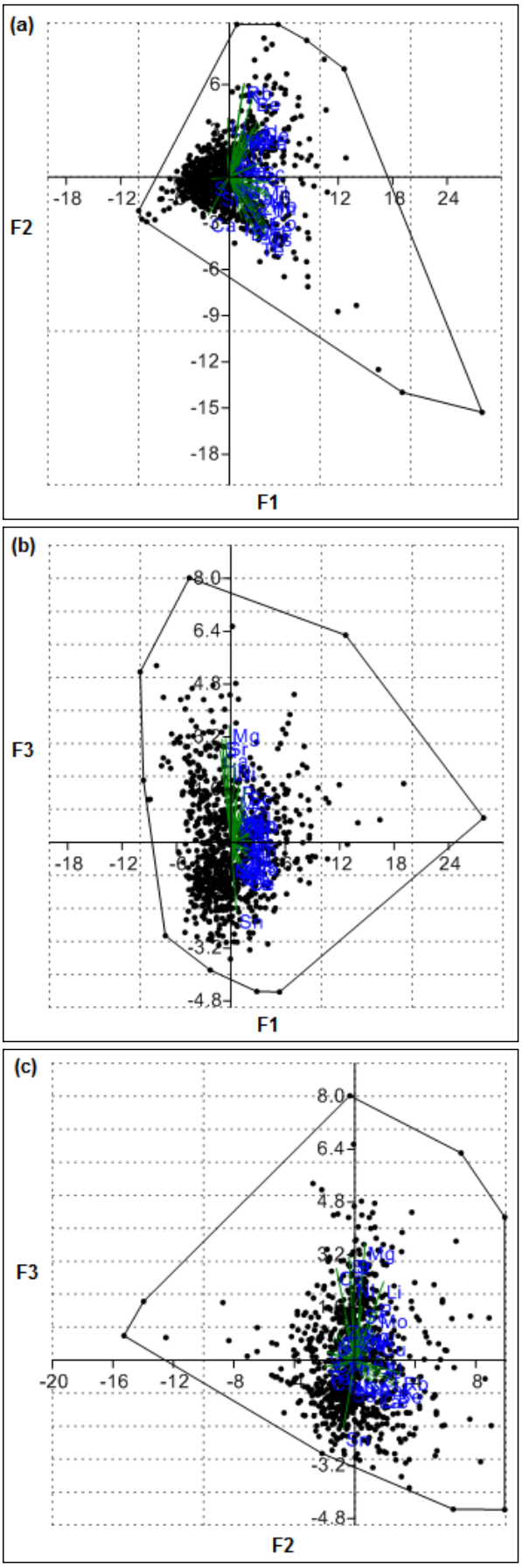

Figure 10. Sample coordinates in PCA. (a) F1 and F2, (b) F1 and F3, (c) F2 and F3.

Clustering Analysis (CA): The application of the CA is very useful as an exploratory tool for data, that is, it can indicate associations /groups that are not previously suspected, and it can often simply reflect some obvious lithological associations. It aims to classify objects (in the case of geochemistry, field samples, or analyzed variables) for similarities and/or dissimilarities, and the groups generated must have high internal homogeneity and high external heterogeneity. Cluster analysis is applied to objects (Q technique), whose variables can be also examined for similarities and groupings (R technique). The different methods for cluster analysis can be framed into four general types: partition methods, methods with arbitrary origin, methods by mutual similarity, and methods by hierarchical groupings.

The method used in this work was hierarchical groupings (the most used in geochemistry) in R mode. The grouping was processed using the method of Ward´s agglomeration (minimum variance), grouped by correlation coefficient. The same raw data used for DFM and PCA was also applied for the CA. In order to evaluate similarities between elements, cluster dendrograms, showing hierarchical variable clustering, are presented in Figure 11. It shows the lines linked according to levels of similarity that group pairs of the variables. The higher the correlation, the shorter the connection distance between variables. From right to left, the first cluster of orange color is largely made up of elements associated with the (As) element as the geothermal pathfinder. This cluster includes the elements Au, As, Mo, W, Be, K, Rb, Zr, Ce, La, Ag, Al, Sc, Cu, and P, so that some of them have a closer connection distance, and some are far away. However, the results are rather similar to the DFM and PCA results, and one can classify a pack of those elements as the geothermal pathfinders of the occurred mineralization based on the geological setting.

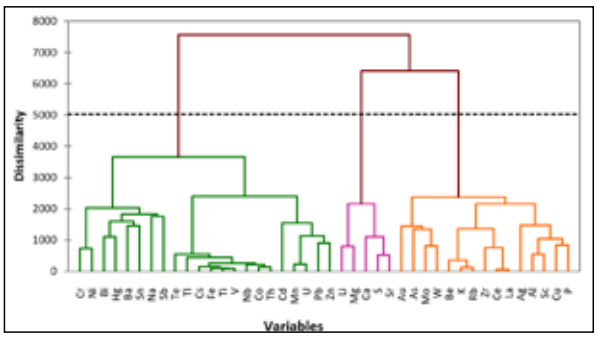

Figure 11. The dendrogram in R mode shows the hierarchical variable clustering by correlation.

GIS mapping: As discussed in the previous sections, the results obtained from DFM, PCA, and CA indicated that a number of elements were identified as related to the arsenic geothermal pathfinder (e.g. Au, Mo, W, Sb, K, Rb, P, Cs, Be, La, Cu, Zr, Ag, and Al). Among these associations, the elements (variables) of Au, Mo, W, Cu, Be, K, and Rb were recognized as the most important related elements to (As) based on the multivariate geochemical analysis (MGA). Some of them can be interpreted as elements related to mineralization (e.g. Au, Mo, Cu). As, Au, Mo, and Cu reinforce the probability of porphyry deposit. It should be

added that (As) has a direct relationship with gold deposits. Among the important geothermal pathfinders such as Sb, Hg, and Bi, only the Sb element showed the relationships with (As) element only in PCA which cannot be seen in DFM or CA. Sb is an element of the nitrogen family (N, As, Sb, P, Bi) and has rather similar chemical properties to Arsenic (As). On the other hand, the elements of K, Rb, and Be are present in alkali feldspar minerals of the volcanic rocks. Distribution maps of the above-related elements were prepared in ArcGIS10.5 software using the kriging method and are shown in Figure 12. In this Figure, the anomalous area of the arsenic geothermal pathfinder and the main related elements of mineralization can be seen. These areas are proposed as promising regions for the later exploration steps.

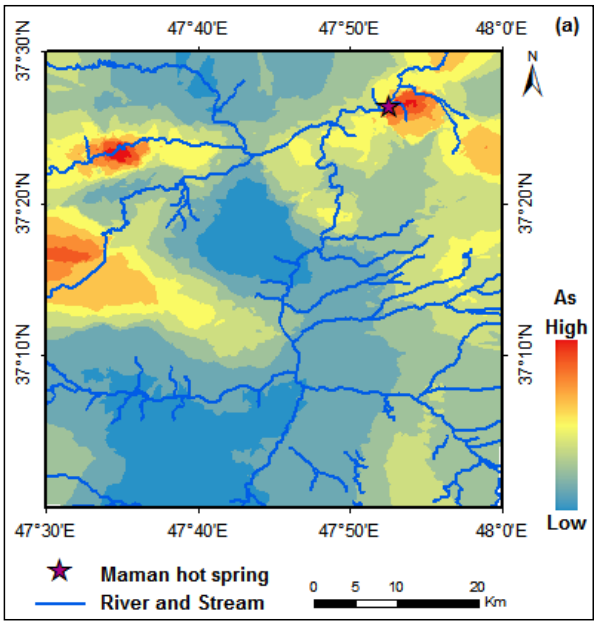

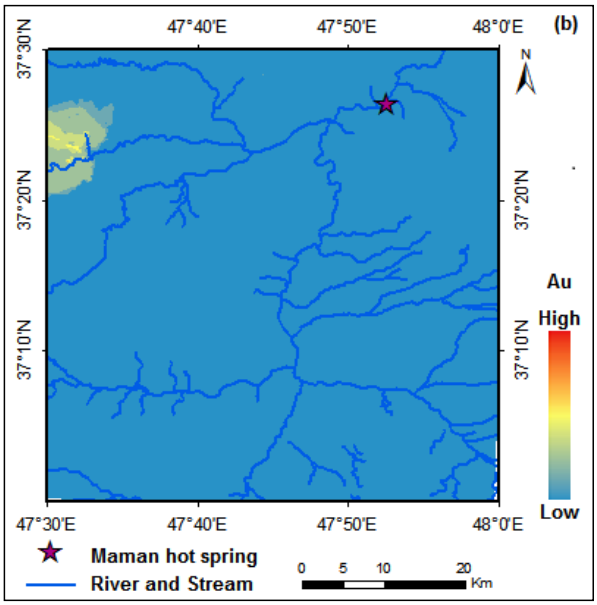

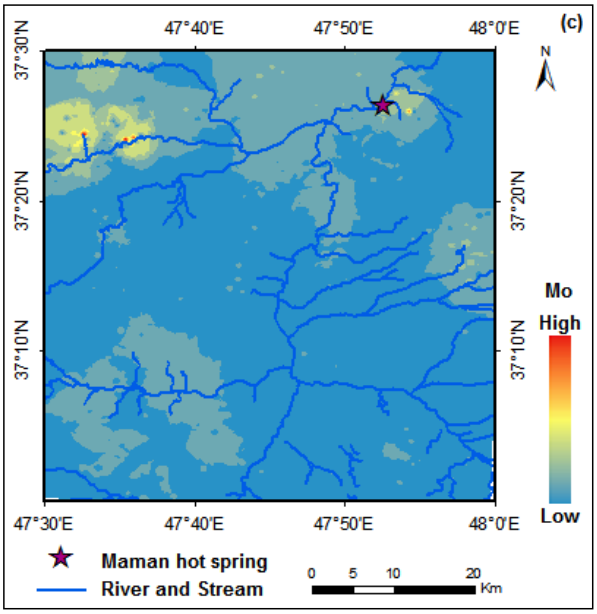

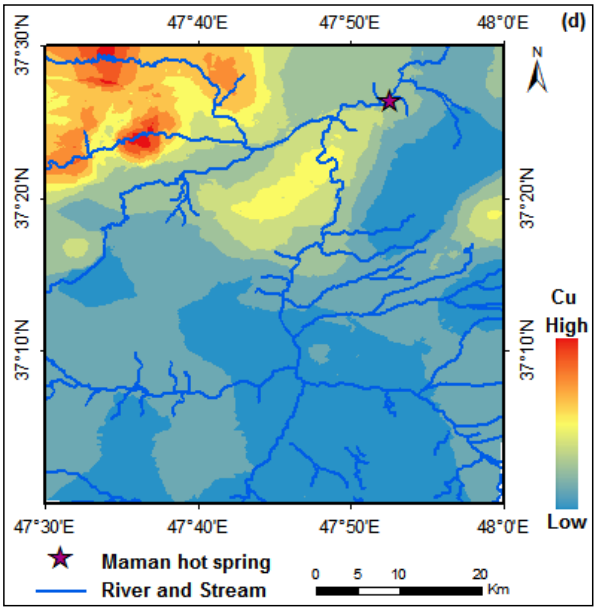

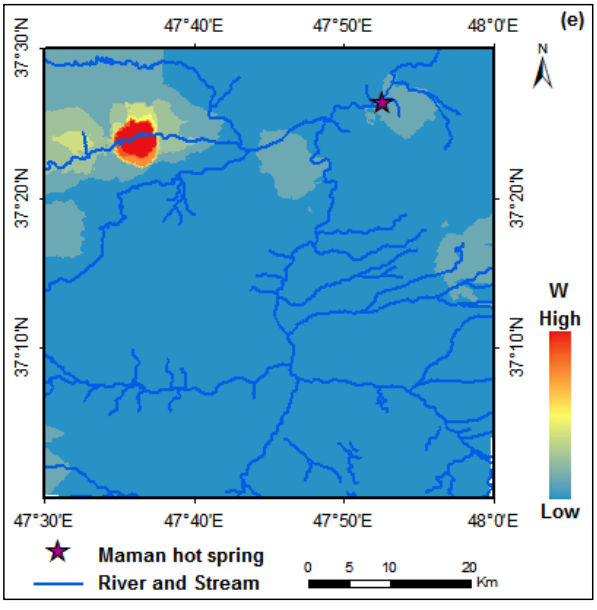

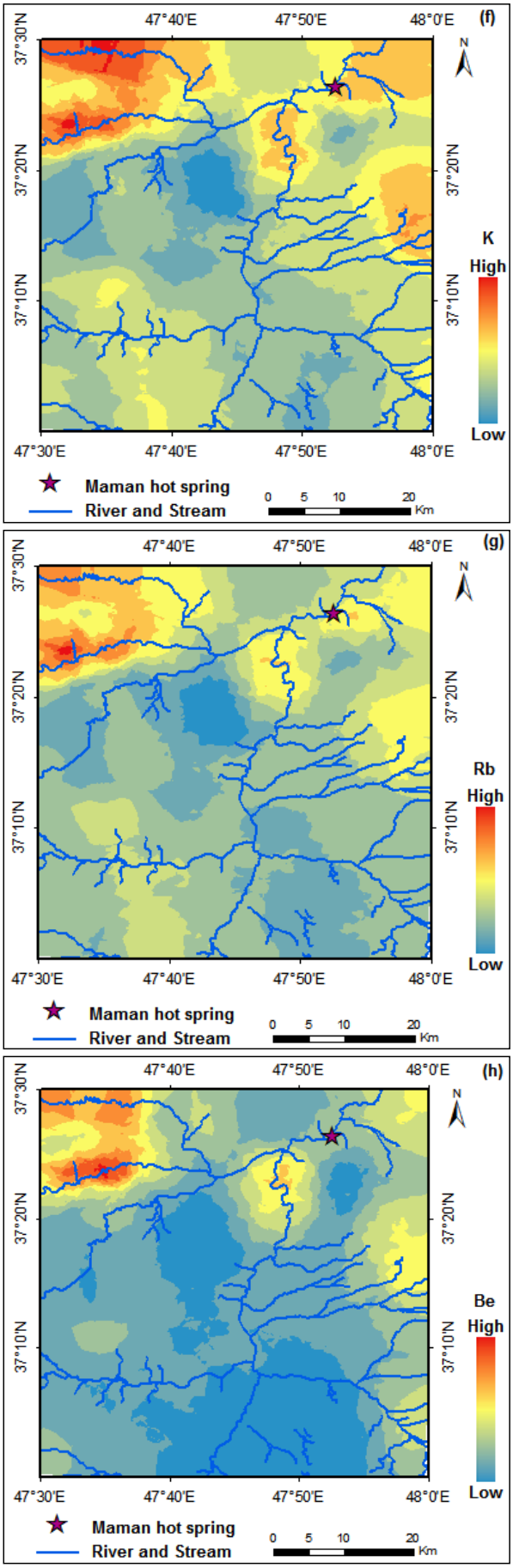

Figure 12. Anomalous area of the geothermal pathfinders and the probable variables of mineralization. (a) As, (b) Au, (c) Mo, (d) Cu, (e) W, (f) K, (g) Rb, (h) Be

4. Conclusion

The results of the present study can be divided into several parts. (a) Due to the selection of arsenic element (As) as a suitable geothermal pathfinder in the study area, the MGA proved that none of the other geothermal pathfinders such as Sb, Hg, and Bi showed a significant relationship with (As) pathfinder. Thus, arsenic plays a key role in the prospecting of geothermal resources in the study area using stream sediments. (b) What can be deduced from the integrated map of the promising areas, geological and MGA indicates that there is an active geothermal region in the northwest of the study area that includes the rivers of Shahrchai, Qaranqu, and Aidoqmosh that originate from volcanic areas of the Sabalan and Sahand mountains and continue to Maman hot spring in the Northeast. These paths often consist of volcanic rocks. (c) Different MGA methods of the present stream sediment data revealed several multi-element associations describing the existence of subsurface probable mineralization in the NW to NE of the study area for plans. Among these associations, the elements of Au, Mo, W, Cu, Be, K, and Rb were recognized as the most important related elements to the (As) variable. The elements of Au, Mo, and Cu can be interpreted as the elements related to the mineralization, which may indicate the probability of a porphyry deposit. The elements of K, Rb, and Be are present in alkali feldspar minerals of the volcanic rocks.

Conflict of Interests

The authors declare that there are no conflicts of interest regarding the publication of this paper.

References

Aghanabati, A. (2004). Geology of Iran, Geological Survey and Mineral Exploration of Iran. 586 p. (In Farsi).

Al-Momani, T., Alqudah, M., Ezz-Aldien, M. (2020). Dwairi Mineralogical and Geochemical Characterization of Jarash Kaolinitic Clay, Northern Jordan. Jordan Journal of Earth and Environmental Sciences 11 (4): 272-281.

Anderson, T. (2003). An Introduction to Multivariate Statistical Analysis. 3rd Ed., John Wiley and Sons. 742 pp., ISBN 0-471-36091-0.

Arhin, E., Boadi, S., Esoah, M.C. (2015). Identifying pathfinder elements from termite mound samples for gold exploration in regolith complex terrain of the Lawra belt, NW Ghana. Journal of African Earth Science 109: 143–153.

Barbier, Enrico. (2002). Geothermal energy technology and current status: an overview. Renewable and Sustainable Energy Reviews 6: 3-65.

Bingqiu, Z., Lixin, Z., Changyi, S., Hui, Y. and Gongyuan, W. (1988). Application of geochemical methods in the search for geothermal fields. Journal of Geochemical Exploration 33: 171-183.

Bloomfield, K.K., Moore J.N., Neilson R.N. (2003). Geothermal energy reduces greenhouse gases. Geoth Res Counc Bull 32(2): 77-79.

Davis, J.C. (2002). Statistics and Data Analysis in Geology. 3rd Ed., John Wiley and Sons, NY. ISBN: 978-0-471-17275-8.

Dillon, W.R. and Goldstein, M. (1984). Multivariate Analysis: Methods and Applications", John Wiley and Sons, New York, 587 S. ISBN 0-471-08317-8. https://doi.org/10.1002/bimj.4710290617.

Dzigbodi-Adjimah, K. (1993). Geology and geochemical patterns of the Birimian gold deposits, West African Journal of Geochemical Exploration 47 (1–3): 305-320.

Ghadimi, F., Mirzaei, M., Ghomi, M., Mina, M. (2012). Hydrochemical properties of the thermal waters of Mahalat Abgarm, Iran. Geothermal Resources Council Transactions 36: 1355– 1358.

Grunsky, E.C., Drew, L.J., Sutphin, D.M. (2009). Process recognition in multi-element soil and stream-sediment geochemical data. Applied Geochemistry 24:1602–1616. https://doi.org/10.1016/j.apgeochem.2009.04.024.

Grunsky, E.C., Mueller, U.A., Corrigan, D. (2014). A study of the lake sediment geochemistry of the Melville Peninsula using multivariate methods: applications for predictive geological mapping. Journal of Geochemical Exploration 141: 15–41. https://doi.org/10.1016/j.gexplo.2013.07.013.

Halfpenny, R. and Mazzucchelli, R.H. (1999). Regional multi-element drainage geochemistry in the Himalayan Mountains, northern Pakistan. Journal of Geochemical Exploration 67(1-3): 223-233.

He, Y., Zhou. Y ., Wen, T., Zhang, S., Huang, F., Zou, X., Ma, X., Zhu, Y. (2023). A review of machine learning in geochemistry and cosmochemistry: Method improvements and applications, Applied Geochemistry 140: 105273. https://doi.org/10.1016/j.apgeochem.2022.105273.

Helvoort, P.J., Filzmoser, P., Gaans, P.F.M. (2005). Sequential Factor Analysis as a new approach to multivariate analysis of heterogeneous geochemical datasets: an application to a bulk chemical characterization of fluvial deposits (Rhine–Meuse delta, The Netherlands), Applied Geochemistry 20: 2233–2251. https://doi.org/10.1016/j.apgeochem.2005.08.009.

Kesse, G.O. (1985). The Mineral and Rock Resources of Ghana. A.A. Balkema, Rotterdam, Netherlands, 610 pp. ISBN: 9061915899.

Li, J., Wang, Y., Xie X., Su, C. (2012). Hierarchical cluster analysis of arsenic and fluoride enrichments in groundwater from the Datong basin, Northern China, Journal of Geochemical Exploration 118(1–3): 77–89.

Lund, J.W, Sanner, B., Rybach, L., Curtis, R., Hellstrom, G. (2003). Ground-source heat pumps- A world overview. Renew Energ World 6(l4): 218–227.

Ma, T., Li, C., Lu, Z. (2016). Geographical environment determinism for discovery of mineral deposits. Journal of Geochemical Exploration 168: 163–168. DOI:10.1016/j.gexplo.2016.07.001.

Matlick, J.S. and Buseck, P.R. (1975). Exploration for geothermal areas using mercury: a new geochemical technique. In: Second United Nations Symposium on the Development and use of Geothermal Resources, Volume I: 785-792.

Moradpouri, F. and Ghavami-Riabi, R. (2020). A multivariate geochemical investigation of borehole samples for gold deposits exploration, Geochemistry International 58(1): 40-48. https://doi.org/10.1134/S0016702920010103.

Moradpouri, F. and Hayati, M. (2021). A copper porphyry promising zones mapping based on the exploratory data, multivariate geochemical analysis and GIS integration, Applied Geochemistry 132: 105051, https://doi.org/10.1016/j.apgeochem.2021.105051.

Moradpouri, F., Ahmadi, S.M.H.,Ghaedrahmati, R., and Barani, K. 2023. Determination of the erosion level of a porphyry copper deposit using soil geochemistry. Journal of the Southern African Institute of Mining and Metallurgy 123(2): 103–112.

Moradpouri, F., Moradzadeh, A., Cruz Pestana, R., Soleimani Monfared, M. (2017). An improvement in RTM method to image steep dip petroleum bearing structures and its superiority to other methods. Journal of Mining and Environment 8(4): 573-578.

Mwangi, M.M. (2013). Application of geochemical methods in geothermal exploration in Kenya. Procedia Earth and Planetary Science 7: 602-606. DOI: 10.1016/j.proeps.2013.03.220.

Najafi, G. and Ghobadian, B. (2011). Geothermal resources in Iran: the sustainable future. Renewable and Sustainable Energy Reviews 15(8): 3946-3951. DOI: 10.1016/j.rser.2011.07.032.

Openshaw, R.E. (1983). Hg and As soil geochemistry of the Meager Creak Geothermal Area. Journal of Geochemical Exploration 19: 339-344. https://doi.org/10.1016/0375-6742(83)90027-4.

Pan, T., Zuo, R. and Wang, Z. (2023). Geological Mapping via Convolutional Neural Network Based on Remote Sensing and Geochemical Survey Data in Vegetation Coverage Areas, IEEE Journal of Selected Topics in Applied Earth Observations and Remote Sensing16: 3485-3494.

Peh, Z., Halamić, J. (2010). Discriminant function model as a tool for classification of stratigraphically undefined radiolarian cherts in ophiolite zones, Journal of Geochemical Exploration 107: 30-38. DOI: 10.1016/j.gexplo.2010.06.003.

Ranasinghe, P.N., Fernando, G.W.A.R, Dissanayake, C.B., Rupasinghe, M.S., Witter, D.L. (2009). Statistical evaluation of stream sediment geochemistry in interpreting the river catchment of high-grade metamorphic terrains, Journal of Geochemical Exploration 103: 97–114. https://doi.org/10.1016/j.gexplo.2009.07.003.

Jimoh, R. O., Olatunji, A.S., Ajadi, J., Afolabi, A.O. (2023). Mineralogy and Geochemistry of Beryl-Bearing Prgmatite Dykes from Gbayo, Southwestern Nigeria. Jordan Journal of Earth and Environmental Sciences 14 (2): 91-102.

Risdianto, D. and Kusnadi, D. (2010). The Application of a Probability Graph in Geothermal Exploration. Proceedings of World Geothermal Congress. Bali, Indonesia, 25–29.

Rowley, J.C. (1982). Worldwide geothermal resources. In: Edwards LM et al (eds) Handbook of geothermal energy. Gulf Publishing, Houston, pp 44–176, Chapter 2. ISBN 0-87201-322-7.

Rybach, L. (2010). The future of geothermal energy and its challenges. In: Proceedings world geothermal congress, Bali, Indonesia, 25–29. April 2010.

Seyedrahimi-Niaraq, M., Ardejani, F.D., Noorollahi, Y., Porkhial, S., Itoi, R. and Nasrabadi, S.J. (2019). A three-dimensional numerical model to simulate Iranian NW Sabalan geothermal system. Geothermics 77: 41-62.

Shiikawa, M. (1983). The role of mercury, arsenic and boron as pathfinder elements in geochemical exploration for geothermal energy, Journal of Geochemical Exploration 19: 337-338. https://doi.org/10.1016/0375-6742(83)90026-2.

Spadoni, M., Voltaggio, M. Cavarretta G. (2005). Recognition of areas of anomalous concentration of potentially hazardous elements by means of a subcatchment-based discriminant analysis of stream sediments, Journal of Geochemical Exploration 87: 83–91. https://doi.org/10.1016/j.gexplo.2005.08.001.

Steenfelt, A. (1996). Distribution of gold, arsenic, and antimony in West and South Greenland: a guide to mineral exploration and environmental management. Bulletin Grønland Geologiske Undersøgelse 172: 55-61.

Tobore, A., Senjobi, B., Oyerinde, G., Bamidele, S. (2023). Geospatial Soil Suitability Assessment for Maize (Zea mays) Production in Derived Savanna of Agricultural Research and Training, OYO STATE, Nigeria. Jordan Journal of Earth and Environmental Sciences. 14 (1): 9-18.

Yaisamut, O., Xie, S., Charusiri, P., Dong, J., Wen, W. (2023).

Prediction of Au-Associated Minerals in Eastern Thailand Based on Stream Sediment Geochemical Data Analysis by S-A Multifractal Model. Minerals 13: 1297. https://doi.org/10.3390/min13101297.

Yousefi H., Noorollahi Y., Ehara S., Itoi R., Yousefi A., Fujimitsu Y., Nishijima J., Sasaki K. (2010). Developing the geothermal resources map of Iran. geothermics 39: 140-151.

Zhang, S.E., Nwaila, G.T., Bourdeau, J.E., Ashwal, L.D. (2021a). Machine learning-based prediction of trace element concentrations using data from the Karoo large igneous province and its application in prospectivity mapping. Artif. Intell. Geosci. 2: 60–75. https://doi.org/10.1016/j.aiig.2021.11.002.

Zhang, S.E., Nwaila, G.T., Tolmay, L.C., Frimmel, H.E., Bourdeau, J.E. (2021b). Integration of machine learning algorithms with gompertz curves and kriging to estimate resources in gold deposits. Nat. Resour. Res. 30: 39–56. https://doi.org/ 10.1007/s11053-020-09750-z.

Zhu, B., Zhu, L., Shi, C., Yu, H. Wang, G. (1989). Application of geochemical methods in the search for geothermal fields. In: Xie Xuejing and S.E. Jenness (Editors), Geochemical Exploration in China. J. Geochem. Explor., 33: 171-183. https://doi.org/10.1016/0375-6742(89)90027-7.

Zuo R. (2011). Identifying geochemical anomalies associated with Cu and Pb–Zn skarn mineralization using principal component analysis and spectrum–area fractal modeling in the Gangdese Belt, Tibet (China, Journal of Geochemical Exploration 111: 13–22. DOI: 10.1016/j.gexplo.2011.06.012.

Zuo, R., Cheng, Q., Agterberg, F.P. and Xia, Q. (2009). Application of singularity mapping technique to identify local anomalies using stream sediment geochemical data, a case study from Gangdese, Tibet, western China. Journal of Geochemical Exploration 101: 225–235. DOI: 10.1016/j.gexplo.2008.08.003.

JJEES

JJEES (2024) 15 (2): 107-114
ISSN 1995-6681

Jordan Journal of Earth and Environmental Sciences

The Mineralogical Composition of Fine Sand for Selected Soils in Suq Al-Shuyoukh City / Southern Iraq

Ali Ramthan[1], Hussein Kh. Chlaib[1*]

[1] University of Sumer, College of Agriculture, Department of Soil Sciences and Water Resources, Thi Qar, Iraq

Received January 4, 2023; Accepted October 7, 2023

Abstract

Suq Al-Shuyoukh is one of the Iraqi alluvial plain areas. Five farms were selected and a total of three samples were taken from each farm at depths of 50, 100, and 150 cm. All samples were subjected to a polarized light microscope to determine the mineral type in fine sand grains and determine the origin and the mechanism of their formation. The results showed two main mineral categories in the fine sand, light, and heavy minerals. The light minerals were Calcite, Quartz, Chert, Gypsum, Anhydrite, and Feldspar, in addition to rock pieces and some fossils. Calcite was dominant. The heavy minerals included the dark minerals (Opaque), Chlorite, Amphibole, Pyroxene,Apidot, Zircon, Muscovite, Garnet, Biotite, Rutile, Tourmaline, in addition to pieces of rocks or fossils, and the dominant mineral was Opaque. Weathering index values for heavy and light minerals ranged between (0.2 - 0.5%) and (4.5 - 9.6%), respectively. The weathering unit index values for light minerals showed an increase in the surface weathering decreased with depth, which indicates the climatic influences mainly. According to the heavy minerals'types and concentration, the proposed source for these minerals is the Arabian Shield due to the volcanic provenance of the parent rocks.

Keywords: *Heavy minerals, Light minerals;,Weathering index, Polarized light microscope, Suq Al-Shuyoukh City.*

1. Introduction

The mineralogical part of the soil consists of particles of different sizes and proportions according to the factors and conditions of soil formation. Because the formation of the grains takes place through the natural fracture and chemical decomposition of large grains as a result of the formation process for the raw materials, it is expected that we will find a difference in the mineralogical and chemical composition of these grains as a result of the difference in their sizes. This will reflect the chemical and physical characteristics of the original substance from which it was formed.

General geological surveys and other investigations of these areas and surrounding lands have been studied by many authors (Al-Shakeri et al., 2017; Al-Janabi et al., 1988; Buday and Jassim, 1987; Shaker, 1986). Most of these studies focused on geological overviews of the study areas, and/or provided descriptions of its provenance, sedimentology, and mineralogy.

Soil consists of three main grain sizes which are sand, silt, and clay. This study focused on the separated sandy part of the studied soil samples, which consists of grains ranging in diameter from 1-0.05 mm. Sand fractions were chosen because their particle properties can be reorganized obviously under polarized microscope more than clay fractions, including shape, size, cleavage, twinning, and color. Sand grains are small pieces of rock (rock fragments) or minerals, which reflect the origin of the parent rock from which these minerals are formed. Sand grains are small pieces of rock (rock fragments) or minerals, which reflect the origin of the parent rock from which these minerals are formed. It is found naturally in different places in the Earth's crust (Dahnoun and Djadouni, 2020). Therefore, from a mineralogical point of view, sand contains primary minerals such as silica, feldspar, and mica , in addition to secondary compounds and minerals that result from chemical weathering processes such as free oxides, especially iron and aluminum oxides. The common minerals in the mineral composition of sand are quartz, feldspar, mica, amphiboles, pyroxene, and other (non-silicate) minerals (Awwad, 1986).

It is also possible to rely on some minerals that are resistant to weathering to study the process of soil development. These minerals are called index minerals. Quartz, zircon, tourmaline, and rutile, which can be found in the clay part of the soil, are the most important of these minerals. The identifying factors of soil components mainly depend on the study of the mineral composition of these soils, which are greatly affected by the processes of weathering and geological erosion, as well as their use as an indicator of soil formation and development through studying the environmental reality of the current and past period (Al-Jubouri, 2014). The separated fine sand has occupied the main importance in this research. It deals with the fine grains of the soil that are enough to determine its optical characteristics.

The aims of this study are

1. studying and determining the physical and optical properties of light and heavy minerals, and
2. determining the probable provenance of the rocks.

* Corresponding author e-mail: hkaldobayany@yahoo.com

2. Materials and Methods

2.1. Study area

The study area is located in Suq Al-Shuyukh District, 30 km southeast of Nasiriyah City, southern Iraq within Iraqi Mesopotamia (Figure 1).The lands are agricultural and mostly covered by sedimentary plains. These lands are part of the flood plain unit branching from the Great Plain unit of the Iraqi sedimentary plain, which is characterized by its low and flat nature. There are no large slopes and their elevations range from (12-16 m) above sea level (Rahel, 2008).

Five sites were selected within the studied area, depending on agricultural practices and the nature of irrigation. Sites (1) and (3) represent soil that have been exploited for 10 years, irrigated from the Euphrates River, while sites (2), (4), and (5) have not been exploited for a period of 15 years for the purpose of comparison.

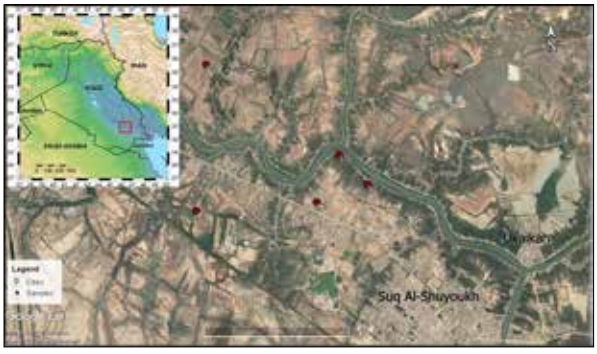

Figure 1. Google maps show the study area, modified from Google Earth

2.2. Soil Sampling

Each site included drill holes by an auger with a depth of 150 cm. Soil samples were obtained for each 50 cm depth for the purpose of conducting mineral analyses. Table 1 shows the coordinates of the five sites with their depths.

Table 1. The locations of the studied soil samples, showing the depth and dry color Munsell code

Sample No.	Depth / cm	Color/ Dry	Coordinates	
			Latitude	Longitude
L1-1	50	10YR6/1	30˚55.519 N	46˚25.568 E
L1-2	100	10YR7/2		
L1-3	150	10YR4/2		
L2-1	50	10YR6/1	30 ˚55.133 N	46˚26.333 E
L2-2	100	10YR7/3		
L2-3	150	10YR5/3		
L3-1	50	10YR5/3	30˚56.138 N	46˚25.931 E
L3-2	100	10YR5/3		
L3-3	150	10YR6/3		
L4-1	50	10YR5/1	30˚55.437 N	46˚23.792 E
L4-2	100	5YR5/3		
L4-3	150	10YR6/3		
L5-1	50	10YR5/3	30˚57.447 N	46˚23.887 E
L5-2	100	10YR6/3		
L5-3	150	10YR7/4		

2.3. Sample Preparation

After the samples were collected from the field, they were dried in the laboratory. It is passed through a sieve with a diameter of 2,000 microns (2 mm), to remove plant residues and unwanted materials. The samples were crushed well—without grinding—by a ceramic mortar in order to preserve the morphological shape of the mineral grains. It was treated with acid, distilled water, and peroxide to remove salts, organic matter, and adhesive materials.

For the purpose of studying the mineral composition through polarizing electron microscopy of fine sand grains separated by sieves, 15 grams were taken from each sample after good mixing (Awwad et al., 2009). Sand, clay, and silt were separated by the dry sifting method through a sieve with a diameter of 62 microns. The fine sand, remaining on the surface of the sieve, was separated and dried by air. Then, they were repeatedly exposed to a current of water for ensuring separating the mineral grains and removing the remaining mud or suspended materials on the surface of the grains, according to the method described by Jackson, (1975).

The remaining sand particles were taken from the previous separation process. The sand particles were divided according to their density into two parts using Bromoform ($CHBr_3$) liquid with a specific weight of 2.80 g. cm^{-3} to separate them into the respective cones. Then, the two parts were dried and placed on glass slides using Arabic glue (Canada balsam) as a preparation medium. After that, the dried parts are covered with thin glass slides. The prepared slides were examined by polarized optical microscope BS-5095TRF model. Based on what was mentioned by Carver (1971), the optical properties of each metal were observed, which were later used in the diagnostic process.

The percentage of the presence of each metal was calculated using the counting method for about 300-350 grains in each slide along straight and parallel lines covering the whole sample. Minerals were diagnosed by the physical properties by polarizing microscope according to Milner (1962) represented by color, form, cleavage, relief and extinction.

3. Results and Discussion

3.1. Light minerals

The results of the process of separating light and heavy minerals from sand particles in the depths of the soils in the study areas showed that light minerals with a specific weight of less than 2.89 form the bulk of the sand particles. These minerals included Quartz, Feldspar, Calcite, Chert, Gypsum, Anhydrite, and rock fragments.

Table 2 shows the percentages of light minerals of the separated sand. Calcite was the dominant mineral in all study sites with a percentage ranging between 42.0 and 45.7%. The results also showed that the vertical distribution of this mineral within the soil depths was not consistent, due to the differences in the geological processes, such as weathering and erosion, as well as the pedogenic processes with increasing depth. The dominance of calcite mineral in the study soil is due to the presence of carbonate-rich formations, such as Dammam, Euphrates, and Nfayil formations, which spread widely in the study area representing the sedimentary rocks (limestone). These sedimentary rocks were subjected

to exposure, weathering, and erosion processes that led to its fragmentation, transfer, and deposition within the soils of the study area (Al-Ankaz, 2012). Figure 2 shows the calcite mineral، representing carbonate rocks fragments under a polarizing microscope.

Quartz is considered to be the most resistant mineral to chemical and mechanical weathering factors. Quartz (SiO_2) is ranked in the second place in terms of dominance. Its percentage ranged between (18.2 - 21.2%). The results also showed that the vertical distribution of quartz through the depth horizons of the studied soil locations was not consistent. The dominance of quartz in the study soils is due to the effect of the nature of the soil origin material, which is originally rich in quartz, the main component of the sand. Also, the quartz is characterized by its high resistance to weathering due to the nature of its ionic chemical bonds and the degree of its hardness (Al-Azami, 2006). Figure 2-b shows the Quartz under the microscope. The source of Quartz comes from the deposits of the Debdiba formation in Nasiriyah, which are formed under semi-humid conditions with relatively short dry periods. These climatic conditions played an important role in the dominance of Quartz and reduced the proportion of Feldspar (Al-Khafaji and Al-Najar, 2010).

In third place came the sedimentary mineral Chert (flint stone) (Figure 2-c). This mineral, consisting mainly of Silica, is considered one of the highly weathering resistant minerals. Its percentage ranged between 13.2and17.5%. It has taken a somewhat vertical distribution in the depths of the studied soil locations.

The reason for the presence of this mineral in high proportions in the soil is the result of its presence in the sandstone layers in the formation of Al-Dibbah, which is exposed in areas close to the study area. Likewise, according to Pettijohn (1957), the presence of limestone pieces is attributed to the mineral maturation of sandstone deposited in the Dibdiba formation, which was subjected to the processes of weathering and erosion.

Table 2. The percentages of light minerals in the fine sand particles for the locations of the study area

Location	Depth/ cm	Quartz	Feldspar	Gypsum and Anhydrite	Calcite	Chert	Rock Fragments	Others	Index Weathering*
	%								
Location 1	50	19.9	2.7	10.7	42.0	17.1	6.6	1.0	7.3
	100	20.1	2.4	9.2	43.9	16.5	6.7	1.2	8.3
	150	19.3	3.0	8.9	43.0	17.5	7.2	1.1	6.4
Location 2	50	18.2	3.7	10.6	42.3	17.4	6.3	1.5	4.9
	100	18.2	3.0	10.8	43.2	16.9	6.9	1.0	6.0
	150	20.9	2.4	9.5	42.7	15.9	7.7	1.4	8.7
Location 3	50	19.3	2.0	8.0	45.7	15.7	7.9	1.4	9.6
	100	18.5	3.0	9.9	42.7	16.2	7.9	1.7	6.1
	150	20.2	3.9	10.7	42.6	13.2	5.9	1.5	5.1
Location 4	50	20.1	4.1	8.4	45.7	14.7	6.4	1.6	4.9
	100	21.2	3.4	6.7	44.5	15.4	7.4	1.4	6.2
	150	20.5	3.9	6.4	43.8	16.8	7.2	1.4	5.2
Location 5	50	20.9	3.3	5.8	44.2	16.9	7.4	1.5	6.3
	100	19.6	4.3	6.8	42.5	17.3	7.8	1.7	4.5
	150	19.5	4.1	6.8	43.4	17.5	7.1	1.6	4.7

* The Quartz/Feldspar ratio was adopted as an indication of the light minerals weathering intensity in the study area (Carver, 1971).

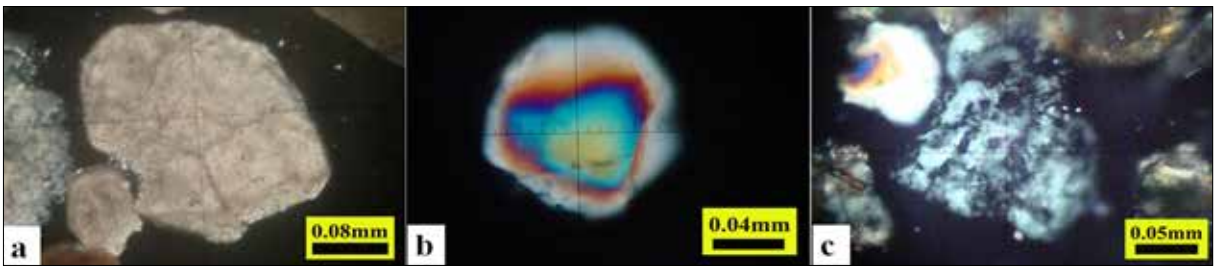

Figure 2. Shows three types of light minerals: a) Calcite (carbonate rock fragment (Limestone), Sample Number L5-2 , b) Quartz, Sample Number L5-2, and c) Chert rock fragment, Sample Number L3-2

Gypsum and Anhydrite came in fourth place. They showed a difference in their distribution pattern with the depth of each location as well as in their percentage which ranged from (5.8 - 10.8%). This vast difference in their percentage is due to the influence of the pedogenic process on these two minerals at different levels, depending on the nature of agricultural practices and the nature of the solubility of both minerals as well as soil materials inherited from the original substance and its mineral composition (Figure 3-a). These two minerals may represent a rearrangement within

the soil body, representing a structural and evolutionary stage for the formation of Gypsum horizons, as stated in the study of Al-Azami, 2006.

As for Feldspar minerals, which came in the fifth rank with few percentages compared to other minerals, the percentages of their presence in the study horizons ranged between (2.0 - 4.3%), and their percentage was close in most of the horizons (Figure 3-b). It is one of the minerals that is greatly affected by different weathering processes, as it is affected by the nature of the soil components, the nature of the origin (parent) material, and the severity of weathering. So, we note that its percentages are greatly reduced in some horizons. The reason of this reduction is due to the ease of chemical weathering and transformation into clay minerals such as Kaolinite and Illite (Tucker, 1985) according to its low presence in the studied samples. This result indicates the mineral's transmission over short distances and the speed of its chemical weathering, and this is due to the presence of Feldspar minerals in the sandy sediments of the formation of Al-Dibbeh in the Nasiriyah region (Al-Khafaji and Al-Najar, 2010). Feldspar is more abundant in metamorphic and igneous rocks than in sedimentary rocks, and its presence in sandstones is generally very beneficial (Pettijohn et al., 1987).

Table 2 also shows the rock fragments' percentages that ranged between (5.9 - 7.9%). They are limestone sedimentary, clay, and silica rock pieces. As for their shapes under the microscope, they were in different shapes from round to angular shape. Most of them were covered with clay materials or iron oxides, and their distribution pattern was heterogeneousone within the horizons of the studied locations (Figure 3-c).

Other materials were found in considerable ratios, most of which consist of fossils that spread widely in the sedimentary plain area, in addition to their large spread in the study area, representing marshes and swamps. The proportions of these fossils ranged from (1.0-1.7%) as shown in Figure 4.

To clarify the weathering condition of light minerals, the Quartz / Feldspar mineral ratio was adopted as an indication of the intensity of weathering of light minerals in the study soils (AlKhalil and Essa, 2020). As shown in Table 2, the weathering index values for light metals ranged between 4.5 and 9.6%. The lowest weathering index appeared within the fifth location at the depth of 100-150 cm. While the highest weathering index appeared within the third location of the surface horizon (depth of 0-50 cm). These values indicate the increase in surface weathering and its decrease with depth.

3.2. Heavy Minerals

Heavy minerals generally include Opaque minerals with a high specific weight because of their iron content. They are sometimes black, such as Magnetite, which spreads in igneous rocks (Kerr, 1959), or brown, as in Hematite, which spreads in metamorphic and sedimentary rocks (Bishop and Hamilton, 1974) or yellowish as in Limonite that is produced from the oxidation of ferrous minerals (Kerr, 1959).

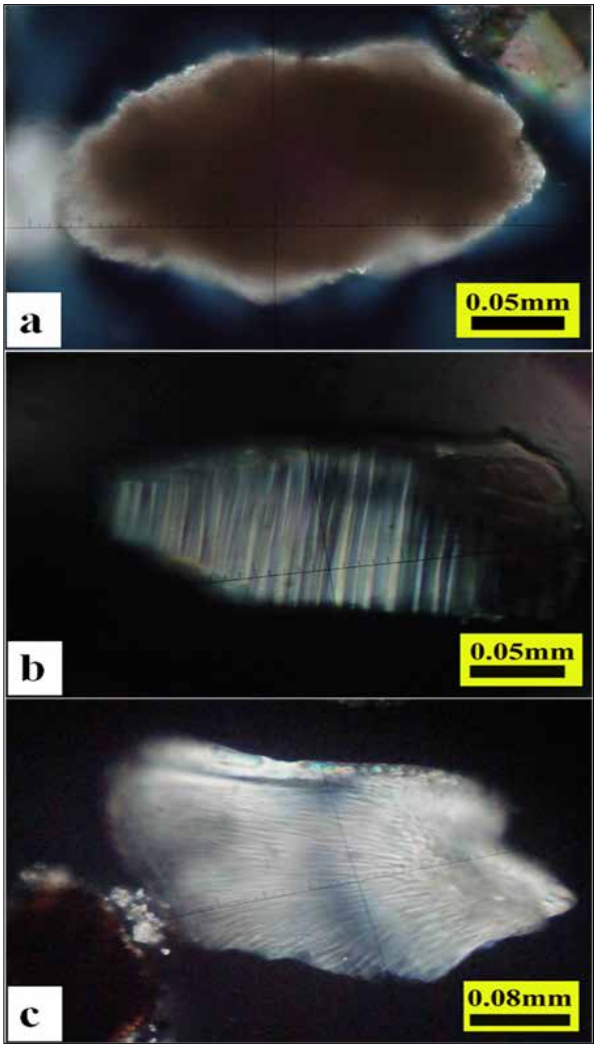

Figure 3. Shows three types of light minerals: a) Secondary Gypsum, Sample Number L3-3, b) Plagioclase Feldspar, Sample Number L2-1, and c) Carbonate Rock Fragment (Shell Fragment) (Aragonite), Sample Number L1-1

Figure 4. Shows a sample of the fossils (shells) that appear in the study area, Sample Number L4-3

Table 3 shows the values of heavy minerals as percentages of their distribution with depth for fine sand grains separated by sieve. It was noted that it contained large numbers of minerals in the following sequence: the dark minerals, Chlorite, Amphibole, Pyroxene, Apidot, Zircon,

Muscovite, Garnet, Biotite, Rutile, and Tourmaline.

Through the values of Table 3, it appears that the dark minerals Opaque Grains represent the largest percentages of heavy minerals in all the depths of the study area, as their percentages ranged (from 46.7 to 50.9%). The reason for the dominance of the Opaque group of minerals over the rest of the minerals is due to the role of the oxide-rich parent material (Figure 5-a). It was shown (Kerr, 1959) that Opaque minerals are found in metamorphic rocks and re-depositioned sedimentary rocks (Al-Jubouri, 2010).

Chlorite is found in metamorphic rocks (Pettijohn, 1975). It comes in second place through its supremacy in the studied locations, where the percentage ranged from (8.9-10.7%). It showed a kind of vertical distribution within the depth of one location, specifically location No. (2), which is graded from 8.9 - 9.2 - 10.0 (Figures 5a-b).

Among the heavy minerals is the presence of Amphibole minerals group represented by Hornblende. It is considered a medium stable mineral and common in igneous and metamorphic rocks (Pettijohn et al., 1972). Its percentage ranged between (6.8 - 7.7%), and it took an irregular pattern and distribution with depth for all study locations, where it increases in the surface horizons and decreases with depth in a location and in the surface horizons. It also shows an increase with depth in other locations. The reason for the difference in its ratio may be attributed to the variation of the original material, the nature of its mineral composition, chronological age, and deposition conditions.

Table 3 also shows the presence of Pyroxene in rates ranging from (6.2-7.4%). In general, the value was linearly homogeneous and convergent for the surface horizons, and heterogeneous vertically. It is considered one of the important mineral groups that make up the Ferromagnetic rocks found in igneous and metamorphic rocks (Murray, 2007). It was shown by (Al-Fatlawi, 2002) that the source of these minerals in Iraqi soils is either intermediate-basic and ultra-basic igneous rocks or acidic rocks.

As shown in Table 3, the presence of Epidote in percentages ranging from (5.2-6.5%). This mineral, as is common among the minerals resistant to weathering, appears in metamorphic rocks. It may be found as an additional mineral in igneous rocks (Figure 5c).

Also, Zircon appeared with a percentage ranging between (3.1 - 5.9%) in all study locations. Its presence didn't indicate any homogeneous distribution. It was present in all locations in different proportions vertically and horizontally, and the source of this mineral is common igneous and metamorphic rocks (Figure 5d).

Muscovite is found in lower percentages ranging between (3.8 - 4.9%) than the previous minerals in all the study locations where it is considered less resistant to weathering. It was noted that Muscovite has a vertical increase with depth in locations (1), (3), and (4). This may be due to the lack of weathering processes with depth, represented by pedogenic processes and climatic conditions.

Garnet is one of the minerals resistant to weathering, but it was found in small percentages in the study locations, which ranged between (3.5 - 5.3%), and perhaps the reason of this scarcity is due to the nature of the origin materials, which contain little of this mineral. Garnet is a common mineral in metamorphic rocks and may be also found in igneous rocks as an additional mineral (Pettijohn, 1975).

Table 3 also shows the Biotite (Figure 6- a) with a value ranging between (3.0 - 4.9%) which showed close values within the surface horizons. As for Rutile, (Figure 6-b), it showed low percentages compared to other minerals, as its percentage ranged between (1.2-2.4%). The reason of the decline is attributed to the source materials, which is the base rock from which these soils came.

Finally, the Table showed the lowest values for all study locations represented by the Tourmaline (Figure 6-c), with values ranging between (1.0 - 1.9%), and the reason for its decline may be attributed to weathering processes or the nature of the original material.

In order to understand the state of weathering within the horizons of the soil for heavy minerals, which have a somewhat higher resistance to weathering than light metals, the ratios of (Zircon + Tourmaline) and that of (Amphibole + Pyroxene) were adopted as an indication of the intensity of heavy minerals weathering in the soils' study (Carver, 1971).

Table 3 shows the weathering index values for heavy minerals. These index values ranged between (0.2 - 0.5%), which are low values compared to light minerals. It was noted that the weathering values for a single location are close, and this explains that these horizons within a single location were subjected to somewhat similar conditions in addition to the similarity of the original material. This is what was observed in locations (4) and (5), as the index values were equal, scoring 0.4% for all horizons of the study locations.

The other locations indicate a rise in the weathering values of the surface horizons or those below them, and this is due to the climatic conditions of heat and rain. As well as the decomposition of plant residues, which encourages microbial activity and thus helps the minerals weather and dissolve into other minerals.

Table 3. The percentages of heavy minerals in the fine sand particles of the study area soils

Locations	Depth/ cm	Opaque	Chlorite	Zircon	Garnet	Pyroxene	Amphibole	Tourmaline	Epidote	Rutile	Biotite	Muscovite	Others	Index* Weathering
	%													
Location 1	50	49.9	9.8	4.5	3.5	6.9	7.0	1.7	5.8	1.7	3.0	4.0	1.8	0.3
	100	48.4	10.7	5.9	3.8	6.8	7.5	1.0	5.2	1.9	3.4	3.8	1.9	0.3
	150	50.9	9.4	4.9	3.9	6.4	7.3	-	6.0	2.0	3.5	3.7	2.0	0.2
Location 2	50	48.6	8.9	3.7	3.7	7.0	7.7	1.4	5.9	2.2	3.8	4.9	2.2	0.3
	100	47.7	9.2	5.1	4.0	7.2	7.5	1.2	6.3	1.8	3.6	4.1	2.3	0.3
	150	49.0	10.0	5.3	4.1	6.8	6.9	1.5	5.5	1.2	3.5	4.2	2.0	0.4
Location 3	50	48.6	8.9	4.8	4.0	6.6	7.1	1.7	5.8	1.6	4.9	4.3	1.7	0.4
	100	47.9	9.7	4.6	4.5	6.9	6.8	1.6	5.5	1.8	4.3	4.5	1.9	0.4
	150	48.0	9.2	5.0	4.8	6.2	6.9	1.4	5.6	1.8	4.6	4.8	1.7	0.4
Location 4	50	47.6	9.4	5.2	5.3	6.0	7.2	1.8	6.5	1.5	3.8	3.9	1.8	0.5
	100	46.7	9.5	4.8	5.1	6.8	7.0	1.9	6.3	1.3	3.9	4.8	1.9	0.5
	150	46.8	9.3	4.4	4.9	6.4	7.5	1.8	6.8	1.7	4.0	4.2	2.2	0.4
Location 5	50	47.3	10.5	4.8	4.3	6.6	6.8	1.8	5.6	2.4	3.5	4.6	1.8	0.4
	100	46.5	9.0	5.2	4.9	7.2	6.9	1.7	6.0	1.8	4.2	4.5	2.1	0.4
	150	47.7	9.2	5.0	4.7	7.4	7.0	1.9	6.2	1.7	4.1	4.1	1.0	0.4

*The ratio of Garnet + Tourmaline / Amphibole + Pyroxene was used as an index to the heavy minerals weathering intensity (Carver, 1971).

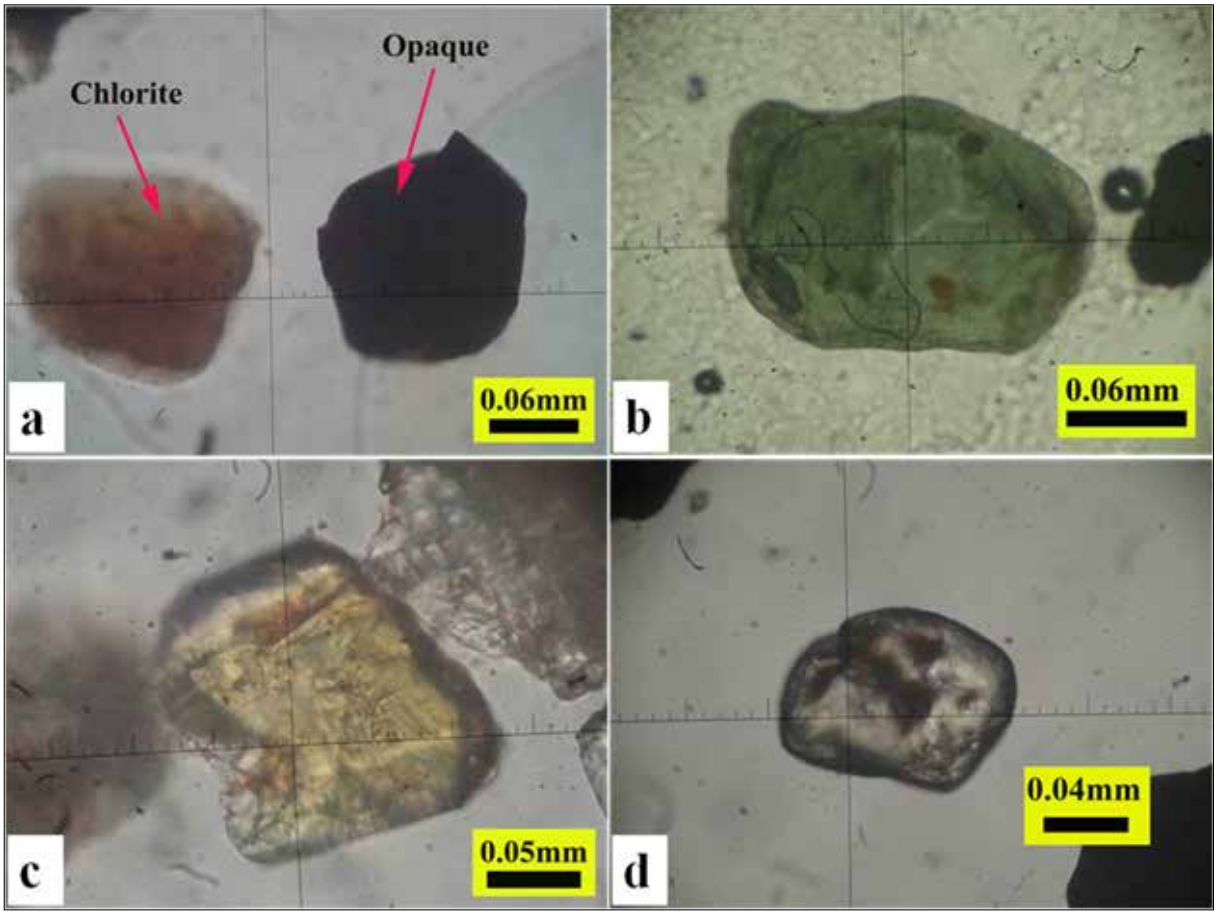

Figure 5. Shows three types of heavy minerals in the study soils a) Chlorite and Opaque Grains, Sample number L5-2, b) Green Chlorite, Sample Number L4-1, c) Epidote, sample number L2-1, and d) Colorless Zircon, Sample Number L3-1

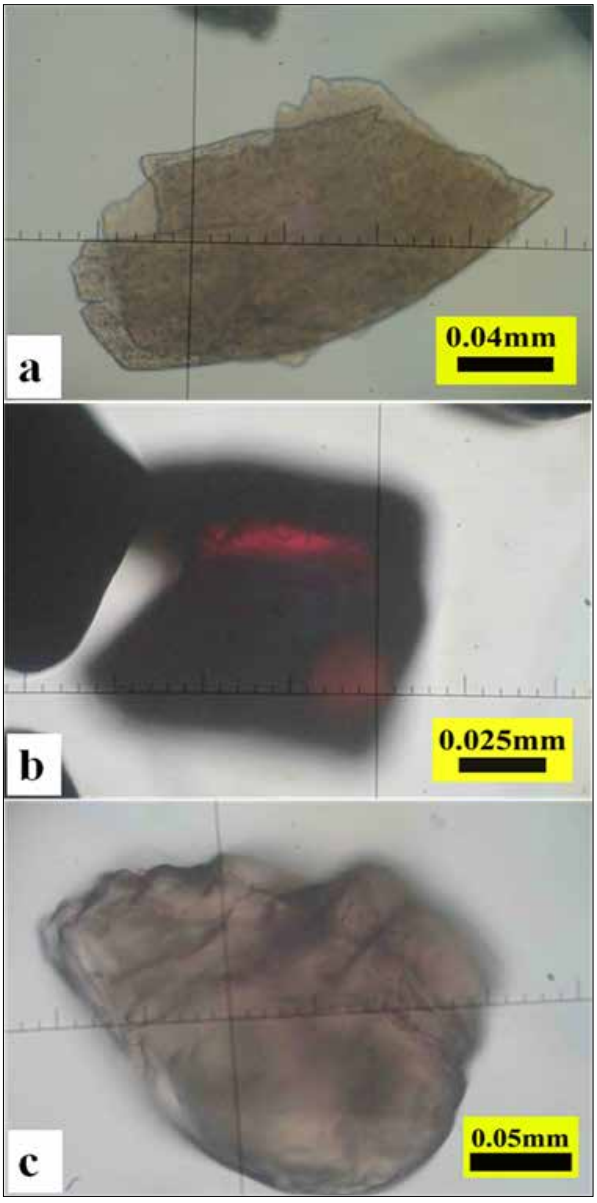

Figure 6. Shows three types of heavy minerals in the study soils: a) Flacky Biotite, Sample Number L2-1, b) Deep Red Rutile, Sample Number L4-1, and c) Tourmaline, Sample Number L1-2

4. Conclusion

Based on the results of this research, it was found that th calcite was dominant in general for all study horizons, as it reached 45.7%. This dominance indicates that the soil-forming material of sedimentary rocks was rich in carbonate. Quartz came in the second place, in dominance, which is one of the most common minerals found in Iraqi soils because of its high resistance to weathering. Weathering values for light minerals showed high values, reaching 9.6%, and this indicates that these soils were subjected to significant weathering, especially in the surface horizons that is due to climatic factors such as heat, wind, and rain.

For the heavy minerals, researchers concluded the dominance of Opaque grains with a ratio of 50.9%, This result indicates that the basic rocks that formed these soils are rocks rich in oxides such as iron and magnesium. Weathering values for heavy minerals were low relative to light minerals, and this finding indicates the severity of weathering to which light metals were exposed in the studied soils.

Based on the types and concentration of heavy minerals present in the studied soil samples, the source of these deposits must be rich in metamorphic and igneous rocks. secondly, it is rich in sedimentary rocks. Therefore, the proposed source for these deposits is the Arabian Shield, in addition to the presence of some sediments transported from sedimentary rocks in the neighboring areas. The high presence of unstable and medium stable heavy minerals, such as Pyroxene and Hornblende, which can indicate the strong influence of transport factors and mechanical weathering compared to the effect of chemical weathering factors, and therefore the most important factor for the transfer of these deposits is wind.

Acknowledgments:

The authors are very grateful to the deanship of the College of Agriculture, University of Sumer for allowing the authors to use the college laboratory devices.

Conflict of Interests

The authors declare that there are no conflicts of interest regarding the publication of this paper.

References

Al-Ankaz, Z.S. (2012). Mineralogy, Geochemistry and Provenance of Dibdibba Formation, South and Middle of Iraq, M.Sc. Thesis, University of Baghdad.

Al-Azami, R.A. (2006). The Effect of the Physiographic Location on the Genetic and Evolutionary Status of Some Gypsum Soils in Iraq, PhD Dissertation, University of Baghdad. In Arabic.

Al-Fatlawi, L.A. (2002). Content and Distribution of Feldspar Minerals in Some Sedimentary Soils, M.Sc. Thesis, University of Baghdad. In Arabic.

Al-Janabi, K.Z., Ali, A.J., Al-Taie, F.H., and Jack, F. J. (1988). Origin and Nature of Sand Dunes in the Alluvial Plain of Southern Iraq. Journal of Arid Environments 14(1): 27-34. DOI: https://doi.org/10.1016/S0140-1963(18)31093-0

Al-Jubouri, D.A. (2010). The Effect of the Type of Vegetation Cover on the Transformations of the Smectite in Some Forest Soils in Northern Iraq, M.Sc. Thesis, University of Baghdad. In Arabic.

Al-Jubouri, S.R. (2014). The Effect of Physiographic Location and Chronological Age of Geological Formations on the Mineral Formation and Weathering Condition of Some Iraqi Soils. Karbala University Scientific Journal 12 (3): 133-144. https://www.iasj.net/iasj/download/273a8abababb22ce . In Arabic.

Al-Khafaji, S.J. and Al-Najar, N. (2010) Some Evidence on the Occurrence of Feldspar Minerals in Sand Deposits of Dibdibba Formation in Nassria Area, Southern Iraq. Iraqi Journal of Desert Studies 2(2): 15-24. https://www.iasj.net/iasj/download/907d6911210fcae8

AlKhalil, Sh.M.A. and Essa, S.K. (2020). Effect of Sedimentation Source on the Nature Occurrence and Distribution of the Feldspar in Some Soil of Alluvial Plain Iraq, M.Sc. Thesis, College of Agricultural Engineering Sciences, University of Baghdad, Iraq.

Al-Shakeri, A.J., Jasim, H.K., Abdullah, H.H., Kadhum, A.K., Thwani, H.H. (2017). Uses of Sand Dunes as Building Materials. Iraqi Journal of Science 58(4A): 1874-1887. DOI: 10.24996/ ijs.2017.58.4A.11

Awwad, A.M., Ahmad, R., and Alsyouri, H. (2009). Associated Minerals and Their Influence on the Optical Properties of Jordanian Kaolin. Jordan Journal of Earth and

Environmental Sciences 2(1): 66-71. http://jjees.hu.edu.jo/files/V2NSPECIAL1/MS_5_Final_Form_9.8.2009%20modified.pdf

Awwad, K.M. (1986). Principles of Soil Chemistry. College of Agriculture, University of Basra, Basra, Iraq.

Bishop, A.C., and Hamilton, W.R. (1974). The Hamlyn Guide to Minerals, Rocks and Fossils. Hamlyn.

Buday, T. and Jassim, S.Z. (1987). The Regional Geology of Iraq, Tectonism, Magmatism and Metamorphism. GEOSURV2, Iraq.

Carver, R.E. (1971). Procedures in Sedimentary Petrology. John Wiley & Sons Incorporated.

Dahnoun, K., and Djadouni, F. (2020). Effects of Heavy-Metal Pollution on Soil Microbial Community, Plants, and Human Health. Jordan Journal of Earth and Environmental Sciences 11(3): 234-240. http://jjees.hu.edu.jo/files/Vol11No4/JJEES_Vol_11_No_4_P1.pd

Jackson, M.L. (1975). Soil Chemical Analysis. Advanced Course. College of Agric., Department of Soil, University of Wisconsin, Madison.

Kerr, P.F. (1959). Optical Mineralogy. McGraw-Hill Book Company, New York.

Milner, H.B. (1962). Sedimentary Petrography. 4th. Ed., Murby and Co. London.

Murray, H.H. (2007). Applied Clay Mineralogy Occurrences, Processing and Application of Kaolins, Bentonites, Palygorskite -Sepiolite, and Common Clays. Elsevier Publications, Netherlands.

Pettijohn, F.J. (1975). Sedimentary Rocks. 3rd Ed., Harper and Row, New York.

Pettijohn, F.J., Potter, P.E., Siever, R. (1972). Sand and Sandstone. Springer, New York.

Pettijohn, F.J., Potter, P.E., Siever, R. (1987). Sand and Sandstone. 2nd Ed., Springer-Verlag, New York.

Rahel, N.Sh. (2008). Pedostratography of Soil Origin Materials for Some Chains in the Irrigated River Basins from the Middle of the Iraqi Alluvial Plain, PhD Dissertation, University of Baghdad. In Arabic.

Shaker, S.N. (1986). The Geomorphology of the Sand Dunes Fields Between Kut, Diwania, and Nasiriyiah Area, M.Sc. Thesis, University of Baghdad, Iraq.

Tucker, M.E. (1985). Sedimentary Petrology an Introduction. Blackwell scientific publ., Oxford.

JJEES

JJEES (2024) 15 (2): 115-122
ISSN 1995-6681

Jordan Journal of Earth and Environmental Sciences

Chemometric Evaluation of Residual Soil Contents: Application to Heavy Metals at Public Parks in Amman - Jordan

Mohammad Al-Hanini[1], Zeyad Makhamreh[2], Ramia Al Bakain[1*]

[1]Department of Chemistry, School of Science, The University of Jordan, Amman, Jordan
[2]Department of Geography, School of Arts, The University of Jordan, Amman, Jordan

Received September 19, 2023; Accepted November 15, 2023

Abstract

In this study, selected heavy metals, present in park soil samples from different areas in Amman-Jordan, were evaluated. Soil samples were collected from 30 different parks in 3 different areas during the summer season. The physiochemical properties that play a main role in metal mobility were determined, such as pH that showed neutral to alkaline values. The moisture content revealed low value due to the high evaporation level during sample collections, and finally, the organic matter content was full in high contents. Park soils' metal contents were extracted and then examined by flame atomic absorption spectroscopy. The data were exposed to principle component analysis and hierarchical cluster analysis to reveal the variations of park metal levels as a result of geographical park areas, to show the metals that were responsible for clustering parks, and finally, to facilitate the future metal's location prediction and parks clustering of unknown soil samples based on their metal contents. The results showed that thirty parks of different soil samples were grouped into two clusters. Among the parks, two areas of high traffic jams and construction processes were clustered together due to the distinct content of Pb, Cu, and Ni where the third area shows distinct content of Zn that was responsible for clustering parks of this area alone. Classification of park soils according to the similarities of their chemical contents based on Flame Atomic Absorption Spectrometry outcomes will help define the sources of the studied heavy metals and provide clear information about the common health symptoms / issues caused by exposure to these heavy metals in the areas that have been clustered in one group.

Keywords: *Park soils, Principal Component Analysis, Cluster analysis, Geographical prediction, Heavy metals.*

1. Introduction

Heavy metals are natural constituents of the earth-crust and are emitted to the environment in different ways: combustion of fossil fuel and road traffic, tears of tires, corrosion of building materials, automobile bodies, brake lining, industry, and human activities. Then, they are settled in soil, water, air, dust and sediments, fertilizer, and sewage. Consequently, they accumulate in the top layer (Mashal et al., 2017; Li et al., 2014; Aaseth et al., 2016; Kumar et al., 2015). Increasing industrialization has been accompanied throughout the world by the extraction and distribution of mineral substances from their natural deposits. Many of these substances have undergone chemical changes through technical processes, and are finally dispersed in solutions by different ways of effluent, sewage, dumps, and dust, into the water, the earth, and the air and thus into the food chain (Al Bakain et al., 2012a). Thus, the threat posed by heavy metals to human health and the environment has risen sharply; hence, there is rising public health interest in the possible effects of heavy metals on human health (appendix 1). Many investigations were carried out to determine the levels of heavy metals in different areas and materials worldwide, including sediment (Bany Yaseen et al., 2019; Irvine et al., 2009), street dust and surface soils (Tarawneh et al., 2021; Lee et al., 2005), and in different parks and gardens (Lorraine et al., 2015; Gu et al., 2018; Wang et al., 2019). Heavy metals can enter human bodies in many ways; the common modes of intake of external materials are inhalation of air into the lungs, ingestion of food, water, and at times non– food items into the gastrointestinal system and transfer through the skin intravenous, intramuscular and vaginal routes (Al Bakain et al., 2012a). Identifying the level of the heavy metals and their toxicity degree in the living areas is required, especially in the areas where children gather since they ingest quantities of soil dust when they play in parks or gardens more likely than adults with their habit of placing dirty fingers and objects into their mouths (Al Bakain et al., 2012a). Therefore, they are more susceptible to the intake of toxins than adults are which is risky since maximal brain growth and differentiation are found in the first few years of life.

Open parks are one of the favorite places for children to spend time. The distribution of heavy metals in the soil in parks is related to natural and anthropogenic sources (Lorraine et al., 2015; Gu et al., 2018; Wang et al., 2019) such as the food residues, application of irrigation water (surface or groundwater), and construction activities nearby the park's areas. Many studies focused on the concentration of heavy metals and their sources in different parks worldwide (Lorraine et al., 2015; Gu et al., 2018; Wang et al., 2019; Paukszto et al., 2018; El Hamiania et al., 2010). In the USA, Lorraine et al., 2015 evaluated Pb, As, and Cd levels in 12 parks in Los Angeles to find high levels of Pb (> 80 mg/Kg) in 11 gardens, where the As level was > 5 mg/Kg, then

* Corresponding author e-mail: r.bakain@ju.edu.jo

finally, Cd concentration was found to be < 2 mg/kg in all samples. In China (Gu et al., 2018), 28 urban soil parks in Guangzhou city were studied to find that Cd, Pb, Ni, Cu, Zn, and Mn were higher than their background value due to anthropogenic sources. Another study was carried out in China, where 34 soil samples from 6 parks in Jiaozuo-Henan Province were collected (Wang et al., 2019), and the results showed that the concentration of As, Zn, Co, and Ni was higher than the background value. In Tatra National Park-Poland, a high content of soluble compounds of the tested metals was obtained due to the long-term flow from the south and west of Poland to the studied area (Paukszto et al., 2018). In Morocco, 16 garden soil samples were collected from the area adjacent to a mining area (El Hamiania et al., 2010) to find that Cr concentration was above the acceptable value (50 mg Kg^{-1}), and Mn concentration was very high (i.e. exceeded 900 $mg.kg^{-1}$). The mobility of heavy metals in soil is affected by many factors: organic matter content, structure, moisture, and pH (Murray et al., 2004; Imperato et al. 2003). When pH decreases, the ions begin to break free of their compounds and hence, the solubility of the heavy metals in the form of ions will increase and that leads to the increase of the mobility in soils. High carbonate content enhances the pH, which promotes precipitation of metals in the soil. The change in pH during the extraction depends on the composition of the sample and affects the amount of the metal leaching considerably (Al Bakain et al., 2012a; Murray et al., 2004; Imperato et al. 2003).

Principal component analysis (PCA) and hierarchical cluster analysis (HCA) are useful tools in analytical chemistry that are used for classifications (Al Bakain et al., 2011; Al Bakain et al., 2021a; Al Bakain et al., 2020; Al Bakain et al., 2021b; Al-Hyasat et al. 2021; Liu et al., 2023). These tools were performed in many studies for many purposes to identify the content most important in distinguishing the sample varieties, to find the variation in chemical profiles as a result of different batches, to confirm whether the areas in the cluster analysis would also be grouped, and to reveal the compounds that were responsible for grouping the areas between clusters.

There is currently no available systematic clustering for the park soils' heavy metals content in Jordan. Hence, this study was implemented to examine the metal contents of 30 park soils. For the first time, park soils were obtained from different areas in Amman, extracted, and analyzed using Flame Atomic Absorption Spectroscopy (FAAS). The Zn, Pb, Cu, and Ni metals were evaluated to reveal all possible metals necessary for park clustering. Grouping the soil samples from different parks was accomplished, using unsupervised clustering methods (i.e. PCA and HCA). To the best of our knowledge, this study is the first to classify the park soil samples in Amman-Jordan and to use the PCA and HCA to predict the location for future park soil samples, considered for blind analysis.

2. Experimental

2.1. Sampling areas

Thirty public parks, distributed in different neighborhoods in Amman, have been selected as sampling areas (Table 1). The studied parks represent different locations, types of soil, ages of buildings around, street types (i.e. major or minor), and human activities. Sampling locations are shown in Figure 1.

2.2. Sampling

From each park, representative soil samples were collected during the summer season in Amman (i.e. August-October 2019), and then transferred to a polyethylene bag. Areas of the parks were varied from 675 m^2 to 8747 m^2. The number of the collected samples was varied according to the area of each park to be from 25 to 300 samples.

2.3. Chemicals and Instrumentations

All glassware, polypropylene test tubes, and funnels were initially cleaned with soap, washed thoroughly with tap and distilled water, and soaked overnight in 10 %HNO_3 (v/v) to remove any contamination by heavy metals. Centrifuge (Model, PK 130), oven (Binder, IP 20, Germany), muffle furnace (Carbolite, S33 6RB, England), water bath shaker (Jeio tech, BS-11, Korea), sieve 125 µm (Model Retsch, G.M, B.H, Germany), pH meter (HANNA, HI-2002 Edge, USA), and ultrasonic bath (Model, 50T, New York) were used in this work. A standard solution of Pb, Zn, Cu, and Ni of 1000 ppm was implemented to prepare the solutions based on the following concentrations: Zn: 0.05, 0.5, 1 and 2 ppm, Ni: 0.5, 1, 3, and 5 ppm, Cu: 0.05, 0.5, 1, 3 and 5 ppm, and Pb: 1, 2, 5, and 15 ppm. The HNO_3 analytical grade 65% (Scharleau, Spain) solvent was applied to extract the heavy metals from the soil samples. The standard Reference Material (SRM) NIST 1646 was purchased from Sigma-Aldrich. Determination of heavy metals was carried out on FAAS (Varian 55B model) according to the following conditions: Air acetylene was the fuel of 1.5 L/min fuel flow, slit width was 0.2 nm, lamp current was 5, 6, 5, 7 mA, and finally, the wavelengths were 217.0, 224.7, 213.9 and 232.0 nm for Pd, Cu, Zn, and Ni respectively.

2.4. Sample Pretreatment

For all representative soil samples, large debris and stones were removed, then the filtered soil was grounded, using a ceramic mortar and pestle to assure homogeneity, sieved through a 125 µm sieve, and finally, stored in polyethylene bags in a freezer at -20˚C prior to analysis.

2.5. Moisture and Organic-Matter Content

The moisture content was determined by weighing around 1.0 g of each park soil sample, then was heated in an oven at 105ºC for 12 hrs. until reaching constant weight. The weight loss was calculated based on the difference between the final and the initial weight. The same dried sample was then transferred into a muffle furnace at 550º C for 4 hrs. in order to determine the organic matter content, which was then calculated gravimetrically based on the weight difference.

2.6. pH Measurement

The pH meter has been calibrated at pH 4 and 7 buffer solutions at room temperature. Then, the pH value of the water extract of each park soil sample was determined by dissolving the soil in milli-Q water (1: 2.5 wt/v) in 15 polypropylene test tubes.

Table 1. Description of the sampling areas in Amman- Jordan.

Park Group	Park No.	Park Name	Site
A	1	Queen Noor	Almadina
A	2	Ammar bin Yasir	Basman
B	3	Alabdallat	Marka
B	4	Iskan alamana	Marka
B	5	Alouda	Al Nasr
A	6	Khawla bent Alazwar	Yarmouk
A	7	Um almuminin	Ras Al Ain
A	8	Kafr Ra'i	Badr
A	9	Al Mutanabi	Zahran
A	10	Aldiyar	Zahran
A	11	Teacher Samir Al Rifai	Abdali
A	12	Bilal bin Rabah	Abdali
B	13	Alhilal	Tariq
C	14	The princess Badiea	Al Qwiesma
C	15	Juwaida	Al Qwiesma
C	16	Mutah	Khuraibet Al-Souq
C	17	AlMuqabilin Almuktabia	Al-Muqabilin
C	18	The Petra	Al-Muqabilin
B	19	Judge Moussa Al Saket	Sweileh
B	20	Um Omar	Sweileh
A	21	Almururia	Tlaa Al-Ali
A	22	The Hashemite Flag	Jubaiha
B	23	Al Manhal	Jubaiha
B	24	Independent Park	Shafa Badran
C	25	Hussain Al-Khawaja	Wadi Seer
B	26	Alshaeb	Wadi Seer
A	27	Alshilal	Wadi Seer
B	28	Abu Naseer 1	Abu Naseer
C	29	Albunaiat	Al-Muqabilin
C	30	The Honorable Rock	Ras Al Ain

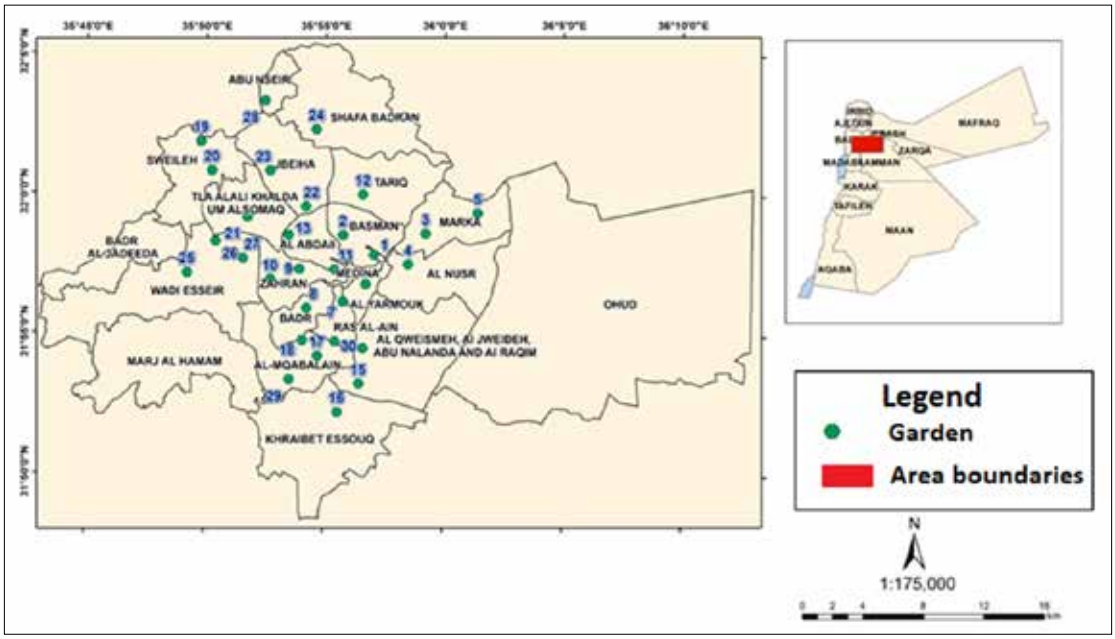

Figure 1. Map of the sampling sites in Amman (the numbers from 1 to 30 are the parks names as identified in Table 1).

2.7. Acid-Extractable Fraction of Heavy Metals

The extraction of heavy metals from park soil samples was carried out by weighing around 0.7 g of dry sample. Then, 15 mL of concentrated HNO_3 was added in 50 mL polypropylene test tubes, heated for 2 h at 95º C in a water bath shaker, sonicated for 30 mins in ultrasonic bath at 50º C, then centrifuged for 15 mins at 1000 rpm (Al Bakain et al., 2012a). The sample was then diluted with 1% HNO_3. Blank solutions and the SRM were prepared in the same way as employed for the real samples.

2.8. Validity and Quality Control

To evaluate the analytical precision and accuracy of the analytical procedure, blank reagents, replicate samples, and standard reference material were implemented. Blanks were prepared in a similar manner to that of the real samples and were analyzed before each measurement. All extractions and analyses were made in triplicate (n = 3) for quality assessment, and the average results were reported. The analysis of SRM was conducted and compared to the results reported in the certified values. The SRM was subjected to the extraction, and then the results were reported as the percent recovery.

2.9. Statistical data treatments

2.9.1 Multivariate analysis of park soil samples using unsupervised clustering methods

The main targets for applying multivariate analysis in chemistry are grouping, clustering, discriminating, and classifying objects (samples, compounds, or materials), besides modeling relationships among different analytical data (Al Bakain et al., 2020). In grouping or clustering, park soil samples would be grouped according to their chemical composition, elemental pattern, or technological properties. In classification, soil samples would be classified into known class membership based on their elemental pattern, chemical composition, or spectra (Otto, 2016; Sipos et al, 2005). Generally, there are two main methodologies adopted for grouping or clustering known as unsupervised and supervised methods. For unsupervised methods, a grouping of analytical data is carried out by projecting the high dimensional data into a lower dimensional space, and since there is no supervisor to relate the membership of samples to classes, then unsupervised methods are performed in a supervised manner (Al-Hyasat et al., 2021; Brereton, 2007). Both Principal Component Analysis PCA and Hierarchical Clustering HCA methods are typical examples of unsupervised methods (Otto, 2016; Brereton, 2007). In this study, HCA and PCA were performed to confirm whether the soil samples obtained from different parks would be grouped based on the analysis results of the heavy metal contents in each sample. PCA can reveal the metal/s that is/are responsible for grouping soil samples of origin. Such classification results may have value for environmental researchers in the discrimination and selection of park soil samples. These results may help to show the similarities and differences between soil profiles across Amman.

2.9.2 Arrangement of chromatographic data

The data were arranged as a data matrix X of samples and variables. For the current case, matrix X has the size of 30×30 (i.e. 30 parks) × 4 heavy metals. Matrix X was subjected to different clustering methods as will be discussed below. None of the collected samples were assigned to a class membership; hence, unsupervised clustering methods were applied (Al Bakain et al., 2020).

2.9.3 Principal component analysis:

PCA is a data compression method based on the correlation among variables. It aims to group those correlated variables, while replacing the original ones by a new set, called the principal components (PCs), onto which the data are projected (Al Bakain et al., 2012b). These PCs are completely uncorrelated and are built as a simple linear combination of the original variables. It is important to point out here that the PCs contain most of the variability in the data set, albeit in a much lower dimensional space. The first principal component, PC1, is defined in the direction of maximum variance of the whole data set. PC2 is the direction that describes the maximum variance in the orthogonal subspace to PC1. The subsequent components are taken orthogonal to those previously chosen and describe the maximum of the remaining variance (Liu et al., 2023; Otto, 2016; Brereton, 2007). Once the redundancy is removed, only the first few principal components are required to describe most of the information contained in the original data set. In this study, two data matrices were built. The data matrix X (30×30) is decomposed into two matrices: T (score matrix) and L (loading matrix), using a suitable PCA algorithm. The first step in PCA is the computation of loadings. Mathematically, the loadings are the eigenvectors of the matrix (XXT). There are several methods to estimate the eigenvectors, such as singular value decomposition (SVD) and NIPALS (non-linear iterative partial least-squares) in the order of explained proportion of the variations in X until a certain pre-established number of components (Al Bakain et al., 2020). The loadings are grouped into a matrix L. The collected loadings are orthonormal, meaning they are both orthogonal and normalized. The relationship between the original matrix X, the loading matrix U, and the score matrix T is described (Otto, 2016; Brereton, 2007):

$$X = TLT \quad (1)$$

Mathematically, matrix X is decomposed in the product of two matrices, T and L, on the condition that L is formed by orthonormal columns. T is obtained as T = XTL. In this work, the size of X is 30×30, while size T is 30×h and L is h×30, where h is the number of factors needed to decompose matrix X. The optimum number of factors (h) is necessary to create the optimum number of loadings and scores and produce informative discrimination among soil samples (Al Bakain et al., 2020). As initial variables are assigned into four different groups (i.e. 4 heavy metals), then it is possible to classify soil samples based on heavy metals` levels.

2.9.4 Hierarchical clustering analysis

The main strategy of unsupervised methods is based on cluster analysis where the soil samples are aggregated stepwise according to the similarity of their features or variables (i.e., contents of heavy metals). As a result, hierarchically ordered clusters are created. In HCA, the collected data is displayed in a certain way to emphasize their natural clusters and patterns in a two-dimensional space. The results are often presented in the form of dendrograms,

which allow quick visualization of clusters and correlations among tested samples. The similarity between samples can be evaluated following a suitable distance measure, which is commonly applied in pattern recognition. Euclidean distance d (which is a special case for Minkowski distance) between samples is estimated as (Brereton, 2007):

$$d_{i,k} = [\sum_{k=1}^{K} (x_{i,k} - x_{j,k})^2]^{1/2} \quad (2)$$

where K and i/j are the number of variables measured for samples and indices for samples respectively. Estimations would be made using the main principal components of the original data after decomposition by PCA. Initially, $d_{i,k}$ is estimated between all samples (i.e., every sample is to be compared with the remaining samples) to create the distance matrix. The similarity or aggregation between samples is then estimated using the weighted average linkage method (Brereton, 2007).

2.10. Statistical software

The statistical analysis, including principal component analysis PCA and hierarchical cluster analysis HCA, was performed using Chemoface 1.61 software which runs under MatlabVR (Mathworks, 8.6, USA).

3. Results and Discussion

3.1. Physico-chemical soil properties

Moisture (Mois) content, organic matter content (OM), and pH have been evaluated (Figure 2). The pH is a test for measuring the binding strength and potential mobility of heavy metals in soil (Al Bakain et al., 2012a). Metal solubility decreases at high pH values, which leads to metal precipitation. The results of pH measurements showed that all park soil samples in the 3 areas (A, B, and C) were neutral to alkaline (i.e. pH > 7). The pH values were varied between 7.86 and 12.27, with an average of 8.52. This result referred to the difference in waste composition that might affect the pH values, such as the food residues, application of irrigation water (surface or groundwater), construction activities near the parks area, and cleaning rate of the park areas. Moreover, the nature of the soil in Jordan is almost calcareous (i.e. high carbonate content), which raises the pH values (Al Bakain et al., 2012a). Carbonate provides a buffer against the mobilization of metals and facilitates metal's precipitation (Sipos et al., 2005).

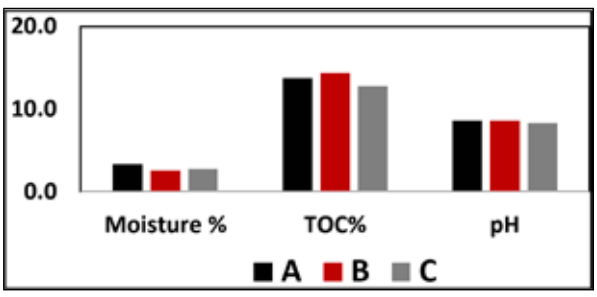

Figure 2. Average physico-chemical soil properties for the studied parks in Amman.

The soil samples from area A showed high pH values since this area consists of new hotels, shopping centers, and office buildings in Amman (Abdali). Moreover, areas A and B had big construction phases during our sample collection.

Regarding the moisture content of the 30-park soil, the values were low, and there was no variation among the three areas as shown in Figure 2. The highest moisture content was 3.33% at area A followed by 2.78% and 2.57% for areas C and B respectively. These results are related to the high temperature recorded in Amman during the sample collection (August-October 2019) with an average of 38°C.

The average organic matter (OM%) content was 13.77%, 14.38%, and 13.78% for areas A, B, and C respectively. The OM% in the studied areas ranged between 7.97% and 21.07%. The differences in OM % values between the studied areas can be attributed to the organic contaminants caused by the residues of food, animal, cartons, papers, and car emissions such as fuel and oils, smelting, chemical fertilizers, mining emissions, in addition to grass and vegetation that cover the soil (Al-Khashman et al., 2006) at the studied park soil areas.

3.2. Total heavy metals

In order to assess the accuracy of the results obtained by the analytical method implemented in this study, two methods were provided: blank solutions and SRM. The recovery of the heavy metals in NIST (1646 a) was (95.60%, 105.04 %, 97.21 %, and 85.52%), and the detection limit was 0.01, 0.10, 0.02, and 0.07 mg/L for Zn, Pb, Cu, and Ni respectively. The averages of heavy metals concentrations (mg/Kg) in the 30 investigated park soil samples are illustrated in Figures 3 and 4.

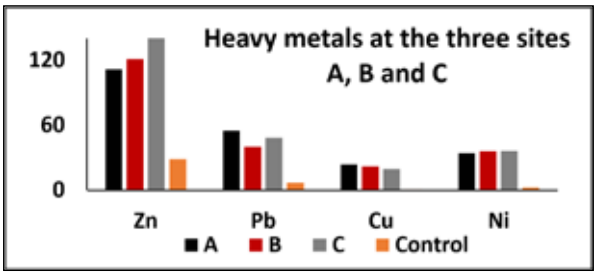

Figure 3. The average total concentrations (mg/Kg) of heavy metals in the soils of the three park areas.

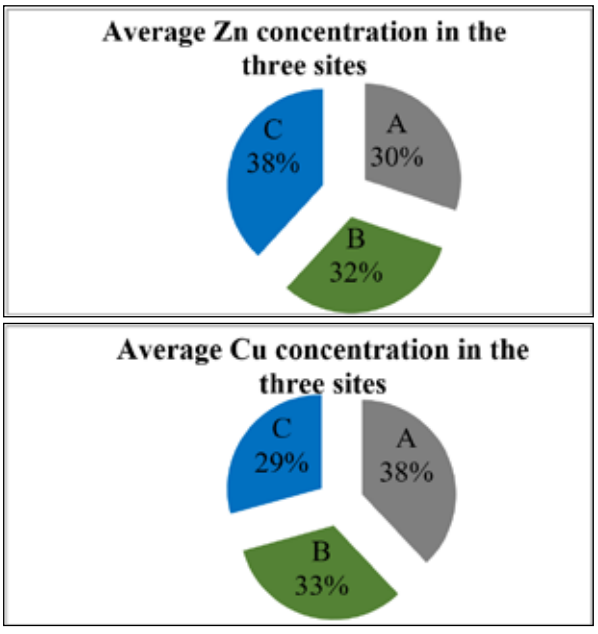

Figure 4. Average concentrations of each metal in the three studied areas.

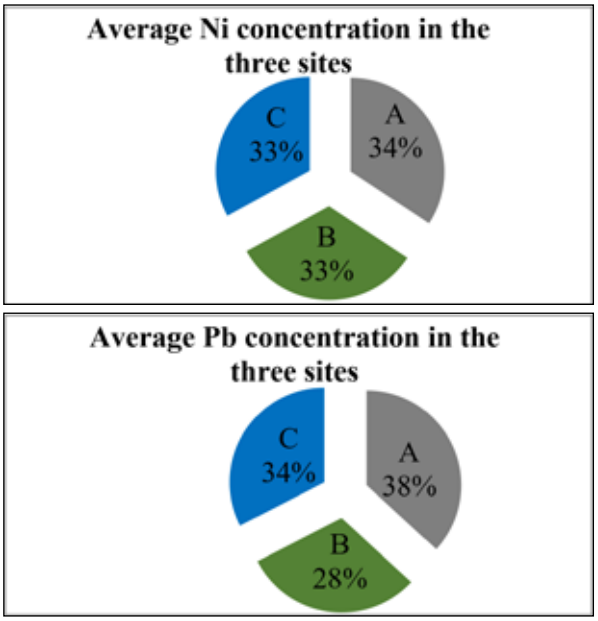

Figure 4 (contin.) Average concentrations of each metal in the three studied areas.

Generally, zinc occurs naturally in soil with about 70 mg/kg in crustal rocks and also from the high density of vehicular traffic (Al-Khashaman et al., 2006). The three park areas showed high levels of Zn (115.60, 121.17, 146.21 mg/kg at A, B, and C respectively) since these areas have intense traffic jams with busy vehicles movements all over the day. Since Zn exists in the carburetors, pumps, and automobile door panels, hence, high levels of Zn are expected. Moreover, the majority of the three park areas are located on major or minor busy streets, nearby bus stations, have busy cafes with outdoor Hookah and high traffic jam neighborhoods. The average concentration of Zn of the control sample was 28.68 mg/Kg; this indicates that the soil samples in all parks have higher levels than the control area as seen previously in Figure 3.

Regarding Ni, the average concentrations at all park samples in all areas were close to each other (37.72, 36.07, and 36.27 mg/Kg, in A, B, and C respectively). This result refers to the usage of Ni in many specific and recognizable consumer products, including stainless steel, alnico magnets, coinage, rechargeable batteries, and special alloys and green tint in glass (Davis, 2000).

For lead, the average concentration was 54.86, 45.58, and 48.48 mg/kg respectively. The average concentration of Pb in the control sample was 6.83 mg/Kg. In fact, the main source of Pb in the completely studied areas is attributed to the automobile exhausts that use Pb as an anti-knock agent in the combustion of gasoline. Since the majority of public park areas have very intense traffic jams, hence a high percentage of Pb is expected.

Finally, the average concentration of Cu was found to be 25.38, 21.90, and 19.56 mg/kg at A, B, and C areas respectively. The sources of Cu are wires, electric device tailing, and plating materials that use copper to protect the surface of the brass alloy, bars, and winding in the motor and generator of the buses (Kartal et al., 2006).

3.3. Statistical data treatment

As indicated in Figure 5-A, two main clusters collect the 30 parks at the three areas. Cluster of group I collects 6 parks, where cluster II collects 24 parks. HCA analysis revealed the same and/or comparable constituents of park soil contents of heavy metals. It is clearly appeared that cluster II (22 parks from locations A and B, and only 2 parks from location C) are overlapped which means that these parks' soils have similar or very comparable metal contents. Regarding group I, it has only parks from area C, which means that the park soils of this area have the same metal contents. To clarify these results, the average concentrations have been taken, and HCA has been re-carried out to reveal Figure 5-B. The order of the average Zn and Pb contents in all the areas was C > B > A and A > C > B, respectively. Cu and Ni metals showed the same order of A > B ≈ C. Location C shows distinct content of Zn that clusters the parks from area C together, but far from locations A and B, which means that Zn is responsible for clustering C alone. This result clearly appeared on PCA, Figure 5-C which revealed that the data loading collected was 99.99% of the whole information from PC1 and PC2.

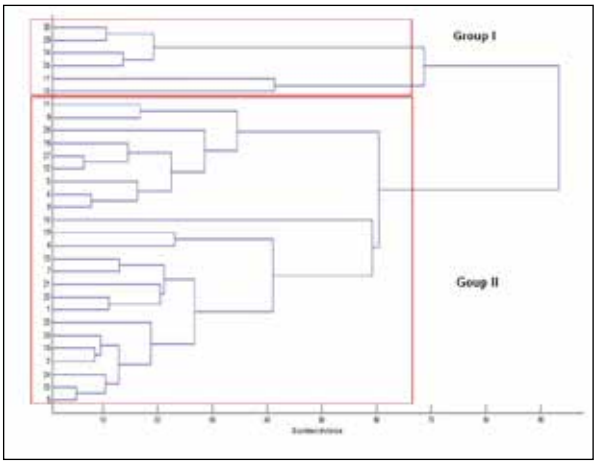

Figure 5A. Dendrogram of the 30 park soil-origin samples of metal contents

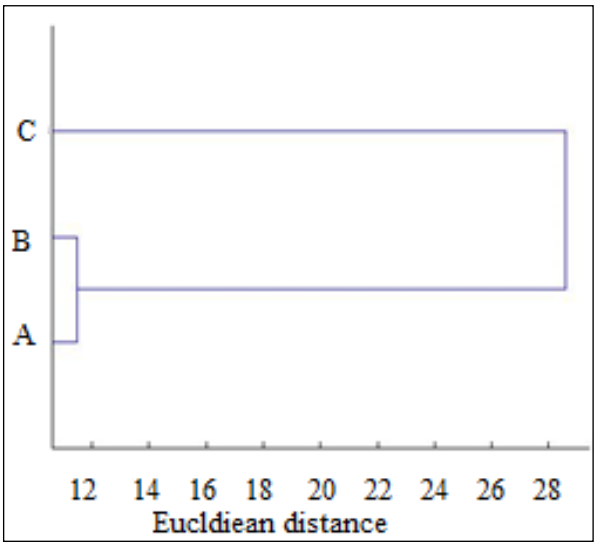

Figure 5B. Dendrogram of the 30-park soil origin samples of metal contents in average.

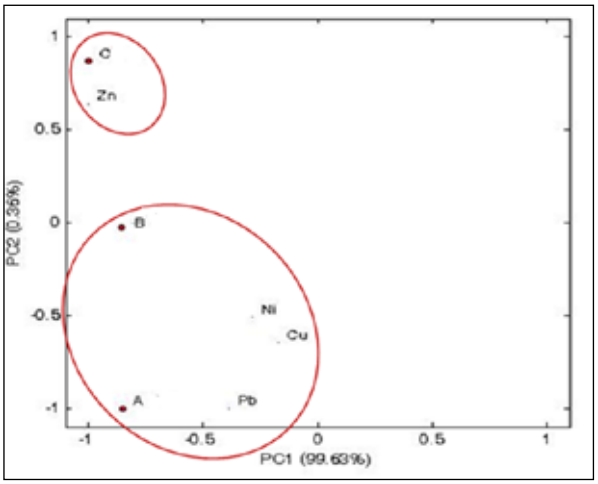

Figure 5C. PCA output: bi-plot obtained from the 30 origin parks soil contents.

4. Conclusion

This study has been carried out in order to achieve SDG#3, good health and well-being, since it detects sensitive metals that affect human health, hence, this will raise the awareness of the major sources of heavy metals that may lead to health issues. Based on the results of the current study, the average pH values at all park soil samples in Amman area were neutral to alkaline, where the moisture contents were low due to the evaporation rate based on the high temperature in the summer that decreases the moisture content. Regarding the organic matter, it was found at a high level due to the high level of organic contamination in all areas. FAAS was used to evaluate the Zn, Pb, Cu, and Ni contents of 30 park soil samples in 3 areas. The metal concentrations showed higher levels than the control areas at the whole park. The metal contents were used to group soil samples with the help of PCA and HCA. The grouping outputs uncovered the geographical origin of soil samples. By HCA and PCA, the 30-park soil origins were classified into two clusters: 24 parks from areas A and B due to the close contents of Pb, Cu, and Ni, and 6 parks in area C due to the distinct constituents of Zn.

Acknowledgment

This project was implemented, thanks to the financial support provided by (1) The University of Jordan, (2) L'Agence Universitaire de la Francophonie-Moyen Orient (AUF - Moyen Orient), and (3) Elsevier Foundation.

Conflict of Interests

The authors declare that there are no conflicts of interest regarding the publication of this paper.

References

Aaseth, J., Crisponi, G., Andersen, O. (2016). Chelation Therapy in the Treatment of Metal Intoxication, (1st ed.).

Al Bakain, R., Al-Degs, Y., Cizdziel, J., Elsohly, M. (2021a). Comprehensive chromatographic profiling of cannabis from 23 USA States marketed for medical purposes. Acta Chromatographica 33(1): 78-90.

Al Bakain, R., Al-Degs, Y., Cizdziel, J., Elsohly, M. (2020). Comprehensive classification of USA cannabis samples based on chemical profiles of major cannabinoids and terpenoids. Journal of Liquid Chromatography & Related Technologies 43(5-6): 172-184.

Al Bakain, R., Al-Degs, Y., Cizdziel, J., Elsohly, M. (2021b). Linear discriminant analysis based on gas chromatographic measurements for geographical prediction of USA medical domestic cannabis. Acta Chromatographica 33(2): 179-187.

Al Bakain, R., Rivals, I., Sassiat, P., Thiébaut, D., Hennion, M-C., Euvrard, G., Vial, J. (2011). Comparison of different statistical approaches to evaluate the orthogonality of chromatographic separations: application to reverse phase systems. Journal of Chromatography A 1218(20): 2963– 2975.

Al Bakain, R., Rivals, I., Sassiat, P., Thiébaut, D., Hennion, M-C., Euvrard, G., Vial, J. (2012b). Impact of the probe solutes set on orthogonality evaluation in reverse phase chromatographic systems. Journal of Chromatography A 1232: 231– 241.

Al Bakain, R., Jaradat, Q., Momani, K. (2012a). Indoor and Outdoor Heavy Metals Evaluation in Kindergartens in Amman, Jordan. Jordan Journal of Physics 5(1): 43-52.

Al-Hyasat, M., Al Bakain, R., Vial, J., Thiebaut, D. (2021). Geographical Prediction of Parsley Origins Based on Chromatographic Fingerprinting and Quantitative Analysis: Application to Mediterranean Cultivars. American Journal of Chemistry 11(4): 66- 80.

Al-Khashman, A., Shawabkeh, R. (2006). Metals distribution in soils around the cement factory in southern Jordan. Environmental Pollution 140(3): 387-394.

Bany Yaseen I., Al-Hawari Z., (2019). Assessment of Metal Pollution of the Surface Sediments along the Wadi Al Rayyan area, Jordan. Jordan Journal of Earth and Environmental Sciences. 10(2): 75-84.

Brereton, R. G. (2007). Applied Chemometrics for Scientists. John Wiley & Sons, Ltd, England.

Clarke, L., Jenerette, G., Bain. (2015). Urban legacies and soil management affect the concentration and speciation of trace metals in Los Angeles community garden soils. Environmental Pollution 197: 1-12.

Davis, R. (2000). Nickel, Cobalt, and Their Alloys. ASM International.

El Hamiania, O., El Khalil, J., Lounatea, K., Sirgueyb, C., Hafidic, M., Bittond, G., Schwartzb, C., Boularbaha, A. (2010). Toxicity assessment of garden soils in the vicinity of mining areas in Southern Morocco. Journal of Hazardous Materials 177(1-3): 755–761.

Gu, Y-G., Gao, Y-P. (2018). Bioaccessibilities and health implications of heavy metals in exposed-lawn soils from 28 urban parks in the megacity Guangzhou inferred from an in vitro physiologically-based extraction test. Ecotoxicology and Environmental Safety 148:747–753.

Imperato M., Adamob P., Naimoa D., Arienzob, M., Stanzionea, D., Violanteb, P. (2003). Spatial distribution of heavy metals in urban soils of Naples city (Italy). Environmental Pollution 124(2): 247-256.

Irvine, K., Perrelli, M., Ngoen-klan, R., Droppo, I. (2009). Metal levels in street sediment from an industrial city: spatial trends, chemical fractionation, and management implications, Journal of Soils and Sediments 9(4): 328–341.

Kartal, S., Aydin, Z., Tokalioglu, S. (2006). Fractionation of metal in street sediment sample by using the BCR Sequential extraction procedure and multivariate statistical elucidation of the data. Journal of Hazardous Materials 132(1): 80-89.

Kumar, V., Kalita, J., Misra, U.K., Bora, H.K. (2015). A study of dose response and organ susceptibility of copper toxicity in a rat model. Journal of Trace Elements in Medicine and Biology 29: 269-74.

Lee, P-K., Yu, Y-H., Yun, S-T., Mayer, B. (2005). Metal contamination and solid phase partitioning of metals in urban roadside sediments. Chemosphere 60(5): 672-689.

Li, Z., Ma, Z., Van der Kuijp, T.J., Yuan, Z., Huang, L. (2014). A review of soil heavy metal pollution from mines in China: pollution and health risk assessment. Science of the Total Environment 468-469: 843-53.

Liu J., Kang H., Tao, W., Li, H., He, D., Ma, L., Tang, H., Wu, S., Yang, K., Li, X. (2023). A spatial distribution – Principal component analysis (SD-PCA) model to assess pollution of heavy metals in soil. Science of the Total Environment 859(1): 160112.

Mashal K., Salahat, M., Al-Qinna, M., Ali, Y. (2017). Assessment of Heavy Metals in Urban Areas of Al Hashmiyya City of Jordan. Jordan Journal of Earth and Environmental Sciences 8(2): 61-67.

Murray, K.S., Rogers, D.T., Kaufman, M.M. (2004). Heavy metals in urban watershed in southeastern Michigan. Journal of Environmental Quality 33: 163-172.

Otto, M. (2016). Chemometrics: Statistics and Computer Application in Analytical Chemistry, 3ed Edition. Wiley-VCH, USA.

Paukszto, A., Mirosławski, J. (2019). Using stinging nettle (Urtica dioica L.) to assess the influence of long term emission upon pollution with metals of the Tatra National Park area (Poland). Atmospheric Pollution Research 10(1): 73-79.

Sipos, P., Németh, T., Mohai, I., (2005). Distribution and possible immobilization of lead in a forest soil (Luvisol) profile. Environmental Geochemistry and Health 27(1):1-10.

Tarawneh, K., Eleyan, I., Alalwan, R., Sallam, S., Hammad, S. (2021). Assessment of heavy metals contamination levels in surfaces soil in Baqa'a area, Jordan. Jordan Journal of Earth and Environmental Sciences 12(3): 285-294.

Wang, M., Han, Q., Gui, C., Cao, G., Liu, Y., He, X., He, Y. (2019), Differences in the risk assessment of soil heavy metals between newly built and original parks in Jiaozuo, Henan Province, China. Sci. Total Environ, 676: 1–10.

Appendix 1. (Aaseth et al., 2016; Li et al., 2014; **Lorraine** et al., 2015).

Element	Toxicity
Lead	Inhibits different biological processes in nervous system, heart, and kidneys, causing headaches, anemia, and death.
Cadmium	Hazardous for the nervous system, kidneys, liver, lungs and could also affect bone. Causing fever, chills, body aches, and joint pain.
Iron	Duo to increasing the concentration level of Fe above the threshold value that causes abdominal pain, vomiting, lethargy, and diarrhea.
Copper	Accumulating of copper leads to several problems like hypotension, abdominal pain, liver damage, kidneys and brain.
Zinc	Loss of taste, infertility, birth defects, chronic diarrhea, kidney disease, white spots on fingernails.
Nickel	Hazardous to the respiratory system, immune system, nasal cavities and sinuses, and the skin.

JJEES

JJEES (2024) 15 (2): 123-128
ISSN 1995-6681

Jordan Journal of Earth and Environmental Sciences

Phytoremediation of Contaminated Soil with Pyrene Using Sunflower (Helianthus annuus)

Kholoud Mashal[1], Fakher J. Aukour[1], and Ismail Al-Hunity[2]

[1]Department of Land Management and Environment, Prince El Hasan Faculty of Natural Resources and Environment, The Hashemite University, Zarqa, Jordan.

[2]Environmental Engineer at Greater Amman Municipality. Amman, Jordan.

Received July 25, 2023; Accepted October 23, 2023

Abstract

The study was conducted to evaluate the potential use of Sunflower (Helianthus annuus) to remediate contaminated soil with pyrene in phytoremediation experiments. Pyrene was used as an example of the PAHs at different concentrations. Representative soil samples were collected and contaminated by pyrene at three levels of concentrations: C1 (1.8 mg/kg), C2 (150 mg/kg), and C3 (300mg/kg). The experiments were conducted for 86 days. The pyrene removal from the contaminated soils was higher in most of the planted soil, compared with unplanted soil (controls) at different concentrations of the contaminants. In addition, the results of this study showed that sunflower (Helianthus annuus) were able to accumulate the tested pyrene in its tissues, and this accumulation was increased with the decrease in the contaminant concentrations in the soil. In addition, sunflower (Helianthus annuus) accumulated more amounts of pyrene in its aboveground parts (shoot and disc), compared with underground part (root). The results of this study imply that using sunflower (Helianthus annuus) in the phytoremediation process is an effective technique to remediate the contaminated soil with pyrene without causing any plant toxicity.

Keywords: *Pyrene, Phytoremediation,Sunflower, Contaminant, Helianthus annuus, Removal*

1. Introduction

Polycyclic aromatic hydrocarbons (PAHs) are organic compounds that have toxic effects on organisms. They can cause carcinogenic and mutagenic effects (e.g. Armstrong et al., 2004). The primary source of PAHs is the incomplete combustion of organic materials such as coal and oil as well as vehicular emissions and the indiscriminate disposal of refined petroleum products and used batteries (e.g., Imarhiagbe and Obayagbona, 2019).

PAHs are not synthesized chemically for industrial purposes. However, there are a few commercial uses for some chemicals of the PAHs such as pyrene. Pyrene is used in the manufacturing of pigments (Kaminski et al., 2008). Pyrene, $C_{16}H_{10}$ (four fused rings), is one of the PAHs that has recently gained attention due to its high toxicity, presence in all environmental ecosystems, high persistence, and resistance to biodegradation (Gabriele et al., 2021; Kim et al., 2019; Offiong et al., 2019; Sushkova et al., 2019; Zhang et al., 2018; Wang et al., 2012). Moreover, pyrene was selected among the 16 EPA-priority PAHs as a model compound based on its intermediate toxicity, hydrophobicity, and environmental persistence. Furthermore, pyrene represents the dominant PAH produced by the incomplete combustion of oil and oil byproducts (Kanaly and Harayama, 2000), and is frequently found in soil (Su et al., 2008) (Figure 1).

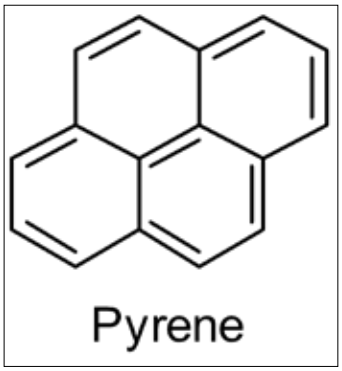

Figure 1. Structure of US-EPA Pyrene

Soil is considered similar to a sink reservoir for the presence of many atmospheric pollutants.Pyrenecontamination of soil occurs naturally because of the incomplete combustion of organic materials such as fossil fuels and vegetation. Moreover, pyrene is often monitored as an indicator of the amounts of PAHs in contaminated soils and sediments (Liu et al., 2020a, 2020b). Therefore, it is important to use technology that can remediate this pollutant from the soil. One of the important technologies is phytoremediation. Several studies showed that phytoremediation is an effective, sustainable, and reliable technique for the remediation of pyrene-contaminated soil and other toxic metals (Gabriele et al., 2021; (Omoregie and Ikhajiagbe, 2021). This technology utilizes plants to remove, stabilize, or reduce the toxicity

* Corresponding author e-mail: kmashal@hu.edu.jo

of the pollutants or contaminants in the soil, groundwater, or other polluted media (USEPA, 2000; Ogeleka and Omoregie, 2022). However, phytoremediation is applied as a final step after other treatments in case of high levels of contamination and is an effective strategy used alone when the concentration of contaminants is low (Jones, 1991). One example of promising plants that could be used in this matter is sunflower (Helianthus annuus). Sunflowers are short-season plants that belong to the family Asteraceae, and there are more than 70 known species around the world. It originally comes from the temperate climate of North America (temperatures around 20- 25 °C) (Adeleke and Babalola 2020).

This plant has valuable benefits. Its growing season is relatively short. It has a large flower with a single stalk and differs from the wild sunflower, which is smaller and has multiple branches (Aboki et al., 2012). Many studies use sunflower (Helianthus annuus) to accumulate different contaminants because of its properties of rapid growth and production of large volumes of biomass (Martins et al., 2014).

A comparative greenhouse experiment was conducted between different plant families to remediate contaminated soil with aged polycyclic aromatic hydrocarbons (PAHs) by Olson et al. (2007). It showed that the largest populations of polycyclic aromatic hydrocarbons (PAHs) degraders were contained in the soil, planted with sunflower (Helianthus annus). Moreover, the results showed that sunflower (Helianthus annuus) was effective in stimulating PAH removal, and it may be a promising species in the remediation processes for the contaminated soil (Olson et al., 2007).

The accumulation of polycyclic aromatic hydrocarbons (PAHs) and polychlorinated biphenyls (PCBs) uptake by sunflower, willow, maize, and poplar in contaminated urban soil in a field experiment was studied (Kacálková and Tlustoš) (2011). They found that a higher concentration of polycyclic aromatic hydrocarbons was accumulated in sunflowers more than in maize. In addition, they observed that the highest accumulation levels of pyrene and phenanthrene were found in plants grown in soil with lower concentrations of pyrene and phenanthrene (Kacálková and Tlustoš, 2011). Another greenhouse experiment was conducted by Tejeda-Agredano and colleagues in 2013 to ascertain if the germination and development of sunflower (Helianthus annuus) plants can promote bio-accessibility and biodegradation of polycyclic aromatic hydrocarbons in the contaminated soil. The same study also explored the effects of sunflower (Helianthus annuus) planting on the removal of six polycyclic aromatic hydrocarbons (fluorene, phenanthrene, anthracene, fluoranthene, pyrene, and chrysene) in the contaminated soil. The results showed that planting sunflowers (Helianthus annuus) had a promoting effect on the removal of five contaminants (fluorene, anthracene, fluoranthene, pyrene, and chrysene) which decreased significantly from the soil in comparison with the unplanted controls. Nevertheless, according to phenanthrene, there was not any significant effect on the removal of this contaminant (Tejeda-Agredano et al., 2013).

Martins, Liduino, Oliveira, and Sérvulo (2014) studied the potential of three cultivars of sunflower (Helianthus annuus) plants to remediate multi-contaminated soil by hydrocarbons and heavy metals. They conducted another greenhouse experiment. Results indicated that the sunflower (Helianthus annuus) cultivars were able to remove Benzo] a[pyrene that is a high molecular weight polycyclic aromatic hydrocarbon from the contaminated soil (Martins et al., 2014).

In Jordan, there are many sources of polycyclic aromatic hydrocarbons (PAHs) that might affect directly or indirectly the health of plants as well as human beings, such as the Jordan petroleum refinery, Al-Hussein thermal power stations, traffic emissions, accidents (such as oil spills), and industrial areas (e.g. All these resources led to an increase in the probability of soil contamination by polycyclic aromatic hydrocarbons (PAHs). Therefore, the main objective of this study is to evaluate the potential of sunflower (Helianthus annuus) to remediate contaminated soil with three different concentrations of pyrene as an example of the PAHs. Other objectives are to study the accumulation of pyrene in the three parts of the sunflower plant (root, shoot, and disc) and to compare sunflower uptake of pyrene.

2. Materials and Methods

2.1. Soil physiochemical analysis

A representative uncontaminated topsoil samples (0-20 cm) were used in this study. This soil is usually cultivated with seasonal crops. The soil samples were air dried at room temperature, sieved with 2 mm mesh, and then subjected to several chemical and physical analyses for the basic soil parameters such as soil texture, past pH, paste electrical conductivity (EC), organic matter content (Black-Wakley method), and the concentration of the pyrene. The concentration of pyrene in soil and plant samples was determined according to Touraud et al., (1998) and Li et al. (2010).

2.2 Phytoremediation experiments

The experiment was performed by adding five kilograms in total of soil to each pot and mixing the contaminants with the upper layer of the soil. In detail, the used pots were bottom-sealed to prevent contaminants from leaching out of the soil. In each pot, 4.5 kg of the above-described soil was spiked with three concentrations of pyrene C1 (1.8 mg/kg), C2 (150 mg/kg), and C3 (300 mg/kg), mixed with the upper layer of the soil, three seeds of sunflower (Helianthus annuus) were sown directly in the contaminated soil and finally covered by 0.5 kg of soil. Locally cultivated sunflower (Helianthus annuus) in Jordan was used in this experiment, as it was adapted to the environmental conditions in Jordan. Furthermore, it doesn't need a lot of care. In addition, sunflower (Helianthus annuus) is considered a drought-tolerant plant that doesn't need a large amount of water.

The experiment was done in three replicates for each treatment. There was one control soil containing the original and the added contaminants, which will not be cultivated with any plant taking into consideration the independent variables like wind and temperature. The experiment was conducted for 86 days in two phases. The first phase was

conducted in an open area because of the high temperature during the summer season, and the second phase was conducted in a plastic house because there was an expected drop in the temperature.

Seeds began to germinate, and seedlings emerged. During this period, the soil was kept moist to prevent hard crust formation, which might affect seed germination. About ten days after the end of the germination stage, the seedlings were thinned to keep just one seedling in each pot. The vegetative growth stage lasted much time in comparison with other stages; it lasted about forty days. During this stage, plants were irrigated carefully about one inch every three days. NPK fertilizer with micronutrients was added right at the beginning of this stage to maintain good health for the plants. After harvesting, plants were cut into the main parts (root, shoot, and disc). Fresh plant samples were washed through tap and distilled water to remove soil particles and dust completely from plant parts. Fresh weight was measured for each part of the plants, and the length of roots and shoots was measured. Air drying at room temperature in the laboratory of the faculty of Natural Resources and Environment was applied for all plants and soil samples until getting a constant weight. After drying, the dry weight for all plant samples was determined.

JMP version (8) statistical software was used to analyze the resulting data for all tested parameters. The statistical analyses included descriptive analysis using distribution command (e.g. measures of central tendency and dispersion), and comparison between means using Tukey Kramer Test (HSD) that is based on least significant difference testing at 95% confidence level.

3. Results and Discussion

3.1. Pyrene removal and uptake from the contaminated soil

The results of physiochemical properties of soil samples are presented in Table 1. The particle size distribution (42.37% sand, 37.45% silt, and 20.18% clay) indicated that the soil is loam. The pH of the soil is moderately alkaline (8.11), non-saline soil (EC< 4ds/m), moderately organic matter (6.14%), and 0.2 mg/kg of pyrene.

Table 1. Physiochemical properties of the studied soil samples

Parameter	Unit	value
Sand	%	42.37
Silt	%	37.45
Clay	%	20.18
Texture	-	Loam
pH	-	8.11
Electrical conductivity (EC)	dS/m	0.893
Organic matter content	%	6.14
Pyrene	mg/kg	0.2

After 86 days, the pyrene concentration in the non-cultivated, pyrene-spiked control soil decreased by 8.67%, 24.78%, and 39.71% for C1, C2, and C3 respectively as compared to the initial concentration (Table 2). This value was considered as the dissipation of pyrene in soil due to evaporation and degradation over the experimental period. There is pyrene removal from the unplanted control treatments, which likely refers to the microorganisms' activity in the soil (Olson et al., 2007). Furthermorepyrene is a volatile organic compound (VOC) and the area of evaporation is larger in bared soil (control) than in planted soil. Pyrene has a vapor pressure of 6.010-4 Pa (Mackay et al., 1992). These results are supported by several studies reported in literature. In a study by Liste and Alexander (2000), which investigated the capability of nine plant species to promote the degradation of pyrene in soil, it was found that higher pyrene was degraded in cultivated soil compared to non-cultivated soil. Moreover, Venkata et al., (2006) found a faster pyrene dissipation in the rhizosphere of several plants than in the bulk soil.

Table 2. Pyrene removal from the contaminated soil

Treatment	Initial (mg)	removal percent (%)
C 1	1.8	28.71^{a}
Control C1	1.8	8.67^{a}
LSD	-	25.78
C2	150	50.06^{a}
Control C2	150	24.78^{b}
LSD	-	19.03
C3	300	58.86^{a}
Control C3	300	39.71^{a}
LSD	-	26.8

*Values of C1, C2 and C3 are means of triplicate measurements, values followed by the same letter are not significantly different at ($p<0.05$).

The pyrene concentrations in soils cultivated with sunflower (Helianthus annuus) decreased respectively by 28.71, 50.07, and 58.86% with respect to the initial values. This decrease was not statistically significant except for C2. This result was agreed with Besalatpour et al. (2010) who found that sunflower (Helianthus annus) hadn't any significant effect on the reduction of the total petroleum hydrocarbons (TPHs) in the contaminated soil. Planting contaminated soil with sunflower (Helianthus annuus) stimulates pyrene degradation through root exudates, which have a clear impact on the development of PAHs degraders' populations (Ortega-Calvo et al., 2017; Olson et al., 2007).

Pyrene uptake by different plant parts (root, shoot, and disc) and by the whole plant are shown in Table 3. During the growth phase, plants can accumulate contaminants in roots, stems, and leaves, and pyrene is eventually removed by harvesting the plant when the treatment is terminated (Mahar et al., 2016).

Table 3. Pyrene uptake by plant parts (root, shoot and disc) and by the whole plant.

Treatment (mg/kg)	Root uptake (%)	Shoot uptake (%)	Disc uptake (%)	Plant uptake (%)
C 1	0.5^{b}	12.1^{b}	7.6^{b}	20.27^{a}
C 2	0.027^{ab}	1.88^{ab}	1.65^{a}	3.56^{a}
C 3	0.028^{a}	0.86^{a}	1.23^{a}	2.72^{a}
LSD	0.29	17.95	7.31	17.63

*Values of C1, C2 and C3 are means of triplicate measurements, values followed by the same letter are not significantly different at ($p<0.05$).

The results showed that roots, shoots, and discs significantly uptake more amount of pyrene at C1 treatment compared with other treatments (Table 3). There were no significant differences between the three treatments in pyrene uptake by the plant, taking into consideration the total amount of pyrene in the soil. However, the results showed that the increase in concentrations of pyrene in the soil leads to a significant decrease in the uptake percentage by different plant parts between treatments. The obtained results concur with Kacálková's and Tlustoš's (2011) study findings where the pyrene PAH uptake by the plant was significantly low when cultivated in soil contaminated with high PAH concentrations.

The extent to which an organic pollutant enters plant roots from contaminated soils depends on the physicochemical characteristics of the compounds including contaminant concentrations in the soil, octanol/water partition coefficient (log Kow), and other factors such as organic carbon content of the soil and plant species (Nwoko, 2010). Hydrophobic compounds with log Kow > 3.0 are bound so strongly to the surface of roots that cannot be easily translocated within the plant. Pyrene log Kow is 5.18, Mackay et al., 1992. This could explain the insignificance of pyrene accumulation in tested plant shoots and roots.

3.2 Plant characteristics at different concentrations of the contaminants

To observe the effect of pyrene uptake on plant growth, the fresh and dry weights of plant parts (root, shoot, and disc) and shoot and root heights were measured at the end of the growth cycle. Fresh and dry weights of plant parts (root, shoot, and disc), after the phytoremediation test, are presented in Figure 2. Statistical analysis of the data showed that pyrene, at low concentration applied (C1), was generally non-toxic to the three plant parts. The C1 concentrations of pyrene had no significant ($p<0.05$) effect on the fresh and dry weights of the different plant parts. No severe plant growth inhibition was apparent during the growth period. While C2 and C3 have a significant effect ($p<0.05$) among fresh and dry weights of plants (Figure 2). The maximum root, shoot, and disc for both fresh and dry weights were found at (C1) treatment. The minimum root, shoot, and disc fresh weights were found at pyrene (C2) treatment (Figure 2). As the pyrene concentration increases in soil, the sorption by soil particles increases resulting in the prevention of pyrene uptake by plants (Olu-Owolabi et al., 2014). Increasing soil pyrene concentration has increased the sorption by soil particles and hindered pyrene uptake by plants. This can be attributed to the fact that when the transport of pyrene at the external soil surface and within the internal pores is equal, less transboundary movement of pyrene is allowed. However, as the concentration increases, the transboundary movement of pyrene resumes, and the adsorption is concentration-dependent (Olu-Owolabi et al., 2014). This explains why the C3 treatment showed higher root, shoot, and disc weight compared with C2.

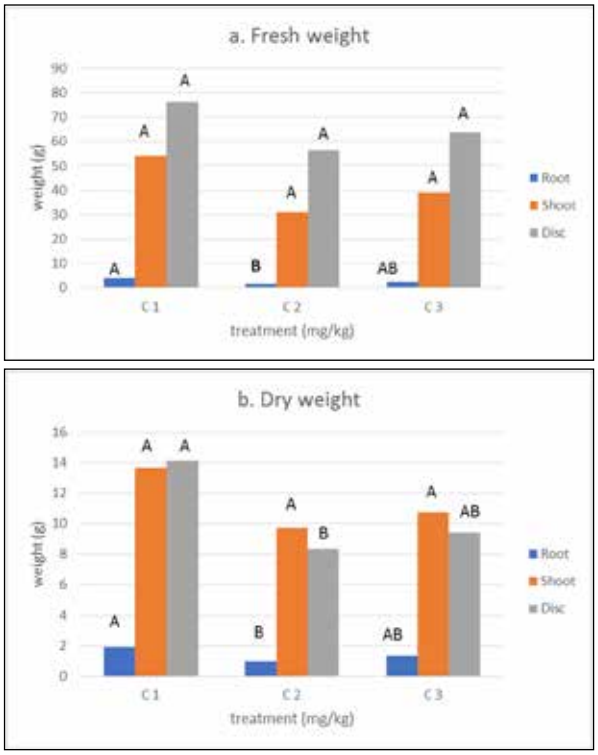

Figure 2. Weight (g) of plant parts (shoot, root and disc) after phytoremediation test fresh weight b. dry weight. (Values with the same letter are not significantly different at $p\leq0.05$ (LSD test).

However, statistical analysis of the obtained data showed that there are no significant ($p<0.05$) effects of the different concentrations of pyrene on the lengths of plant root and shoot (Figure 3). These results would imply that pyrene does not affect the development of sunflowers (Helianthus annuus) height. Same results were found in literature using L. perenne (D'Orazio et al., 2013), related this effect to the other factors associated with the plant itself and other soil factors.

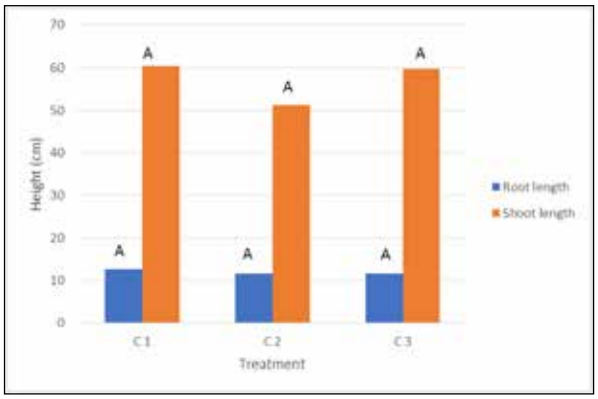

Figure 3. Shoot and root length (cm) after phytoremediation test of pyrene.
Values with the same letter are not significantly different at $p\leq0.05$ (LSD test).

The results showed that phytoremediation mechanism for all treatments include extraction, degradation, volatilization, and stabilization by plants as indicated by more than 50% removal for higher concentration of pyrene. Moreover, the results indicate that the removal of pyrene does not result in any toxicity for the used plant.

Comparing pyrene removal from soil and plant uptake (Figure 4), each point is the average of triplicate. For the 86-day phytoremediation trial, the amount of pyrene in the uncultivated, pyrene-spiked control soil decreased by 8.67%, 24.78%, and 39.71% respectively. The distribution of pyrene in the soil and plants is shown by these findings. The soil used to cultivate sunflowers (Helianthus annuus) reduced pyrene by 28.71%, 50.10%, and 58.86% respectively, when measured in comparison to the initial levels. While the percentage of removed plants was 20.30%, 3.60%, and 2.70% respectively. These results demonstrated that plant removal decreased as soil pyrene content increased whereas the opposite was true for soil removal.

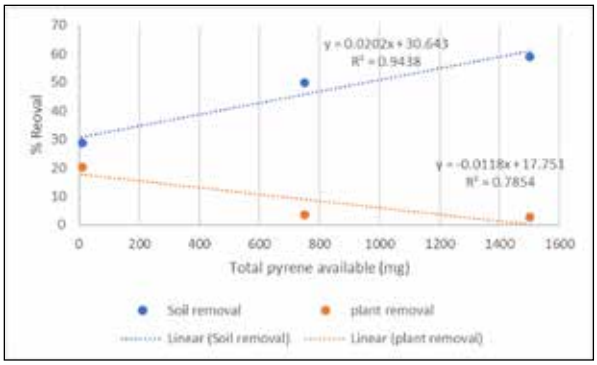

Figure 4. Total pyrene removal from spiked soil by soil and plant

These results (Figure 4) indicated that several factors play a major role in pyrene removal from soil. As the concentration of pyrene in soil increases, the effect of plant uptake is low, supporting that the pyrene removal is affected by other factors due to evaporation, degradation, and the presence of certain genera that are capable of using pyrene as energy and sole carbon source in the rhizosphere area and promote biodegradation of pyrene (Liu et al., 2013; Zeng et al., 2019; (Yang et al., 2021). Moreover, bioavailability plays a major role in plant uptake. Several factors affect the bioavailability such as aging or contamination. A study by Smith et al., 2011 showed that pyrene loss, through mechanisms not connected to plants, could more easily occur in freshly spiked soils. Presence of organic matter in high amounts (Table 1) more than 2% could play a role in limiting the bioavailability of pyrene for plants through adsorption. A study by Chekol et al., 2002 showed that under high soil organic matter (6.3%) conditions, adsorption, or covalent binding of pyrene to SOM are the dominant forces for pyrene retention in soil, limiting pyrene bioavailability for plants. Therefore, under the soil conditions of this study, sunflower (Helianthus annuus) with other soil factors showed a promising potential in promoting the phytoremediation of pyrene freshly added to the soil without any toxicity or any effect on plant growth. Moreover, the accumulation of pyrene in the aboveground parts helps remove pyrene by harvesting.

4. Conclusion

After 86 days of phytoremediation experiment, sunflower (Helianthus annuus) appears to be a promising process to remediate contaminated soil with the tested polycyclic aromatic hydrocarbon (pyrene). Pyrene removal from the contaminated soil was higher in the planted soil compared with unplanted soils at different concentrations of the contaminant. Sunflowers (Helianthus annuus) showed their ability to accumulate pyrene in their tissues, and this accumulation was increased with the decrease in the contaminant concentration in the soil without showing any toxicity. Therefore, plant cultivation on pyrene-contaminated soil appeared to play a significant role in ecosystem restoration by limiting the spread (erosion, leaching) of pyrene and restoring sites contaminated with pyrene. Thus, this practice represents an important tool for the control of pyrene migration in soil. Sunflower (Helianthus annuus) accumulated more amounts of pyrene in its aboveground parts (shoot and disc) compared with underground parts (roots).

Acknowledgment

The research team wishes to thank Hana Al-Nounah for her sampling and analytical work during all stages of this study.

Conflicts of Interest:

The authors declare no conflicts of interest.

References

Aboki, M. A., Mohammed M., Musa S. H., Zuru B. S., Aliyu H. M., Gero M., Alibi I. M., Inuwa B. (2012). Physicochemical and Anti-Microbial Properties of Sunflower (Helianthus aannus L.) Seed Oil. International Journal of Science and Technology 2:151-154.

Adeleke B.S., and Babalola O.O. (2020). Oilseed crop sunflower (Helianthus annuus) as a source of food: Nutritional and health benefits. Food Science and Nutrition. 8:4666-4684.

Armstrong B., Hutchinson E., Unwin J., Fletcher T. (2004). Lung cancer risk after exposure to polycyclic aromatic hydrocarbons: a review and meta-analysis. Environmental Health Perspective 112(9):970-8.

Besalatpour, A. A., Hajabbasi M. A., Khoshgoftarmanesh A. H.(2010). Reclamation of a Petroleum-Contaminated Calcareous Soil Using Phytostimulation. Soil and Sediment Contamination: An International Journal 19: 47-559.

Chekol, T., Vough, L.R., Chaney, R. (2002). Plant-Soil-Contaminant Specificity Affects Phytoremediation of Organic Contaminants. International Journal of Phytoremediation 4: 17–26.

D'Orazio, V., Ghanem A., Senesi N. (2013). Phytoremediation of Pyrene Contaminated Soils by Different Plant Species. Clean, Soil, Air, Water 41: 377–382.

Imarhiagbe, E. Obayagbona N. (2019). Polycyclic Aromatic Hydrocarbon, Physio-Chemical Properties, and Culturable Microbial Flora of Human Urine-Impacted Topsoils at Commercial Tricycle Parks Along Benin-Sapele Expressway, Benin City, Nigeria. Jordan Journal of Earth and Environmental Sciences 10 (3): 167-172.

Gabriele, I., Race M., Papirio S., Esposito G. (2021). Phytoremediation of pyrene-contaminated soils: A critical review of the key factors affecting the fate of pyrene. Journal of Environmental Management 293: 112805.

Jones, K.C. (1991). Organic Contaminants in the Environment. Elsevier Applied Science. New York, NY.

Kacálková, L., and P. Tlustoš. (2011).The uptake of persistent organic pollutants by plants. Central European Journal of Biology 6: 223-235.

Kaminski, N.E., Faubert Kaplan B.L., Holsapple M.P. (2008). 7th ed., in: Curtis D. Klaassen (Ed.), Casarett and Doull's Toxicology, the basic science of poisons, vol. 526, Mc-Graw Hill, Inc.

Kanaly, R. A., and Harayama S. (2000). Bioremediation of High-Molecular Weight Polycyclic Aromatic Hydrocarbons by Bacteria. Journal of Bacteriology 182: 2059–2067.

Kim, L., Jeon H.J., Kim Y.C.,Yang S.H., Choi H., Kim T.O., Lee S.E. (2019). Monitoring polycyclic aromatic hydrocarbon concentrations and distributions in rice paddy soils from Gyeonggi-do, Ulsan, and Pohang. Applied Biological Chemistry. https://doi. org/10.1186/s13765-019-0423-7.

Li, J., Shang X., Zhao Z., Tanguay R.L., Dong Q., Huang C. (2010). Polycyclic aromatic hydrocarbons in water, sediment, soil, and plants of the Aojiang River waterway in Wenzhou, China. Journal of Hazardous Materials, 173:75-81.

Liste ,H., and Alexander M. (2000). Plant-Promoted Pyrene Degradation in Soil. Chemosphere 40: 7–10.

Liu, J., Su H., Wei X., Xue J. (2020a). Progress in Bioremediation of Pyrene. Recent Innovations in Chemical Engineering (Formerly Recent Patents on Chemical Engineering). https://doi. org/10.2174/2405520412666191009104644.

Liu, S., Hou Y., Sun G. (2013). Synergistic degradation of pyrene and volatilization of arsenic by cocultures of bacteria and a fungus. Frontiers of Environmental Science and engineering. https:// doi.org/10.1007/s11783-012-0470-3.

Liu, X., Shen S., Zhang X., Chen X., Jin R., Li X. (2020b). Effect of enhancers on the phytoremediation of soils polluted by pyrene and Ni using Sudan grass (Sorghum sudanense (Piper) Stapf.). Environmental Science and Pollution Research. https:// doi. org/10.1007/s11356-020-09934-3.

Mahar, A., Wang, P., Ali, A., Awasthi, M.K., Lahori, A.H., Wang, Q. Li, R., Zhang, Z. 2016. Challenges and opportunities in the phytoremediation of heavy metals contaminated soils: A review. Ecotoxicology and Environmental Safety doi: 10.1016/j.ecoenv.2015.12.023.

Mackay, D., Shiu W.Y., May K.C.(1992). Illustrated Handbook of Physical-Chemical Properties and Environmental Fate for Organic Chemicals: Polynuclear Aromatic Hydrocarbons, Polychlorinated Dioxins, and Dibenzofurans, 1-597. Lewis Publishers, Chelsea, MI, USA.

Martins, C. D., Liduino V.S., Oliveira F.J., Servulo E.F. (2014). Phytoremediation of Soil Multi-Contaminated with Hydrocarbons and Heavy Metals Using Sunflowers. International Journal of Engineering & Technology, 14:1-8. https://doi.org/10 .1080/10934529.2018.1429726

Nwoko, C. O. (2010). Trends in Phytoremediation of Toxic Elemental and Organic Pollutants. African Journal of Biotechnology 9: 6010–6016.

Offiong, N.A.O., Inam E.J., Etuk H.S., Essien J.P. (2019). Current status and challenges of remediating petroleum-derived PAHs in soils: Nigeria as a case study for developing countries. Remediation. https://doi.org/10.1002/rem.21630.

Ogeleka, D. F., and Omoregie, G. O. (2022). Ecotoxicological Consequences and Hyper-accumulative Potentials of Beans (Phaseolus vulgaris) Exposed to Heavy Metals Spiked in Native Soils. Jordan Journal of Earth and Environmental Sciences 13 (2): 114-121.

Olson, P. E., Castro A., Joern M., Duteau N.M., Pilon-Smits E.A., Reardon K.F. (2007). Comparison of Plant Families in a Greenhouse Phytoremediation Study on an Aged Polycyclic Aromatic Hydrocarbon–Contaminated Soil. Journal of Environment Quality 36: 1461.

Olu-Owolabi B. I., Diagboya P. N., Adebowale K. O. (2014). Evaluation of pyrene sorptionedesorption on tropical soils. Journal of Environmental Management. https://doi.org/10.1016/j. jenvman.2014.01.048.

Omoregie, G., and Ikhajiagbe, B. 2021. Differential Morphological Growth Responses of Chromolaena odorata under Heavy Metal Influence. Jordan Journal of Earth and Environmental Sciences 12: 50-61

Ortega-Calvo, J. J., Posada-Baquero R., Garcia J. L., Cantos M. (2017). Bioavailability of Polycyclic Aromatic Hydrocarbons in Soil as Affected by Microorganisms and Plants. In Soil Biological Communities and Ecosystem Resilience (pp. 305-319). Springer, Cham.

Smith, M.J., Flowers T.H., Duncan H.J., Saito H. (2011). Study of PAH dissipation and phytoremediation in soils: comparing freshly spiked with weathered soil from a former coking works. Journal of Hazardous Material 192: 1219-25. https://doi. org/10.1016/j. jhazmat.2011.06.033.

Su, Y., Yang X., Chiou C. T. (2008). Effect of Rhizosphere on Soil Microbial Community and in Situ Pyrene Biodegradation. Frontiers of Environmental Science and Engineering 2: 468–474.

Sushkova, S., Minkina T., Deryabkina I., Rajput V., Antonenko E., Nazarenko O., Yadav B. K., Hakki E., Mohan D. (2019). Environmental pollution of soil with PAHs in energy producing plants zone. Science of the Total Environment. https://doi.org/ 10.1016/j.scitotenv.2018.11.080.

Tejeda-Agredano, M., Gallego S., Vila J., Grifoll M., Ortega-Calvo J., Cantos M. (2013). Influence of the sunflower rhizosphere on the biodegradation of PAHs in soil. Soil Biology and Biochemistry 57: 830-840.

Touraud, E., Crone M., Thomas O. (1998). Rapid diagnosis of polycyclic aromatic hydrocarbons (PAH) in contaminated soils with the use of ultraviolet detection. Field Analytical Chemistry & Technology 2: 221-229.

United States Environmental Protection Agency (USEPA). (2000). Introduction to Phytoremediation. EPA 600/R-99/107, U.S. Environmental Protection Agency, Office of Research and Development, Cincinnati, OH.

Venkata, M. S., Takuro K., Takeru O., Robert A. K., Yoshihisa S. (2006). Bioremediation Technologies for Treatment of PAH-Contaminated Soil and Strategies to Enhance Process Efficiency, Rev. Environmental science Biotechnology 5: 347–374.

Wang, M.C., Chen Y. T., Chen S.H., Chang Chien S.W., Sunkara S.V. (2012). Phytoremediation of pyrene contaminated soils amended with compost and planted with ryegrass and alfalfa. Chemosphere 87: 217-225.

Yang, J., Gu Y., Chen Z., Song Y., Sun F., Liu J., Waigi M. G.(2021). Colonization and performance of a pyrene-degrading bacterium Mycolicibacterium sp. Pyr9 on root surfaces of white clover. Chemosphere. https://doi.org/10.1016/j. chemosphere.2020.127918.

Zeng, J., Zhu Q., Li Y., Dai Y., Wu Y., Sun Y., Miu L., Chen H., Lin X. (2019). Isolation of diverse pyrene-degrading bacteria via introducing readily utilized phenanthrene. Chemosphere. https:// doi.org/10.1016/j.chemosphere.2019.01.189.

Zhang, Y., Virjamo V., Du W., Yin Y., Nissinen K., Nybakken L., Guo H., Julkunen-Tiitto R. (2018). Effects of soil pyrene contamination on growth and phenolics in Norway spruce (Picea abies) are modified by elevated temperature and CO2. Environmental Science and Pollution Research 25:12788-12799.

JJEES

JJEES (2024) 15 (2): 129-135
ISSN 1995-6681

Jordan Journal of Earth and Environmental Sciences

Experimental studies of Physico-hydrodynamic parameters of Carbon Dioxide Application

Alexander V. Chibisov[1], Alexander P. Chizhov[1], Yousef A. Abusal[*2], Shamil Kh. Sultanov[1], Renat R. Gazizov[2]

[1]Department of Geology and Exploration of Oil and Gas Fields, Ufa State Petroleum Technological University Kosmonavtov str., 1, Ufa, 450064, Russian Federation

[2]Department of Oil and Gas Well Drilling, Ufa State Petroleum Technological University Kosmonavtov str., 1, Ufa, 450064, Russian Federation

Received June 13, 2023; Accepted November 13, 2023

Abstract

The article presents new results of laboratory studies, along with a summary of previously obtained ones. An analysis of the development of reserves in the experimental area was carried out with recommendations for improving the efficiency of its oil recovery processes in the amount of 10-30% of the pore volume of the experimental area. New conditions for injection with a limited supply of carbon dioxide are considered. The results of oil recovery modeling, using CO_2 and water rims, are presented. The increase in oil recovery for reservoirs D_1 and D_2 was determined, and a forecast was made for the value of additional oil production per ton of carbon dioxide.

Keywords: *Core, Efficiency increase, Oil displacement, Injection, Carbon dioxide, Oil recovery.*

1. Introduction

This work was carried out in accordance with the research schedule and is an addition to the theoretical study of the injection of carbon dioxide into the productive strata of depleted oil fields. The paper clarifies the geological characteristics of the experimental area and sets out main issues, the solution of which depends on the volume of CO_2 supply.

A preliminary assessment of the effectiveness of the use of CO_2 in one- production well is given. The results of testing the technology for washing the sediment of asphalt-resinous substances in injection wells are presented.

Recommendations are given for the development and restoration of injection wells. The results obtained and these recommendations can be used for CO_2 injection (Andreev et al 2023, ChizhovA et al 2021, Rabaev et al. 2021).

2. Materials and methods

The substantiation of the design provisions of the pilot works involves laboratory studies to determine the oil displacement coefficients for water, carbonated water, carbon dioxide, and the effect of CO_2 on the physical properties of oil, water, and host rocks.

To test the conditions of the experimental site of the oil field, a set of laboratory studies has been carried out to study the solubility of CO_2 in oil, the effect of carbon dioxide on the composition and gas factor of oil, its distribution over heterogeneous layers during filtration.

For the preparation of porous media, cores of Devonian deposits were used, taken in well Nos. as Devonian productive objects. Layer D_1 is represented by 47 samples of core material, layer D_2-57 samples. Oil saturation was determined from core samples from wells Nos. 1070 and 1173.

The parameters of the core material samples are shown in Table 1. A comparison of the weighted average values of the parameters of the samples showed that reservoir D_1 has better reservoir properties than reservoir D_2. The filtration properties of the D_1 formation samples are 1.8 times higher, the porosity is 8.8% higher, and the carbonate and clay contents are 1.3 and 1.4 times lower respectively (Figure 1).

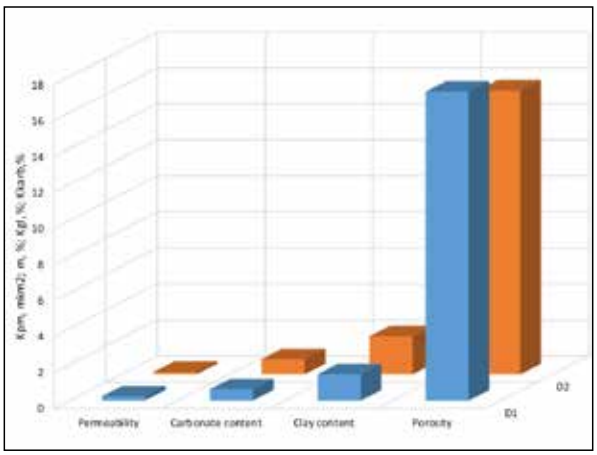

Figure 1. Thickness-weighted average values of the main parameters of sandstone samples

* Corresponding author e-mail: yousef-abusal@mail.ru

Table 1. Thickness-weighted parameters of the core material of the polygon object

Wells	Definitions	Parameters				
	Layer	Permeability, $\times10^{-12}$ m^2	Porosity, %	Carbonate content, %	Clay content, %	Oil saturation, %
733	Quantity	7	7	7	7	-
	D_1	0,144	15,7	1,24	1,87	-
880	Quantity	2	2	2	2	-
	D_1	0,334	18,4	0,8	1,6	-
	Quantity	28	28	28	28	-
	D_2	0,131	16,3	1	2,3	-
1070	Quantity	25	25	25	25	25
	D_2	0,149	15,5	0,6	2	36,9
1173	Quantity	26	29	28	29	28
	D_1	0,238	17,2	0,37	1,3	36,4
	Quantity	4	4	4	4	3
	D_2	0,05	14,2	1,64	1,7	29

Table 2. Average values of the parameters of the sandstone samples of the deposit before and after exposure to carbon dioxide

Permeability interval, $\times10^{-12}$ m^2	Initial values				After exposure to CO_2			
	Kpr, $\times10^{-12}$ m^2	m, %	Kkarb, %	Kgl, %	Kpr, $\times10^{-12}$ m^2	m, %	Kkarb, %	Kgl, %
0.01-0.05	0	15.67	1.3	2.38	0.051	15.92	1.23	1.05
0.05-0.10	0.1	15.75	0.67	1.8	0.104	16.16	0.62	1.18
0.10-0.20	0.1	16.51	0.91	2.02	0.158	16.73	0.67	0.63
0.20-0.30	0.2	17	0.73	2.07	0.256	17.28	0.58	1.12
0.30-0.40	0.4	17.63	0.59	1.85	0.393	18.1	0.51	1.03
0.40-0.50	0.5	17.65	0.67	1.62	0.528	18	0.51	1.29
0.50-0.60	0.5	19.1	0.3	1.07	0.577	19.4	-	-
0.80-1.00	0.9	20.9	0.56	0.73	1.087	21.4	0.4	0.62

Notes: Kpr – permeability; m – porosity; Kkarb - carbonate content; Kgl - clay content.

Under the experimental conditions (pressure 11 MPa, temperature 313 °K), the oil had a viscosity of 7.86 mPa×s, a density of 0.848 g/cm^3, a viscosity of water of 0.856 mPa×s, and a density of 1.0614 g/cm^3 (Chizhov et al 2020, Mousa et al 2012, Qahir et al 2014). The solubility of CO_2 in water and oil under reservoir conditions was experimentally determined (Table 3, Figure 2), as well as the change in the gas factor of oil saturated with CO_2 (Table 4, Figure 3).

Table 3. Solubility of CO_2 in injected water

Pressure, Mpa	4	6	8	10	12	14	16	18
CO_2 concentration in water, % by weight	2.3	3.3	3.8	4	4.1	4.2	4.3	4.4

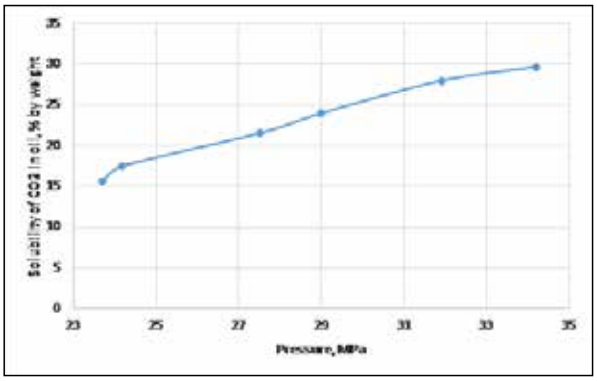

Figure 2. Solubility of carbon dioxide in oil

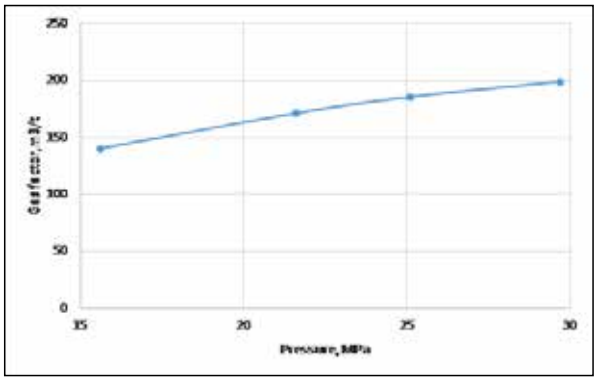

Figure 3. GOR of oil saturated with CO_2

Table 4. Change in GOR of oil saturated with carbon dioxide under reservoir conditions

GOR*, m^3/t/share.unit	37/1	72.40/1.89	91.50/2.38	143.90/3.75
CO_2 concentration in oil, % wt.	0	5	10	20
* Pressure - 18.5 MPa, temperature - 313°K				

Dissolving in oil, carbon dioxide significantly reduces its viscosity and increases saturation pressure. The distribution coefficients of CO_2 between water and oil and oil and the CO_2 phase, were determined under dynamic conditions in free volume at a pressure of 11 MPa and a temperature of 313 °K. The average value of the distribution coefficient between oil and water is 1.83, and it is between oil and CO_2 phase is 4.28.

3. Results and Discussion

The displacement of oil with water, carbonized water, and carbon dioxide was carried out at a pressure of 11 MPa and a temperature of 313 °K. The results of oil displacement by water (Table 5, Figure 4) show that in the permeability range of 0.02-0.05×10^{-12} m^2, the displacement coefficient increases from 0.665 to 0.699, and in the permeability range of 0.05 - 0.25, the oil displacement coefficient by water is 0.697± 0.043.

The results of experiments on oil displacement by carbon dioxide show that the alternating injection of portions of CO_2 and water does not reduce the efficiency of the method.

Table 5. Coefficient of oil displacement by water from core sandstones

Number models	Length of reservoir model, m	Permeability, ×10^{-12} m^2	Porosity,%	Bound water,%	Water flow rate, m/year
1	0.411	0.004	14	10	66
2	0.569	0.023	16.8	10	189
3	0.55	0.025	17.2	9.5	30
4	0.428	0.034	15.2	9.8	106
5	0.408	0.052	16.4	11.1	293
6	0.573	0.054	18.4	8.6	253
7	0.408	0.059	16.3	10.4	294
8	0.402	0.064	16.6	9.2	145
9	0.402	0.069	16.1	10	298
10	0.573	0.108	18.5	9.7	252
11	0.589	0.12	16.4	9.6	282
12	0.429	0.124	16.2	9.2	332
13	0.589	0.142	16.6	9.8	279
14	0.588	0.143	16.9	9.2	265
15	0.583	0.146	17	9.8	322
16	0.42	0.198	18	10	267
17	0.423	0.206	17.8	9.7	270
18	0.421	0.216	18	9.4	270
19	0.423	0.225	17.7	9.6	270
20	0.42	0.227	17.9	9.6	267

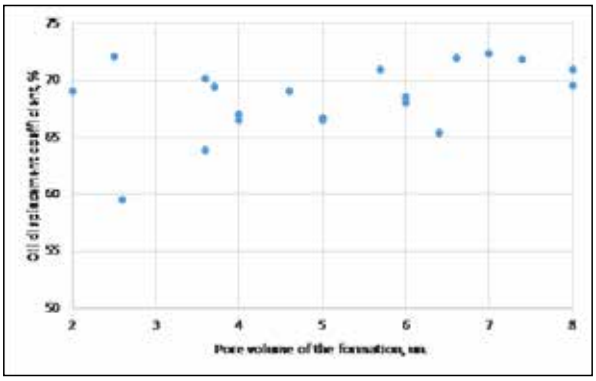

Figure 4. Oil displacement values for different CO2 injection volumes

At the next stage of research, the distribution of carbon dioxide over heterogeneous reservoirs was determined during the filtration process. According to (Chizhov et al 2020, Chizhov et al 2019, Andreev et al 2019), the main technological parameters of CO_2 and water injection were the total volume of the CO_2 slug (Vot) that is 15% Vn, and the ratio of the volumes of injected water and CO_2, (λ) is 3:2. In subsequent experiments, the values Vot and λ, accepted in (Chizhov et al 2020, Chizhov et al 2019), were confirmed. The minimum number of portions (n) into which the CO_2 slug must be divided is also determined in order to prevent premature breakthrough of the reagent into production wells. Experiments to determine the minimum required number of CO_2 portions were carried out on models of non-communicating, heterogeneous reservoirs with a common input and separate withdrawal of fluids. Considering that the change in such parameters as oil saturation, composition, and properties of residual oil cannot be controlled during the studies. All experiments were carried out on water-saturated reservoir models (Table 6).

Table 6. Characterization of reservoir models

Model number	Length, $\times10^{-2}$ m		Permeability, $\times10^{-12}$ m^2		Permeability ratio, units
1	58	54.8	0.144	0.018	7.8
2	52	54.8	0.158	0.026	6
3	54.8	54.8	0.133	0.039	3.41
4*	101.8	54.8	5.001	0.039	128.2

*Note: Model 4 was made for the physical modeling of phase permeabilities, which can be an order of magnitude or greater than the ratio of reservoir permeabilities

On these reservoir models, several series of experiments were carried out at a pressure of 10.0 MPa, a temperature of 299.5 °K and 313 °K, and an average velocity of fluids in the pore space of 201 m/year. The volume of the CO_2 slug was 12 and 16% of the pore volume of the reservoir model samples. Each series consisted of four experiments, during which the injected CO_2 slug was divided into 5, 10, 20, or 40 portions. In each series of experiments, the ratio of the volumes of water and CO_2 were constant. A series of experiments was carried out for at ratios of water and CO_2 equal to 1, 1.5, 2, and 3. Since the reservoir temperature of the polygon is 313 °K and exceeds the critical temperature of CO_2 (304.1 °K), two series of experiments were carried out to determine the degree of influence of the state of aggregation of carbon dioxide on its distribution in heterogeneous reservoirs. The experiments were carried out at temperatures of 299.5 °K and 313 °K. The results of the experiments are shown in Tables 7 and 8.

Table 7. Influence of the state of aggregation of carbon dioxide on the distribution parameters in reservoirs with different permeabilities

Temperature, °K	Number of servings, units				
	1	5	10	20	40
299.5	3.42	3.05	2.77	2.68	2.54
313	3.6	3.22	3.11	2.96	2.76

The distribution parameter (R) is a dimensionless value, which is the ratio of the amount of fluid entering the high-permeability reservoir (Qv) to the amount of fluid entering the low-permeability reservoir (Qn).

Table 8. Distribution parameters of carbon dioxide rims with a size of 12% of the void space of the reservoir at various values of the ratios of CO_2 to water and the number of portions

The ratio of CO_2 to water (λ), units	Number of servings, units			
	5	10	20	40
3	2,24	2,39	1,4	1,24
2	1,53	1,64	1,49	-
1,5	1,61	1,51	1,42	1,37
1	1,63	1,9	1,59	1,59

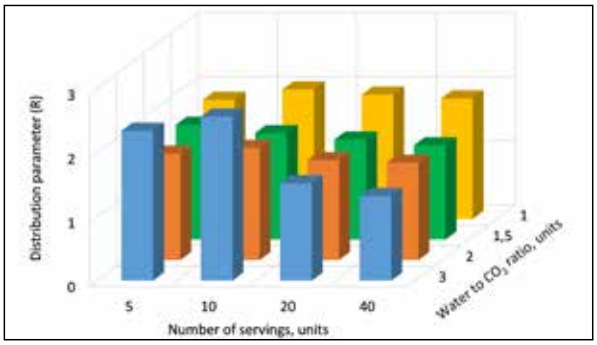

Figure 5. Distribution parameters of carbon dioxide fringes with a size of 16% of the pore space at different values of the ratio of CO_2, water, and the number of servings

Experiments have shown that the influence of the state of aggregation of carbon dioxide on the parameters of its distribution over heterogeneous layers during filtration is very insignificant. The nature of the distribution of CO_2 in heterogeneous reservoirs with the size of the rims of both 12% and 16% of the volume of the void space of the polygon object is similar, and the flow of the reagent into the low-permeability reservoir is facilitated by an increase in CO_2 and the number of rims. But this relationship is ambiguous. Thus, when the number of portions is less than 20, an increase in ratios of 1.5-3 entails a sharp decrease in the supply of carbon dioxide to a low-permeability formation.

Geological and hydrodynamic modeling of oil recovery using CO_2 rims in the pilot area. In the experimental area, the deposits coincide in plan and are separated from each other by D_1 and D_2 layers (Andreev et al 2019, Chizhov et al 2020, Chizhov et al 2020). Formation D_2 is underlain by bottom water over most of the area of the pilot area. Heterogeneity in reservoir permeability obeys a logarithmically normal distribution law with a variation coefficient of 0.79 and an average permeability value of 0.15×10^{-12} m^2. Data on the geological structure of the reservoirs, the type of reservoirs, and their heterogeneities are the basis of their geological and physical models. Their characteristics are shown in Figure 6.

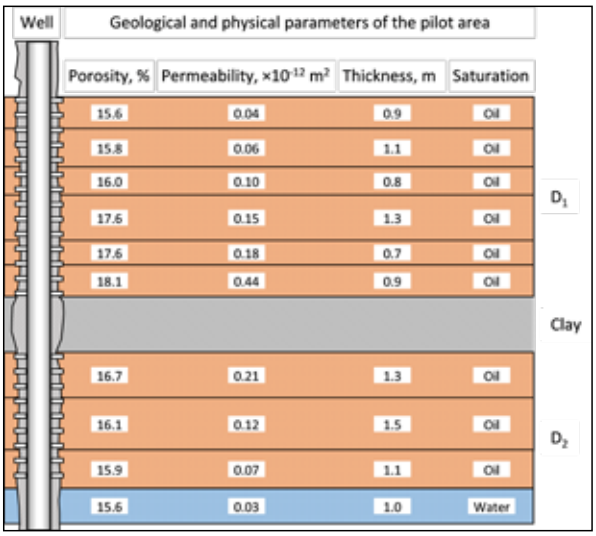

Figure 6. Average values of the parameters of the pilot area used in the simulation of oil displacement from the reservoirs of group D.

The thickness-weighted average values of permeability and porosity for the D_1 formation are 0.24×10^{-12} m^2 and 17.6%, and for the D_2 formation 0.133×10^{-12} m^2 and 15.77% respectively (Figures 6-8).

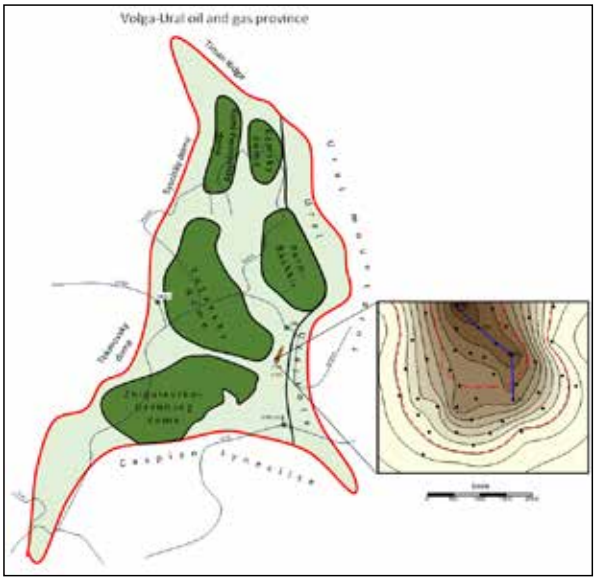

Figure 7. The location of the experimental site on the tectonic map of the Volga-Ural oil and gas province. The blue polygon indicates the geological profile along the line of wells Nos. 365, 259, 412, and 63.

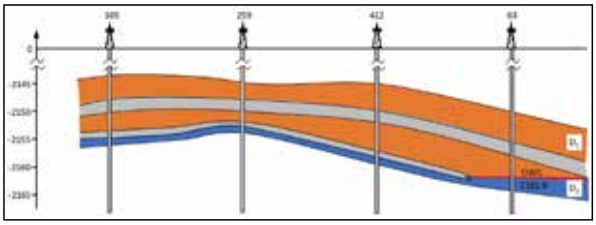

Figure 8. Geological section of the pilot area along the line of wells Nos. 365, 259, 412, and 63.

The calculation of technological indicators was carried out using a quasi-one-dimensional numerical model of the process of displacement of oil by CO_2. It also uses water in layered formations for a characteristic element of the formation (Andreev et al 2019, Chizhov et al 2020, Andreev et al 2020, Efimov et al 2021) and a special program for summing the indicators for the entire development object. The initial data for calculations are given in Table 8, and the additional data are as follows: At the existing formation pressure of 18 MPa and temperature of 40°C, the density and viscosity of the injected CO_2 and water are 0.79, 1.06 g/cm^3 and 0.076, 0.86 mPa×s respectively. The equilibrium values of the mass fraction of CO_2 in oil and water are 0.246 and 0.044. As a result of processing laboratory experiments on the displacement of oil by water and carbon dioxide, the following dependences of the relative permeability of the phases were established (Yamaletdinova et al 2020 , Andreev et al 2020,Chizhovet al 2019):

- for oil

$$K_{po} = \left(\frac{S_o^* - S_{or}}{1 - S_{or}}\right)^3 \times \left[1 + \left(3.58 \times S_g + 0.52\right) \times S_w\right], S_o^* > S_{or},$$

- for water

$$K_{pw} = \left(\frac{S_w - S_{wr}}{1 - S_{wr}}\right)^2 \times 0.32,$$

- for gas

$$K_{pg} = \left(\frac{S_g - S_{gr}}{1 - S_{gr}}\right)^{3.5} \times \left(4 - 3 \times S_g\right),$$

Where

$$S_\alpha^* = S_{\alpha i} - \frac{S_{\alpha i} - S_{\alpha r}}{S_{\alpha i} - S_{\alpha r}(C_\alpha)}\left(S_{\alpha r} - S_\alpha\right), \alpha - \text{oil, water.}$$

Here, S_{ai} and S_{ar} are the initial and residual saturation with phase α. C_α is the coefficient taking into account the solubility of CO_2 in the α phase. Subscripts "*o, w,* and *g*" indicate that the parameters belong to the oil, water, and gas phases.

According to the development history, modified phase permeabilities were obtained. They have a form that differs in that the exponent in the expression for K_{po} is 3.3 (Chizhov et al 2019,Efimov et al 2019, Dubinsky et al 2018 , Andreev et al 2019, Bentahar et al 2023), and the factor in the expression for K_{pw} is 0.25. In addition, the parameters of the aquifer for the D_2 formation were refined (Table 9). The identification results are shown in Figure 9.

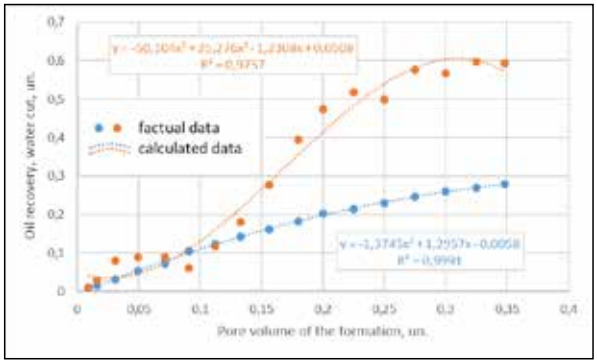

Figure 9. Dependence of oil recovery and water cut on the pumped liquid volume

Table 9. Initial data for determining development indicators

Options	Dimension	Values
Object area	m^2	6430000
Average depth	m	2150
Oil pay thickness	m	9.0
Porosity	%	16
Oil saturation: Initial Residual	%	 87 26
Geological reserves: Oil Gas	 million tons billion m^3	 5.24 0.26
Viscosity in reservoir conditions: Oil reservoir and injected water	mPa×s	 5.85 0.86
Permeability	×10^{-12} m^2	0.15
Permeability variation coefficient	%	79
GOR	m^3/t	49.0
Displacement ratio	%	70.0
Area sweep efficiency	%	92.5
Well operation factor		0.95
Initial formation temperature	°C	40
Initial reservoir pressure	MPa	23.6
Saturation pressure	MPa	9.7
Downhole pressure in production wells	MPa	13.0
Pressure at the mouth of injection wells	MPa	15.0
Discharge pressure	MPa	34.0
Pressure drops	MPa	21.0
Density in reservoir conditions: Oil Gas Water	g/cm^3	 0.842 0.00112 1.06
Conversion factor t of oil in surface conditions in m3 in reservoir		1.267

At the beginning of 2023, 69.6% of the recoverable oil reserves were withdrawn at the pilot site of the field with a water cut of 59.0%. The development is carried out using spot flooding. Due to the fact that CO_2 injection is limited to a supply of 40 thousand tons per year, the pilot facility-polygon is limited to 11 injection and 42 production wells. In these studies, the base case is development with water flooding. Development system parameters were as follows: in-loop flooding, triangular well pattern 500×500 m, density 153,000 m^2, injection to production well ratio 1:3.7. The options for injecting CO_2 rims and water into the D_1 and D_2 formations were modeled using the existing development system. In this case, the reservoir D_2 is covered by the impact of the reagent only within one injection site.

The calculations of technological indicators were preceded by numerical studies on a characteristic element of the development system to determine the best technology for injecting CO_2 and water into the Devonian formations. The processes of flooding, injection of a continuous slug of CO_2 pushed by water, an alternating slug of CO_2 and water with the ratio of their volumes in 1 injection cycle were 2:1, 1:1, 1:1.5, 1:2, 1:3, and 1:5. The analysis of the obtained simulation results showed that with a decrease in the CO_2 as follows: water ratio, the dynamics of the oil fraction and, accordingly, the current oil recovery deteriorate somewhat. However, early gas breakthrough and a rapid increase in the gas factor make the use of the continuous slug injection technology and the risky technology of alternating slug injection with a ratio of 2:1. Moreover, the increase in ultimate oil recovery for these options is lower than for technologies with CO_2: water ratios are 1:1, 1:1.5, and 1:2 (Table 10).

Table 10. Key technological indicators of development of D_1 and D_2 formations with different technology of carbon dioxide and water slug injection (total CO_2 slug - 0.2-pore volume)

Ratio of CO_2 and water slug volumes in one injection cycle	Oil recovery, %	Increase in oil recovery, %	Development period (conditional), years	Cumulative injection of agents, units	Water-oil factor by the end of development, m^3/m^3
Flooding	47.7	-	66.5	1.79	3.02
1 : 5	57.6	9.9	89.5	2.26	2.97
1 : 3	57.9	10.2	80.8	2.08	2.62
1 : 2	58.4	10.7	79.8	2.01	2.45
1 : 1.5	58.4	10.7	75.6	1.94	2.33
1 : 1.0	58.3	10.6	71.3	1.88	2.22
2 : 1.0	58.0	10.3	67.7	1.84	2.15
CO2 slug only	35.6*	12.1	22.0	0.59	0.66

*Note: Wells are shut down when GOR reaches 2000 m^3/t.

A comparison of the technological parameters of the options shows that the injection of CO_2 and water in a ratio of 1:1 is somewhat better than the others. With almost the same increase in oil recovery, there is a better dynamic of displacement characteristics, a shorter development period, and a lower water-oil ratio. Similar results were also obtained for ratios of 1:1.5, and 1:2. Nevertheless, from these three options, one should choose the option with a ratio of CO_2: water - 1:2, which represents the least risk of a premature breakthrough of carbon dioxide into production wells. For the selected technological ratio (CO_2: water - 1:2), various calculations were performed with different total carbon dioxide rim - 0.1, 0.2, and 0.3 of the pore volume of the polygon object. The calculation results are shown in Figure 10.

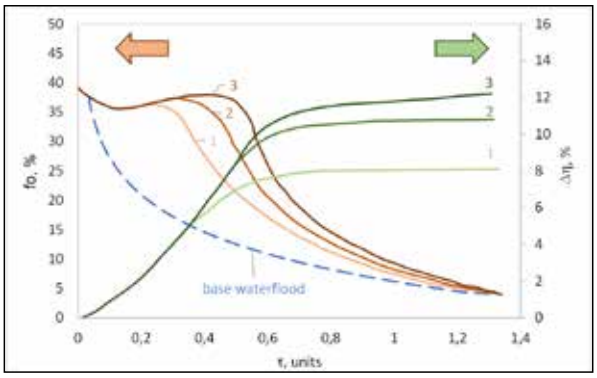

Figure 10. Dependence of oil recovery increment (Δη) and oil fraction (fo) on the withdrawn volume of liquid since the beginning of the method application at various CO_2 slug sizes. Numbers indicate the following: 1 - total CO_2 slug with a value of 0.1 of the pore volume of the formation; 2 – total CO_2 slug – 0.2 of the formation pore volume; 3 - total CO_2 slug - 0.3 of the reservoir pore volume

For these values, calculations of technological indicators of the development of the object under consideration were made. The recommended option is with a total CO_2 slug of 0.3 formation pore volume. The development options using enhanced oil recovery methods do not provide for a change in the number of production and injection wells and their location, compared to the base case. Only the water flooding technology changes. As of January 1, 2023, the current oil recovery in the D_1 and D_2 formations of the experimental area reached 27.4%, and the water cut was 59.2%.

It is assumed that the injection of carbon dioxide began in 2026 and by the beginning of 2028, 29.4 thousand tons will be injected. It is planned to inject carbon dioxide in the period up to 2046 in the amount of 0.3-pore volume of CO_2-covered reserves, which is formally 0.13 pore volume of the entire experimental area. The total consumption of CO_2 will be 789.4 thousand tons. The increase in oil production over the entire development period will be 298.6 thousand tons. 0.39 tons of additional oil will be taken per ton of spent reagent. The estimated total development period is 53 years. The increase in oil recovery due to the use of carbon dioxide will be 12.2%. The value of the ultimate oil recovery in layers D_1 and D_2 of the experimental area will reach 49.2%.

4. Conclusions

Based on laboratory studies to predict the development indicators of a pilot site on geological and hydrodynamic models of an oil field using carbon dioxide, the following data are presented as follows:

- Coefficient of oil displacement by water is 0.700 units;
- Distribution coefficient of CO_2 between oil and water and between oil and CO_2 phase is 1.83 and 4.28 units respectively;
- Increase in oil displacement coefficients for rims of 16, 21, and 30% of the pore volume of the formation is 0.089, 0.100, and 0.110 units respectively;
- Coefficient of oil displacement by carbon dioxide (CO_2 consumption 0.8 formation pore volume) is 0.918 units;
- Coefficient of oil displacement by carbonized water (CO_2 consumption 0.8 formation pore volume, CO_2 concentration - 4.4% wt.) is 0.766-0.780 units;
- The number of portions into which the CO_2 slug is divided is at least 20;
- The ratio of the volumes of portions of water and carbon dioxide is 1.5 or more.

Thus, the use of the parameters of the process of oil displacement by carbon dioxide rims obtained in the course of laboratory experiments, will make it possible to reasonably approach the implementation of the forecast of technological indicators for the recovery of residual oil reserves.

Modeling of oil recovery processes using CO_2 and water rims showed that the final oil recovery would increase by 12.2%, and an additional 0.39 tons of oil would be produced per ton of carbon dioxide.

Acknowledgments

The study has been supported by the Ministry of Science and Tertiary Education of the Russian Federation under Agreement No 075-15-2022-297, part of the WCRC development program.

Conflict of Interests

The authors declare that there are no conflicts of interest regarding the publication of this paper.

References

Andreev, V. E., Mukhametshin, V. V., Kuleshova, L. S., et al, 2023, Reasons for the viscoelastic compositions breakthrough in the process of polymer flooding pilot testing in the conditions of a complex terrigenous reservoir of the Zaburunye deposit. SOCAR Proceedings 1: 051-058.

Andreev V.E., et al, 2019, Forecasting the use of enhanced oil recovery methods in oilfields of Bashkortostan. IOP Conference Series: Earth and Environmental Science. 2019th International Symposium on Earth Sciences: History, Contemporary Issues and Prospects. 012025.

Andreev, V.E., Chizhov, A.P., Chibisov, A.V., 2020, Justification of the use of gas exposure in the conditions of the Volga-Ural province // Acceleration of innovations - institutes and technologies: 91-95.

Andreev, V.E., et al, 2018, Results of modeling the oil displacement process with the use of gas stimulation methods collection of scientific papers: Oil and gas technologies and new materials. Problems and solutions. Vol. 7(12): 147-156.

Andreev, V.E., et al, 2020, Forecasting for application of formation stimulation to BV6 formations of Las-Eganskoye oil field. Journal of Physics: Conference Series. High-Tech and Innovations in Research and Manufacturing, HIRM 2020: 012003.

Bentahar, F., Mesbah, M., Ribstein, P., 2023, Hydrogeological Modeling of the Sandstone Aquifer of Mostaganem Plateau (North-West Algerian) and Perspectives on the Evolution of Withdrawals. The Jordan Journal of Earth and Environmental Sciences Proceedings No. 14:113-125. http://jjees.hu.edu.jo/files/Vol14/No.2/JJEES

Chizhov A.P., et al, 2020, System approach to well construction during gas methods implementation under conditions of productive deposits of Bashkortostan. Problems of Gathering, Treatment and Transportation of Oil and Oil Products No. 1 (123): 95-103. DOI: 10.17122/ntj-oil-2020-1-95-103.

Chizhov, A. P., Doskazieva, G. Sh., Andreev, V. E., et al, 2021, Factors affecting the stability of polymers under flooding conditions at vostochny Moldabek field. Problems of Gathering, Treatment and Transportation of Oil and Oil Products 6(134): 52-69.

Chizhov, A.P., Chibisov, A.V., Efimov, E.R. 2019, Modeling the process of oil displacement by gas on the example of oil fields in Bashkortostan. Innovations and science-intensive technologies in education and economics. Materials of VIII Intern. Scientific-practical and method. P. 196-200.

Chizhov, A.P., et al, 2019, Forecasting the results of gas methods for residual oil reserves of Bashkortostan fields. Collection of scientific papers: Oil and gas technologies and new materials. Problems and solutions. Vol. 8(13): 134-140.

Chizhov, A.P., et al, 2020, Forecasting the results of gas impact on residual oil reserves in the conditions of the Volga-Ural fields. Geology, geophysics and development of oil and gas fields. No. 6: 56-62.

Chizhov, A.P., et al, 2020, Theoretical features of increasing the efficiency of oil recovery from carbonate reservoirs of the Volga-Ural province. SOCAR Proceedings No. 4: 9-14. http://dx.doi.org/10.5510/OGP20200400460.

Chizhov, A.P., et al, 2020, Theoretical features of increasing the efficiency of oil recovery from carbonate reservoirs of the Volga-Urals province. SOCAR Proceedings 4: 9-14.

Dubinsky, G.S., et al, 2018, On the possibility of applying the technology of water-gas treatment using wellhead ejector devices. In the collection: Science-intensive technologies in solving the problems of the oil and gas complex. Materials of the VIII International Youth Scientific Conference. P. 122-127.

Efimov E.R. et al, 2021, Process modeling of gas displacement of oil on the example of oil fields in Bashkortostan. IOP Conference Series: Materials Science and Engineering. International Conference on Mechanical Engineering, Automation and Control Systems, MEACS 2020: 012060.

Efimov, E.R., et al, 2019, Review of the use of gas methods to increase oil recovery in the fields of Russia and abroad. Collection of scientific papers: Oil and gas technologies and new materials. Problems and solutions. Vol. 8(13): 141-146.

Mousa, M., Manar, F., Mufeed, B., 2012, Preparation of Natural Standard Reference Material (SRM) for Ellajjun Oil Shale/ Jordan. Jordan Journal of Earth and Environmental Sciences, Vol. 4: 15- 22.

Qahir, N. A., Arabi, N. A., Taiser, S. K., 2014, Effect of Oil Shale Ash on Static Creep Performance of Asphalt-Paving Mixtures. Jordan Journal of Earth and Environmental Sciences, Vol. 6: 67-75.

Rabaev, R.U., et al, 2021, Results of experimental studies of integrated physico-chemical impact in carbonate reservoirs. SOCAR Proceedings 2: 34-39.

Yamaletdinova, K.Sh., et al, 2020, Experiment to find the oil displacement factor. Collection of scientific papers: Oil and gas technologies and new materials. Problems and solutions. Vol. 9(14): 276-278.

JJEES

JJEES (2024) 15 (2): 136-145
ISSN 1995-6681

Jordan Journal of Earth and Environmental Sciences

Identifying Climate Scenarios and an Index-Based Assessment of Household Vulnerability to Climate Change in the South-West Coastal Region of Bangladesh

Niger Sultana[1] and Md. Kamrul Hasan[2*]

[1]Student, Department of Urban and Regional Planning, Pabna University of Science and Technology, Pabna, Bangladesh.
[2]Assistant Professor, Department of Urban and Regional Planning, Pabna University of Science and Technology, Pabna, Bangladesh

Received March 28, 2022; Accepted October 7, 2023

Abstract

Climate change harms the households of coastal areas in Bangladesh because of the geographical position and changes in the climatic elements that are primarily at play. This study looks at the pattern of two prominent climatic elements: temperature and precipitation over thirty years, from 1992 to 2021, focusing on how those factors have changed. The findings revealed an upward increase in all elements, i.e., the maximum temperature, the lowest temperature, and the amount of precipitation. Using the Livelihood Vulnerability Index, this research looked at how vulnerable households are to the effects of climate change in the southwestern coastal area, namely in Amadi Union and Koyra Upazila in the Khulna district of Bangladesh. The original data came from a survey of 276 households and secondary data on rainfall and temperature for the period beginning in 1992 and continuing through 2021. The research conducted a comparative analysis to determine the household's vulnerability to climate change. The empirical research found that families in the Amadi union were moderately exposed to the effects of climate change and the weather variability regarding their strategies for making a living, their social networks, the food they have, and their level of health. By considering the socio-demographic elements, social networks, livelihoods, natural disasters, and climate variability, households of the Amadi union were equally vulnerable regarding their adaptation potential and exposure. These findings have implications for the governments, donor agencies, and other relevant agencies in Amadi Union, Koyra Upazila, and Khulna, initiating and implementing initiatives to adapt to climate change and increase household resilience.

Keywords:*Climate change, Climatic trend, Vulnerability, Livelihood Vulnerability Index.*

1. Introduction

Bangladesh is one of the countries that is among the most vulnerable to the effects of climate change. This vulnerable situation is due to the country's undesirable location, flat, low-lying topography, high density of population, extreme poverty, dependence on climate-sensitive industry segments, particularly agriculture and fisheries, and ineffective institutional characteristics (Climate Change Cell, 2006; DoE, 2012; Ahmed et al., 2013). Severe weather events have occurred in Bangladesh, a nation with a total area of 147,570 square kilometers and roughly 160 million people (BBS, 2001; Dewan, Yamaguchi, and Rahman, 2012). On average, there are 1015 people per square kilometer, and the yearly growth rate is 1.37 percent (BBS, 2011). The 35 million people who reside in the Bay of Bengal's low-lying coastal districts are particularly at risk from natural disasters such as storm surges caused by cyclones, coastal floods, river bank erosion, sea level rise, and saline water intrusion (BBS, 2013); (Dasgupta et al., 2014). The beaches of Bangladesh are dynamic, have multiple functions, and are challenging to represent spatially (FAO, 1998). The coastline of Bangladesh contains 147 sub-districts and 19 districts, with a combined size of 47,201 km^2 in total (BBS, 2013).

The country's coastline, which accounts for 32% of its total land, exacerbates the consequences of climate change. The problem at hand is the climate alteration in every region of the earth. Climate change results in weather that is both more severe and unpredictable (IPCC, 2007). Climate change includes both the increase in frequency and the increase in intensity. Disasters, such as floods, cyclones, tornadoes, tidal surges, storm surges, river banks, shoreline erosion, and droughts, are frequent occurrences in the tropical region of Bangladesh (Hahn, Riederer, and Foster, 2009).

The "cyclone season" runs from April to May and September to November, negatively impacting the lives of people experiencing poverty in twelve districts (Abu et al., 2017). These districts include Khulna, Bagerhat, and Satkhira. People of Khulna, Bagerhat, and Satkhira in the Southwest coastal zone lost their lives and their means of subsistence when river dams, dykes, and polders ruptured as a result of Cyclone Aila's tidal surges that reached a height of 13 feet on May 25, 2009. Before Aila, on November 15, 2007, a storm named Sidr battered the coastal districts of Bangladesh with a surge that was as high as 16 feet. In October 2022, storm Sitrang attacked the coastline of Bangladesh (The Daily Samakal, 2022). Recently, hundreds of residents were affected by flooding in Mafraq City's central and western areas. It is vital to manage such floods in

* Corresponding author e-mail: kamrul.urp@pust.ac.bd

order to keep them under control and reduce the effects they have on the local population (Amoush et al., 2017).

According to the Intergovernmental Panel on Climate Change (IPCC), climate change, induced by humans, is causing a dangerous and widespread disruption in nature, affecting billions of people worldwide (IPCC, 2022; Ahmed, 2019). Those populations and ecosystems that are the least equipped to adapt to changing conditions are the ones that will suffer the most (IPCC, 2022). The rising intensity and frequency of weather extremes, droughts, and flooding are already exceeding the limits of tolerance that plants and animals have evolved to resist, leading to the loss of entire ecosystems, such as forests and coral reefs (IPCC, 2022). They have put millions of people in danger of starvation and dehydration, particularly in Africa, Asia, Central and South America, tiny islands, and the Arctic (DoE, 2012). To reduce the number of lives lost, the biodiversity, and the infrastructure destroyed due to climate change, urgent, ambitious, and speedy adaptation to climate change is required, in addition to rapid and significant reductions in greenhouse gas emissions (IPCC, 2022).

Bangladesh is in South Asia (Ahmed et al., 2013). These tidal currents are indeed the source of a broad range of weather events, such as tropical cyclones, severe storms, coastline erosion, seasonal wind, vaporization for monsoon rains, floods, and saline intrusion (Islam et al. 2015). According to Ahmed et al. (2013), the coastal areas of Bangladesh are more prone to being negatively affected by the consequences of global warming (Ahsan and Warner, 2014). This study aims to analyze the climate scenarios and evaluate the sensitivity of a portion of Bangladesh's coastal areas to the effects that climate change will have on the way people live in that location. The Livelihood Vulnerability Index (LVI), produced by Hahn et al., is applied here in this research (Hahn, Riederer, and Foster, 2009). This index takes its primary data from housing units and uses some variables. As a result, it can measure not only the degree to which households are vulnerable to the effects of natural disasters and climatic variability but also their capacity for adaptation and their level of sensitivity to the effects of climate change. In addition, the computation of this index is more straightforward than other indices because it utilizes primary data from residences (Adger et al., 2009).

2. Materials and Methods

2.1 Study area profile

The research has been carried out in Amadi Union, Koyra Upazila, and Khulna, Bangladesh's southwest coastal districts. One of the most well-known sub-districts in Bangladesh's southern coastal belt is the Koyra sub-district of the Khulna District (Ahsan and Warner, 2014). The union's 41.47 square kilometer area is bordered to the north by the Chadkhali Union, to the east by the Maheshwarpur Union, to the south by the Koyra River, and to the west by the Kopotakkho River. In the Amadi Union, there are 27 villages and 17 mauzas (BBS, 2011). The meeting of three rivers, the Kopotakkho, the Sakbaria, and the Koyra River, is where the Koyra Subdistrict is situated. Men (19868), women (20336), and 8445 households make up the total population of 40200. The Amadi Union has a 77 percent literacy rate, which includes 14 high schools and three colleges (BBS, 2011; Koyra Upazila., 2011; Amadi Union Parishad, 2022). Due to its coastal location, the research area experiences cyclones, tidal waves, inundation, heavy rainfall, river erosion, saline soils, and waterlogging (Ahsan and Warner, 2014). Sidr in 2007 and Aila in 2009, two catastrophic storms, devastated the region in close succession (BBS, 2011). The Harinkhola Dam in Koyra Upazila of Khulna collapsed by 200 meters recently due to Cyclone Sitrang, and the seaports of Mongla and Payra received Distress Signal Number 7. As a result of Cyclone Sitrang, ten to twelve local villages, notably Upazila Parishad, were inundated, and the high tides in the nearby rivers surged by five to seven feet above regular waves (The Daily Samakal, 2022).

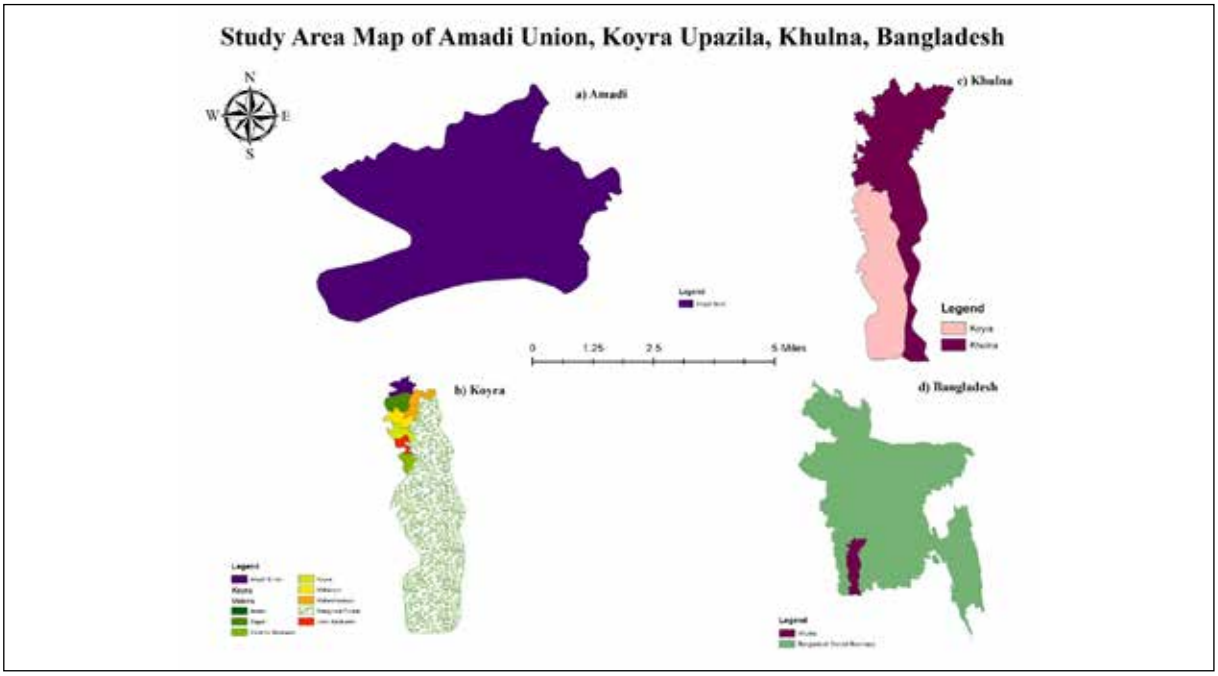

Figure 1. Amadi Union, Koyra Upazila, Khulna, Bangladesh

2.2. Data Collection

Primary and secondary data have been used to examine the climatic scenarios and livelihood vulnerability of Amadi Union, Koyra upazila, and Khulna, Bangladesh.

2.2.1. Primary data

The "Household Questionnaire Survey" was used to collect the primary data, and the sample size was initially determined using the "Yamane formula" (1967) with a 95% confidence level, 10% precision, and 50% prevalence:

$$n = N/(1 + Ne^2) \quad (1) \text{ (Yamane, 1967)}$$

where, n = Sample size
N = Household size
E = Margin of error
Here, household size = 8445

The margin of errors = 0.005, and the sample size is 382 households.

$$n = 8845/(1 + 8445 * (0.005)^2) = 381.95$$

Using statistics from the 2011 national census, which determined the union's total population, 276 residences, rather than (n= 382), were surveyed in the Amadi union due to weather conditions, a lack of time, and a shortage of employees. When the field team arrived at the block, community leaders were called to inform them of the study's purpose and request permission to meet homes. The Expanded Program on Immunization of the World Health Organization (WHO)'s "random walk" technique served as the basis for the home sampling strategy (WHO, 2005). The survey was conducted in August 2022 from the 20th to the 26th.

2.2.2. Secondary data

Secondary data is information that another party has previously gathered. Data sources include government reports, websites, books, journal articles, and internal documents. Second-hand data sources include the Bangladesh Bureau of Statistics, World Bank Group, Climate Change Knowledge Portal, NASA Prediction of Worldwide Energy Resources (POWER) access data viewe, World Climate Data, Diva GIS portal, and Amadi Union Office. Secondary data on climatic elements were collected from the following source, as shown in the Table, and then processed in DIVA-GIS and MS Excel.

2.3. Examination of Climate Scenarios

2.3.1. Trend analysis of climatic elements (temperature and rainfall)

The trend analysis uses the monthly maximum temperature and monthly lowest temperature data. Y = a + bx connection was used to calculate the central tendency value (represented by value a) and rate of incremental value (represented by value b). Then, a straightforward statistical analysis was performed using the mean, range, standard deviation, and coefficient of variation (RECOFTC, 2016). The following relationships were used to derive linear trend line equations based on the 30 years of temperature time series records (1992–2021). This study has calculated the climatic elements trend analysis only for the Koyra Upazila, not the Amadi union because union-level data is too small to find the climatic variations. Climatic elements data, i.e., temperature and rainfall, are similar for both the Union and Upazila levels. That is why this study has used the Upazila level data to analyze the climatic trend of Koyra Upazila.

$$Y = a + bx \quad (2) \text{ (RECOFTC, 2016).}$$

Thus, for a given time t, the estimated value Y_e of Y (temperature axis) can be written as

$$Y_e = a+bx \quad (3) \text{ (RECOFTC, 2016).}$$

The value of a and b was computed by using equations 3 and 4 respectively

$$\sum Y = na + b\sum x \quad (4) \text{ (RECOFTC, 2016).}$$

Hence, $a = \sum Y/n$ as b becomes zero.

$$\sum xy = a\sum x + b \sum x^2 \quad (5) \text{ (RECOFTC, 2016).}$$

Hence, $b= \sum XY/\sum x^2$

where n is 30 (climatic data series of 30 years), and t is the corresponding time. The existing and future maps are prepared using DIVA-GIS 7.5 world climate data (RECOFTC, 2016).

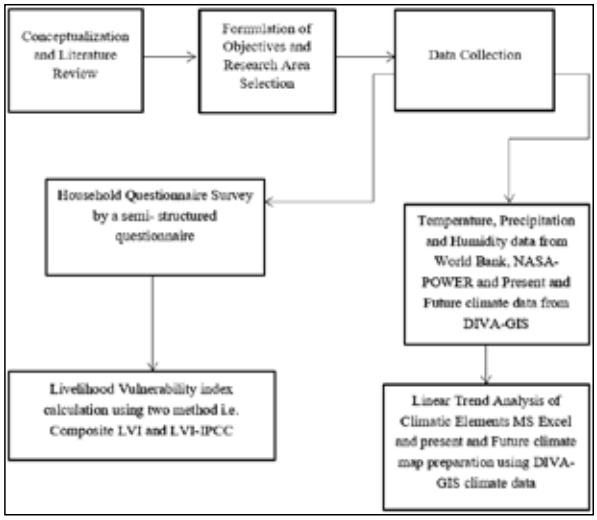

Figure 2. Methodological framework of the research

2.3.2. Assessment of Livelihood Vulnerability

2.3.2.1. Calculation of Livelihood Vulnerability Index (LVI)

This study utilized a metric known as the Livelihood Vulnerability Index (LVI), conceived by Hahn and his colleagues (2009). The extent to which a household is susceptible to the impact of climate change and natural disasters, as well as the household's capacity for adaptability and responsiveness to the effects of climate variability, can be determined by some variables. These variables include the family's location, the family's socioeconomic status, the family's level of education, and the family's story of income, etc. (Hahn et al. 2009). Except for the data about temperature and precipitation, the computation of this index is made much simpler, thanks to the utilization of data gathered from individual residences.

The research relied on a total of eight essential components, including the socio-demographic profile (SDP), livelihood strategies (LS), social networks (SN), natural capacity, health (H), food (F), water (W), and natural disasters (ND). While calculating the vulnerability index, Hahn et al. (2009) used a symmetrical weighted average method. This method ensures that each indicator contributes the same

amount to the overall index, despite different components, including varying numbers of indications. As a result of the fact that each hand would be tracked on a unique scale, it was first necessary to normalize each indicator so that it could be represented by an index employing equation 6:

$$\text{Index } X_{ij} = (X_{ij} - \text{Min } X_i)/(\text{Max } X_i - \text{Min } X_i)$$

(6) (Hahn et al. 2009).

Index Xij signifies the index score (0–1) of the sub-component or indicators for union j, Xij signifies the value of the ith hand for each union, and Max Xi and Min Xi illustrate the maximum and minimum values of the ith indicator throughout all blocks. After indexing all of the arrows, the average of the importance of the hands was used to get the value of each significant component. Finally, the following equation 7 was used to determine each of the eight primary members:

Livelihood Vulnerability Index,

$$LVI_j = \frac{(W_{SDP}SDP_j + W_{LS}LS_j + W_{SN}SN_j + W_{NRE}NRE_j + W_H H_j + W_F F_j + W_{ND}ND_j)}{W_{SDP} + W_{LS} + W_{SN} + W_{NRE} + W_H + W_F + W_{ND}}$$

(7) (Hahn et al. 2009).

The total weights of each single component are added together to get the vulnerability index, which is the same thing. The number of subcomponents used to manufacture an element might impact the Wmi, also known as the component's overall weight. For instance, if the SDP consists of four indicators, the WSDP will similarly contain four. In this scenario, the livelihood vulnerability index for district j, abbreviated as LVIj and "the livelihood vulnerability index for district j," corresponds to the weighted mean of seven primary components. To ensure that each sub-component contributes an equal amount to the total LVI, the weight values of each significant element, which Wmi denotes, are calculated according to the absolute number of sub-components contained within that considerable component (Sullivan, 2002). This research utilized a scale of LVI grades ranging from 0 to 0.2, being considered not to be vulnerable, 0.21 to 0.4 being moderately vulnerable, and 0.441 to 0.5 being very vulnerable (Suryanto and Rahman, 2019).

2.3.2.2 LVI-IPCC

The IPCC-LVI is yet another tool to create indices that indicate vulnerable places. According to the Intergovernmental Panel on Climate Change, vulnerability results from three contributing elements: adaptive capacity, susceptibility, and exposure. Adaptive capability refers to an individual's ability to adjust to changing conditions (IPCC, 2001; IPCC, 2011).

Vulnerability = f (Exposure, Sensitivity, and Adaptive capacity) (8) (IPCC, 2001).

The following equation brings together, among other factors contributing to openness, the components of the vulnerability index known as exposure, ability to adapt, and sensitivity (Hahn et al., 2009).

$$CF_j = \frac{\sum_{i=1}^{n} W_{mi} M_j}{\sum_{i=1}^{n} W_{mi}}$$

(9) (IPCC, 2001).

Where Wmi is the number of factors that comprise each component, CFj is the factor contributing (exposure, sensitivity, or adaptive capacity) to the union j, and Mij is the significant component for the j union indexed by i. Following the IPCC's definition of vulnerability, IPCC-LVI was computed after accounting for exposure, sensitivity, and adaptive capacity.

$$\text{IPCC-LVI} = (\text{EI} - \text{AI}) \times \text{SI}$$

(10) (IPCC, 2001).

The sensitivity index is SI, the adaptive capacity index is AI, and the exposure index is EI. This study employed the LVI-IPCC scale, ranging from (-1) to (-0.4), which is not vulnerable, through (-0.41) and (0.3) which is moderately weak, and (0.31) and (1) which is highly vulnerable (Suryanto and Rahman, 2019).

3. Results and Discussion

3.1. Examination of climatic scenario

3.1.1. temperature

The following figures show a positive linear maximum temperature trend in Koyra Upazila, Khulna. In 1992, the annual maximum temperature was 42.35 degrees Celsius; in 2021, it was 43.48 degrees Celsius. The current maximum yearly temperature of Koyra Upazila ranges from 30 degrees Celsius to 31 ° degrees Celsius, which will increase to 33 degrees Celsius by the year 2100, showed in the maps. However, Hossain et al. (2014) showed that the lowest average temperature is in January, and it will gradually increase until June, fluctuating from July to October, and then decreased until December in Dhaka.

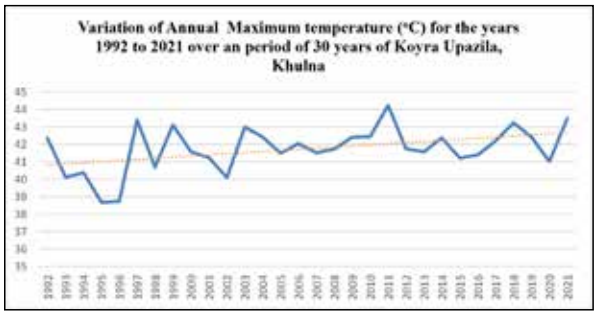

Figure 3. Variation of Annual Maximum temperature (°C) for the years 1992 to 2021

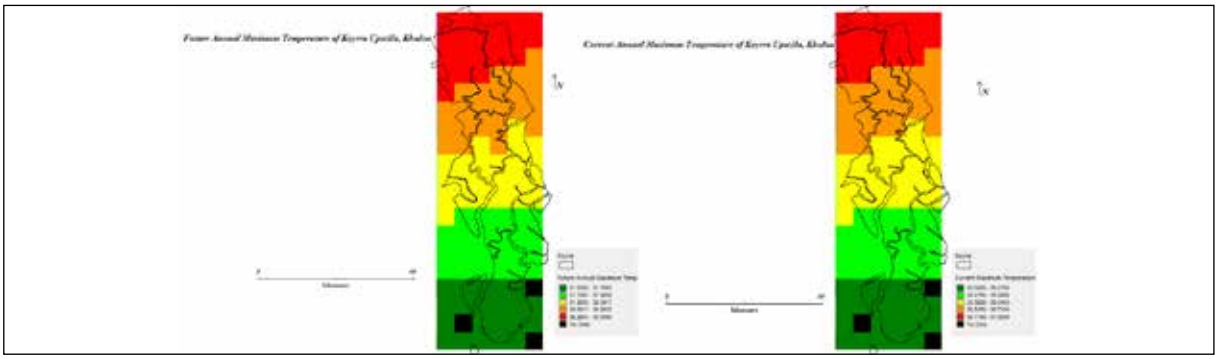

Figures 4. (left) and **5.** (right). Map of Annual Maximum Temperature (Current and Future) of Koyra Upazila, Khulna Source: World Climate Data 2022

Yet for each month in 2021, compared to 1992, the monthly minimum temperature has also increased linearly. The temperature variation lends credence to the observed size and frequency of extreme weather events, resulting from global warming. Figure 6 shows that there is a positive linear trend of minimum temperature in Koyra Upazila, Khulna. In 2013, the annual minimum temperature was recorded lowest at 17.73 degrees Celsius. In 2017, it was the highest at 19.34 degrees Celsius. In 2021, the annual minimum temperature was 18.87 degrees Celsius, and in 1992 it was extremely low at 18.27 degrees Celsius.

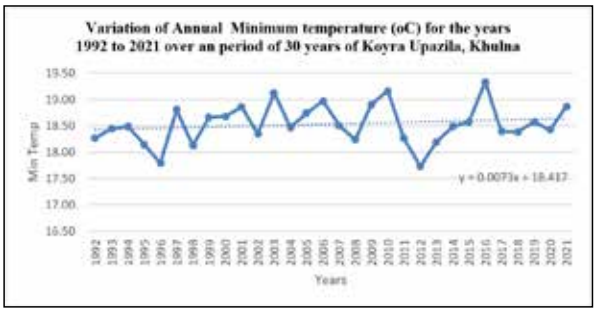

Figure 6. Variation of annual minimum temperature (°C) for the years 1992 to 2021

3.1.2. Rainfall

The second climatic element to examine climate scenarios is the amount of rainfall. The annual precipitation of Koyra Upazila has a positive linear trend that denotes an increment in yearly rain. The annual rainfall (SD value) in 1992 was 2.64, which increased to 6.72 in 2021, achieving a more significant increase in annual precipitation and cyclones, i.e., Mahasen and Nargis attacks. In 2007, the annual rainfall (SD value) was 5.76, and this year cyclone Sidr attacked the coastal belt of Bangladesh. In 2020, several cyclones shot the coastal belt of Bangladesh, i.e., Foni, Bulbul, and Amfan, and the precipitation level (SD value) of that time was 7.48. The Figure below represents the Khulna district's annual precipitation from 1992 to 2021. The following maps show current and future annual precipitation. The yearly rainfall ranged from 1170 mm to 2072 mm and 1794 mm to 2022 mm.

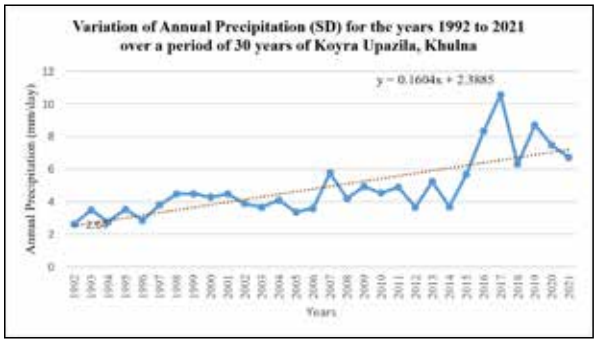

Figure 7. Annual Precipitation (mm) of Koyra Upazila, Khulna District, over the period 1992 to 2021

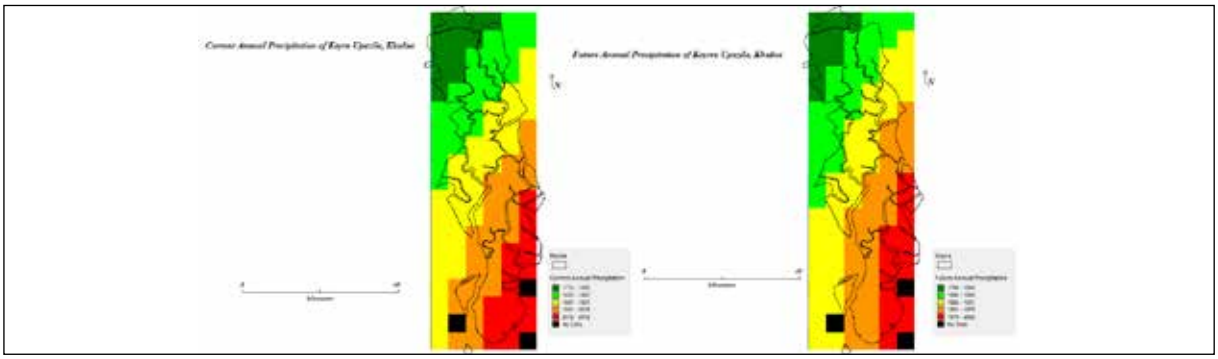

Figures 8. (left) and **9.** (right). Map of Annual Maximum Rainfall (Current and Future) of Koyra Upazila, Khulna
Source: World Climate Data, 2022

3.2. Assessment of Livelihood Vulnerability

3.2.1. Livelihood Vulnerability Index (LVI) of Amadi Union, Koyra, Khulna

Data from 276 households in the Amadi Union, Koyra were used to calculate the LVI and the LVI-IPCC. The LVI scores suggest that families in Amadi have a moderate vulnerability (LVI=0.40), and the LVI-IPCC scores indicate the same thing (-0.0013). Therefore, these scores reflect the same conclusion.

According to the findings, the vulnerability indices of the primary component fell somewhere in the range of 0.24 to 0.55. The index varied from 0 to 0.2, representing non-vulnerability, 0.21 to 0.4, representing moderate vulnerability, and 0.41 to 0.5, representing very vulnerable. The composite value of the LVI was 0.40, which indicates moderate exposure according to the index.

The Socio-Demographic Profile (SDP), consisting of six subcomponents, was the first significant component of the study. The analysis, as a whole, was conducted using these six subcomponents. According to the socio-demographic profile index, which gave the degree of vulnerability a score of 0.24, the level of exposure was assessed to be moderate on the indexed scale. The dependency ratio index for the Amadi Union was 0.278, which indicated that the proportions of the people, under 15 and over 65 years old, who were dependent were moderate, showing moderate vulnerability. Additionally, the proportions of dependents, under 15 and over 65 years old, were reasonable and indicated moderate exposure. It is estimated that approximately 18% of the heads of households in the union did not have a primary education, which means that they did not ever attend school at any time in their lives. On average, 5.17 persons called each house their home, and the vulnerability score for the typical family member was 0.314, which is in the moderate range. In addition, the average age of heads of households was 38.67 years old, with an index of the average age of

0.408, suggesting a greater degree of vulnerability. Just 12.3 percent of household members possessed any expertise, either formal or informal, while women headed 16.3 percent of households. Based on this statistic, it may be deduced that households headed by women will be more vulnerable than those led by men.

Table 1. Indexed major component and overall LVI value (calculated using equation 12)

LVI-IPCC	Major Component	Sub Component	Amadi, Koyra
Adaptive Capacity 0.377	Socio-demographic profile (SDP)	Percentage of Female-headed household	0.24
		Average Age of Household Head	
		Dependency ratio	
		Percentage of Households where the Head of the household Head had not attended school	
		Percentage of Households where members had any formal or informal skill	
		An average family member in a household	
	Livelihood Strategies (LS)	Percentage of Households dependent solely on agriculture as an income source	0.55
		Percentage of Households dependent on other occupations	
		Percentage of Households who have the burden of a loan	
	Social Networks (SN)	Average Time to reach nearest vehicle station (Minutes)	0.48
		A percentage of HHs have communicative devices (TV, radio, mobile, etc.) at home	
		Percentage of HHs where a family member is affiliated with any organization	
Sensitivity 0.44	Food (F)	Percentage of Households dependent solely on the family farm for food	0.46
		Percentage of Households struggle to find food to support the whole year	
		Percentage of Households with a primary irrigation source	
		Percentage of Households that do not save crops	
	Natural Capacity (NC)	Average Household income per month	0.34
		Percentage of Households using natural resources for livelihood	
		Percentage of Households with fertile land	
	Health (H)	Average Time to health facility (minutes)	0.51
		Percentage of Households with a family member with chronic illness	
		Percentage of Households receiving treatment from government or private hospitals	
	Water (W)	Percentage of Households that utilize a natural water source	0.48
		Average Time to reach water source (minutes)	
		Percentage of Households reported to have a water availability problem	
Exposure 0.374	Natural disasters and climate variability (ND)	The average number of flood, cyclone, storm surge, and river bank erosion events in the past six years (Years: 2016-2021)	0.374
		Households that did not receive a warning about the pending natural disasters	
		Mean standard deviation of the monthly average of average maximum daily temperature (years: 1992 to 2021)	
		Mean standard deviation of monthly average minimum daily temperature (years: 1992 to 2021))	
		Mean standard deviation of monthly average precipitation (years: 1992 to 2021)	
LVI-IPCC -0.0013	Overall LVI (using equation 03)	0.40	

The plan consisted of three sub-components subdivided into the Livelihood Strategies (LS), the second most essential aspect of the project. When each of the individual components is aggregated, Amadi displayed a level of susceptibility that is noticeably elevated to a much higher level. There are 39 percent of households in the neighborhood whose sole source of income comes from agricultural endeavors. Amadi is also home to families heavily dependent on various types of employment, including but not limited to business people, drivers, day laborers, fishermen, and a variety of others. In addition, the weight of loan payments is carried by 56% of households, which implies a higher level of vulnerability. This value demonstrates that a family's dependence on the agricultural sector makes them more vulnerable to the effects of climate change than families whose primary source of income is not agriculture. They are more resilient to the impacts of climate change. Because around 70 percent of people live outside of cities and work in other economic sectors, they are far less vulnerable to the effects of climate change.

The Social Network (SN) was the third component, and it was subdivided into three different parts to understand it better. Amadi revealed a higher degree of susceptibility when each constituting element was considered (0.488). The average time necessary to reach the next vehicle station was 19.48 minutes, and an index score of 0.262 indicates moderate vulnerability. Around 94.9 percent of residents had communication equipment, such as televisions, radios, and mobile phones (59.1 percent). This equipment included radios, televisions, and mobile phones. Only 25.4% of people living in households were members of any government or non-government bodies, that would make people more vulnerable to the effects of climate change.

The fourth component was food (F), broken down into four distinct subcomponents before being assembled. The total score for this component was 0.46, suggesting a greater degree of susceptibility to the consequences of climate change. This score was determined by adding together all of the values of the sub-components. The fact that 51.4% of households had trouble locating sufficient food to last throughout the year indicates greater vulnerability. When a family knows they will always have food available, they can better deal with the pressures from the outside world, such as those brought on by extreme weather (World Bank, 2010).

As a result of the fact that people, communities, and nations have access to more significant amounts of high-quality food, actual prices decline. Because of this decline, the basic incomes of these organizations can grow, as they develp strategies for adjusting to the effects of climate change (World Bank, 2010). In the Amadi Union, approximately 32% of the households obtained all their food from family farms, while 82% did not store their crops. This hugepercent presents a challenge since farm households that derive most of their nourishment from their crops are more exposed to the adverse effects of climate change. According to the food subcomponent index, the families whose primary food source comes from their crops are most sensitive to climate change's impacts. These households do not store food for use in times of need when the weather is unexpected. And just 19% of households have access to some irrigation supply, which leaves them vulnerable to the effects of climate change and makes them more likely to be affected by natural disasters.

The seventh primary component of the formula was denoted by the letter "W," and it was water, composed of three sub-components. The element of the vulnerability index known as water has Amadi's highest recorded score of any other location (0.48). Most Amadi households, 58.7%, have claimed that natural water sources are their primary potable water supply. The existence of natural water sources increased the likelihood that a family would fall victim to waterborne diseases. Moreover, natural water sources made it more challenging to obtain water during the dry season. Because of the proximity of the water sources to one another in each of these villages, the majority of the responsibility for gathering water fell on the shoulders of the women and children. The number of hours working mothers spent watching for their children and sending them to school did not significantly change. They are compelled to look for alternative water sources to satisfy their family's requirements for water in an area where seventy percent of households reported having water availability problems. It takes an average of seven minutes to get to the closest source of water, which gives it an index value of 0.16, indicating a reduced level of vulnerability. In recent years, the Tigris River has faced a number of challenges, including a lack of resources, dam construction by neighbouring countries, and the inflow of industrial and agricultural waste water as well as local trash (Hadithi et al., 2019).

The eighth and final main component was natural disasters and climatic variability (ND), which had five sub-components to make up the components as a whole. When everything was considered, the data for the Amadi Municipality suggested a higher level of danger (0.374). A notice about an imminent natural hazard with indices of 0.275 was provided to around 27.5 percent of households in the Amadi Union that did not receive a warning about the most catastrophic flood, drought, and cyclone event that has occurred in the preceding six years in the region. During the past six years, the Amadi Union has documented an annual average of three instances of flooding, cyclones, storm surges, and bank erosion (Years: 2016-2021).

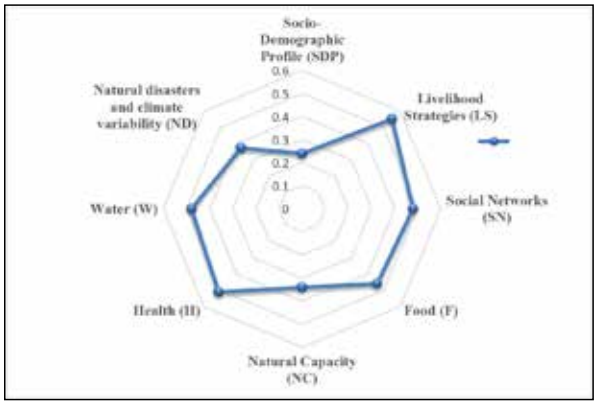

Figure 10. Vulnerability score of the major components of the Livelihood Vulnerability Index (LVI) for Amadi Union, Koyra Upazila

2016 and 2017 witnessed the fewest natural disasters (2), compared to 2020, which had the most natural disasters (5). Given that the index for this union is 0.3, it can be deduced that its susceptibility to the effects of climate change is moderate. During the 30 years, the Amadi Union reported an index of 0.464 for the mean and standard deviation of monthly average minimum daily temperatures and an index of 0.53 for the mean standard deviation of monthly average maximum daily temperatures. Both of these values were based on monthly averages. The weights, observed for Amadi's indices on the mean standard deviation of monthly average precipitation, were 0.263 throughout the research, which spanned from 1992 to 2021. According to the mean standard deviation of the monthly average rainfall, these values would indicate that the Amadi Union had a degree of susceptibility in the middle of the spectrum.

3.2.2. LVI-IPCC for Amadi Union, Koyra, Khulna

The following figures show a positive linear maximum temperature trend in Koyra Upazila, Khulna. In 1992, the annual maximum temperature was 42.35 degrees Celsius; in 2021, it was 43.48 degrees Celsius. The current maximum yearly temperature of Koyra Upazila ranges from 30 degrees Celsius to 31 ° degrees Celsius, which will increase to 33 degrees Celsius by the year 2100, showed in the maps. However, Hossain et al. (2014) showed that the lowest average temperature is in January, and it will gradually increase until June, fluctuating from July to October, and then decreased until December in Dhaka.

According to the data, the overall score for the LVI-IPCC was -0.0013. This places it in the category of vulnerable or moderate, depending on how the index, is interpreted. According to the final IPCC weighted LVI scores, a score between (-1) and (-0.4) indicates that a region is not vulnerable to climate change and variability; a score between (-0.41) and (0.3) suggests that an area is weak or moderate; and a score between (0.31) and (1) indicates that a part is the most vulnerable to climate change and variability. Scores ranging from (-0.31) to (1) show a vulnerable to moderate level of exposure. The eight key components were first separated into their respective categories—exposure, sensitivity, and adaptive capacity to arrive at the LVI-IPCC.

Table 2. IPCC-LVI contributing factors and their indexed value

Contributing Factors	Major components for Amadi Union	Number of sub-components per major component	Contributing factor values	LVI–IPCC value for Amadi
Adaptive Capacity	Socio-demographic profile (SDP)	6	0.377	-0.0013
	Livelihood Strategies (LS)	3		
	Social Networks (SN)	3		
Sensitivity	Food (F)	4	0.447	
	Natural Capacity (NC)	3		
	Health (H)	3		
	Water (W)	3		
Exposure	Natural disasters and climate variability (ND)	5	0.374	

The Intergovernmental Panel on Climate Change (IPCC) has come up with a definition of vulnerability that considers exposure, sensitivity, and adaptation. This idea is depicted in the form of the vulnerability triangle, which at any given time can have any value between 0 (which indicates a low contributing component) and 0.44 (which indicates a vital contributing part) (high contributing factor). Based on the vulnerability triangle findings, it is possible to deduce that the families comprising the Amadi Union were moderately vulnerable to climate change and variability. When one considers the circumstances of the families in the association regarding their access to water, their state of health, and their inherent abilities, one arrives at the current state of affairs. We observed that the Amadi Union homes had a capability for household adaptation that made them less sensitive to the effects of climate change.

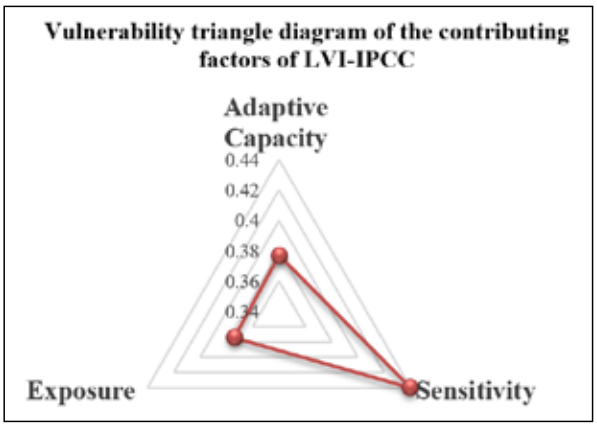

Figure 11. Vulnerability triangle of LVI-IPCC for Amadi Union, Koyra Upazila

The fact that adaptable capacity received a score of 0.377 and exposure received a score of 0.374 indicates that adaptive capacity is almost equal to exposure, although sensitivity received a score of 0.44. Amadi Union is more vulnerable to the effects of natural catastrophes and climatic fluctuations than its ability to adapt.

4. Conclusion

In particular, the LVI and LVI-IPCC methodologies were presented in this study so that the relative susceptibility of populations to the effects of climate change could be determined. Each strategy offers a comprehensive investigation of the elements contributing to the precariousness of households' means of subsistence in a given region. The LVI and LVI-IPCC calculation algorithms were developed to be easily comprehended by many people across various contexts. When comparing two or more research regions using vulnerability spider and triangle diagrams, more information is attained. Our methodology has a few flaws, the most notable of which are the subjectivity involved in selecting the sub-components, the directionality of the relationship between the sub-components and vulnerability, the masking of extreme values by using methods to calculate the indices, and the potential for selection bias due to the exclusion of empty homes from the sample. All of these issues are discussed in more detail below. It is possible to repeat this study in the same region over time to learn more about how districts' exposure, aptitude for adaptability, and sensitivity change as adaptation methods are implemented. In subsequent studies, improving the Social Networks and Natural Capacity subcomponents may be necessary to obtain a more precise measurement of social links. The LVI approach can also be used to analyze the vulnerability of a neighborhood within a district by evaluating the neighborhood level. The Livelihood Vulnerability Index (LVI) is a valuable tool for urban planners. It allows them to assess people's livelihoods' susceptibility to climate change's effects in their areas and devise ways to bolster the most vulnerable industries. In addition, this research provides a valuable tool for understanding the demographic, socioeconomic, and health factors that influence climate sensitivity at the district or community level. Professionals in public health, lawmakers, and development organizations will all be able to benefit from this tool. The research also demonstrates the trend, existing status, and predicted future conditions of the climatic elements. These findings encourage local citizens and the government to create plans and take appropriate action in response to the state of the climatic factors.

Conflict of Interests

The authors declare that there are no conflicts of interest regarding the publication of this paper.

References

Abu, D., John, K. K., Henry, A., & Nophea, S. (2017). Application of livelihood vulnerability index in assessing smallholder maize farming households' vulnerability to climate change in Brong-Ahafo region of Ghana. Kasetsart Journal of Social Sciences,pp. 1-11.

Adger, W., Dessai, S., Goulden, M., Hulme, M., Lorenzoni, I., Nelson, D., Wreford, A. (2009). Are there social limits to adaptation to climate change? Climate Change, pp. 335-354.

Ahmed, H. (2019, January 30). Bangladesh Coastal Zone Management Status and Future Trends. Journal of Coastal Zone Management, vol. 22(1).

Ahmed, N., Occhipinti, A., & Muir, J. (2013). The impact of climate change on prawn post-larvae fishing in coastal Bangladesh: Socioeconomic and ecological perspectives. Marine Policy, pp. 224-233.

Ahsan, M., & Warner, J. (2014). The socioeconomic vulnerability index: A pragmatic approach for assessing climate change led risks–A case study in the southwestern coastal Bangladesh. International Journal of Disaster Risk Reduction, pp. 32-49.

Amadi Union Parishad. (2022). Amadi Union Parishad.

Amoush, H.A., Shabeeb, A.R.A, Adamat, R.A., Fugara, A.A., Ayyash, S.A., Shdeifat, A., Tarazi, E.A. and Rajab, J.A., 2017. The Use of GIS Techniques and Geophysical Investigation for Flood Management at Wadi Al-Mafraq Catchment Area. Jordan Journal of Earth and Environmental Sciences, vol. 8(2), pp. 97 – 103.

BBS. (2001). Bangladesh Bureau of Statistics.

BBS. (2011). Population and housing census-2011.

BBS. (2013). Bangladesh Bureau of statistics. Government of the People Republic of Bangladesh.

Climate Change Cell. (2006). Who is doing what in Bangladesh? Report on the First Meeting, Comprehensive Disaster Management Programme. Dhaka.

Dasgupta, S., Haq, M., Khan, Z., Ahmed, M., Mukherjee, N., & Khan, M. (2014). Cyclones in a changing climate: The case of Bangladesh. Climate & Development, pp. 96-110.

Dewan, A., Yamaguchi, Y., & Rahman, M. (2012). Dynamics of land use/cover changes and the analysis of landscape fragmentation in Dhaka Metropolitan, Bangladesh. Geojournal, pp. 315-330.

DoE. (2012). Environmental outlook. Dhaka: Department of Environment. Government of the People Republic of Bangladesh.

FAO. (1998). Food security and agricultural mitigation in developing countries: Options for capturing synergies.

Hadithi, M.A., Hasan, K., Algburi, A., Paruany, K.A. 2019. Groundwater Quality Assessment Using Irrigation Water Quality Index and GIS in Baghdad, Iraq. Jordan Journal of Earth and Environmental Sciences, vol.10(1), pp. 15- 20.

Hahn, M., Riederer, A., & Foster, S. (2009). The livelihood vulnerability index: A pragmatic approach to assessing risks from climate variability and change—a case study in Mozambique. Global Environmental Change, pp. 74-88.

Hossain, M.Z., Mondal, M.N.I., Sarkar, S.K. and Haque, M.A. 2014. Seasonal Variation of Temperature in Dhaka Metropolitan City, Bangladesh. Jordan Journal of Earth and Environmental Sciences, vol. 6(2),pp. 93- 97.

IPCC. (2001). Contribution of working groups I, II and III to the fourth assessment report of the intergovernmental panel on climate change. Climate Change.

IPCC. (2007). Contribution of working groups I. II and III to the fourth assessment report of the intergovernmental panel on climate change.

IPCC. (2011). The Scientific Basis. Contribution of Working Group I to the Third Assessment Report of the Intergovernmental Panel on Climate Change. Intergovernmental Panel on Climate Change.

IPCC. (2022). Climate Change 2022: Impacts, Adaptation, Vulnerability.

Islam, S. D.-U., Bhuiyan, M., & Ramanathan, A. (2015). Climate Change Impacts and Vulnerability Assessment in Coastal Region of Bangladesh: A Case Study on Shyamnagar Upazila of Satkhira District. Journal of Climate Change, pp. 37-45.

Koyra Upazila Parishad. (2011). Koyra Upazila Parishad.

RECOFTC. (2016). Climate Change Vulnerability Assessment Report: Developing a Demonstration Site in Nepal on Community Forestry, Gender and Climate Change Adaptation.

USAID Climate Change Adaptation Project Preparation Facility for Asia and the Pacific.

Sullivan, C. (2002). Calculating a water poverty index. . World Development, 1195-1210.

Suryanto, S., & Rahman, A. (2019). Application of livelihood vulnerability index to assess risks for farmers in the Sukoharjo Regency and Klaten Regency, Indonesia. Journal of Disaster Risk Studies, vol. 11(1), pp. 739.

The Daily Samakal. (2022). কয়রায় ধসে গেছে ২০০ মিটার বাধ, আতঙ্কে মানুষ.

World Bank (2010.). World Bank Group, Climate Change Knowledge Portal.

World Climate Data, 2022,DIVA-GIS Portal, https://www.diva-gis.org/

WHO. (2005). Immunization Coverage Cluster Survey—Reference Manual. WHO Document Production Services. toward a working definition of adaptive capacity.

Yamane, Y. (1967). Mathematical Formulae for Sample Size Determination.

المملكة الأردنية الهاشمية

صندوق دعم البحث العلمي

الجامعة الهاشمية

المجلة الأردنية
لعلوم الأرض والبيئة

JJEES

مجلة علمية عالمية محكمة

المجلد (١٥) العدد (٢)

http:// jjees.hu.edu.jo/

ISSN 1995-6681

المجلة الأردنية لعلوم الأرض والبيئة

مجلة علمية عالمية محكمة

المجلة الأردنية لعلوم الأرض والبيئة: مجلة علمية عالمية محكمة ومفهرسة ومصنفة، تصدر عن عمادة البحث العلمي في الجامعة الهاشمية وبدعم من صندوق البحث العلمي - وزارة التعليم العالي والبحث العلمي، الأردن.

ترسل البحوث إلكترونيا إلى البريد الإلكتروني التالي:

رئيس تحرير المجلة الأردنية لعلوم الأرض والبيئة

jjees@hu.edu.jo

لمزيد من المعلومات والأعداد السابقة يرجى زيارة موقع المجلة على شبكة الانترنت على الرابط التالي:

www.jjees.hu.edu.jo

المملكة الأردنية الهاشمية صندوق دعم البحث العلمي الجامعة الهاشمية

JJEES

المجلة الأردنية لعلوم الأرض والبيئة

المجلد (15) العدد (2)

مجلة علمية عالمية محكمة تصدر بدعم من صندوق دعم البحث العلمي

ISSN 1995-6681 jjees.hu.edu.jo حزيران 2024